



Master's Thesis

Isabella Chi Gieseler Cortzen

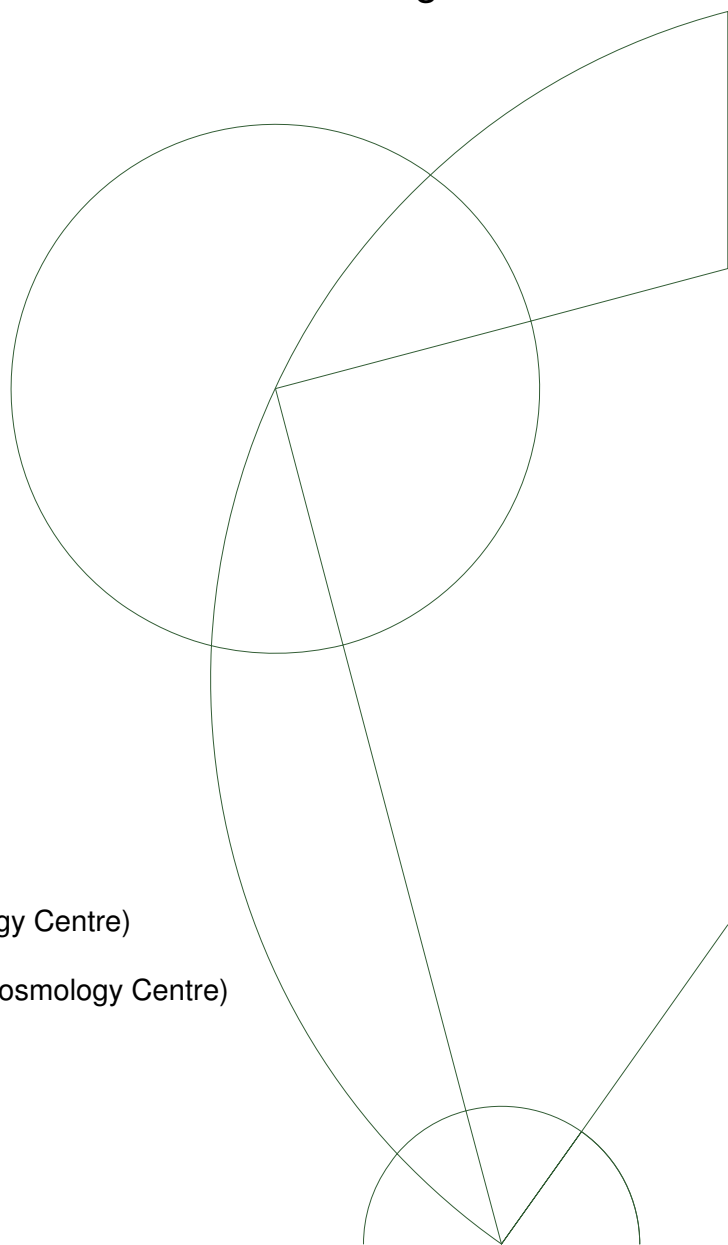
Examining the existence of two distinct modes of star formation

A study of the gas reservoir and dust emission in star-forming galaxies across cosmic time

Supervisors: Professor Sune Toft (Dark Cosmology Centre)

Professor Georgios Magdis (Dark Cosmology Centre)

Submission date: October 14, 2016



ABSTRACT

Observations indicate that the majority of star-forming galaxies (SFGs) across cosmic time follow a remarkably tight relation between the star formation rate (SFR) and stellar mass (M_*) forming a "main-sequence" (MS) of galaxies. Outliers located above the MS for a given M_* are classified as starbursts (SBs) and are present at all redshift. In our local universe these rare systems are represented by ULIRGs, where star formation is triggered by major mergers. The star formation efficiency is defined as the ratio of SFR and the amount of molecular gas, which is the fuel for star formation ($\text{SFE} = \text{SFR}/M_{\text{gas}}$). The gas reservoir is often traced by CO emission lines. In SB galaxies the SFEs are significantly higher compared to MS galaxies. Due to the increasing normalization in the SFR- M_* plane with increasing z , ULIRGs make up the MS population at higher redshifts. Because these galaxies have higher SFRs and gas reservoir, stars formed in a MS galaxy in the early universe might differ from those formed during a smooth secular evolution at low- z . This suggests two distinct modes of SF are responsible for the buildup of stellar mass across cosmic time. However, the distinction between MS and SB galaxies might be enhanced by the gas estimates, which heavily rely on the uncertain bimodal conversion factor α_{CO} .

To examine the two possible modes of SF, a statistically representative sample are collected. The catalog consists of 801 CO detected SFGs from the literature covering a broad range of redshifts. Only the direct observables are considered (L_{IR} and L'_{CO}), in order to obtain direct evidence for SFE variations in both SB and MS galaxies at various redshifts.

In order to investigate the dispersion in the $L'_{\text{CO}} - L_{\text{IR}}$ relation, the galaxies are classified as either MS or SB galaxies. This was done by determining the off-set from the MS ($\Delta\text{SFR} = \text{SFR}/\text{SFR}_{\text{MS}}$), where a total of 322 SFGs were included. The majority of MS galaxies from the SFR- M_* relation follow a unique sequence in the $L_{\text{CO}} - L_{\text{IR}}$ relation, whereas the SB galaxies systematically lie above following a different sequence. The results support two distinct modes of SF for SB and MS galaxies, respectively.

CONTENTS

1	Introduction and motivation	3
1.1	Galaxy evolution	3
1.2	The connection between molecular gas and star formation	5
1.3	The main-sequence of galaxies	5
1.4	Star Formation Efficiency	6
1.5	Infrared Galaxies	7
1.6	Summary	8
2	Methods	11
2.1	Measuring molecular gas mass	11
2.1.1	Estimating the molecular gas mass	11
2.1.2	Higher CO excitation levels	12
2.1.3	Measuring Dense Gas	12
2.1.4	Line luminosities	12
2.2	Measuring SFR (L_{IR} and Dust properties)	13
2.2.1	Dust emission	13
2.2.2	Draine & Li (2007) dust models	14
2.2.3	Estimating the dust mass	15
2.3	Measuring the Distance to the Main-Sequence and SFE	15
3	Collecting and processing data	17
3.1	Data overview	17
3.1.1	MySQL database containing the gas measurements	18
3.2	Python scripts	20
3.3	Data processing	22
3.3.1	Combining measurements from various sources	22
3.3.2	Stellar masses	23
3.3.3	Higher J-transitions	23
3.3.4	Gravitationally lensed galaxies	23
3.3.5	Determining SFR/SFR _{MS}	23
3.4	Galaxy surveys	24
3.4.1	COLD GASS	24
3.4.2	GOALS	24
3.4.3	ALLSMOG	24
3.4.4	EGNoG Survey	25
3.4.5	ULIRGs and LIRGs	25
3.4.6	SMGs	26
3.5	<i>Herschel</i> -detected data sample	27

4	Results and discussion	29
4.1	All CO detected galaxies	29
4.2	Distance to the main-sequence	32
4.3	Two modes of star formation	35
4.4	Linking SFE with the off-set from the MS	36
4.5	Dust temperature and dense gas fractions	37
4.5.1	Future perspective	39
5	Conclusion	41
	List of References	42
	List of Figures	52
	List of Tables	53
A	The program	55
A.1	Used software	55
A.1.1	The challenges	55
A.1.2	The building blocks	55
A.2	Selected function declarations	56
A.2.1	cat_reader.try_ned_from_query_name	56
A.2.2	cat_reader.full_name_search_on_query	56
A.2.3	cat_reader.load_excel	57
A.2.4	cat_reader.add_calc_column	57
A.3	Selected python scripts	58
A.3.1	result_builder.py	58
A.3.2	add_cols.py	59
B	Tables	63
B.1	Included telescopes and instruments	63
B.2	<i>Herschel</i> -detected sample	64
C	Figures	67
C.1	<i>Herschel</i> -detected sample	67

1 INTRODUCTION AND MOTIVATION

1.1 GALAXY EVOLUTION

Galaxy evolution is one of the most challenging and mysterious topics in Astrophysics that is still not well-understood, despite several decades of extra-galactic research [Mo et al., 2010]. Understanding the evolution and assembly of stellar populations within these large dynamically bound systems will help us understand how gas clouds are turned into stars through powerful and complex processes that enrich the interstellar medium¹ (ISM) with chemical elements [Sparke & Gallagher III, 2000]. Galaxy formation is essential for enhancing our knowledge of our origins, as the majority of stars eventually form solar systems with habitable planets similar to our own. But how do galaxies, which are the building blocks of the Universe, form and evolve? What factors affect the properties of galaxies and what drives star formation in these systems? How were the majority of stars formed in the Universe? Could all galaxies be correlated even though they span a wide range in both morphology and sizes? How does the intergalactic medium² (IGM) affect galaxy growth and evolution? How do stars form and evolve in various galaxy populations? Understanding these questions provides insight to how structures are formed, and how the Universe as a whole has evolved.

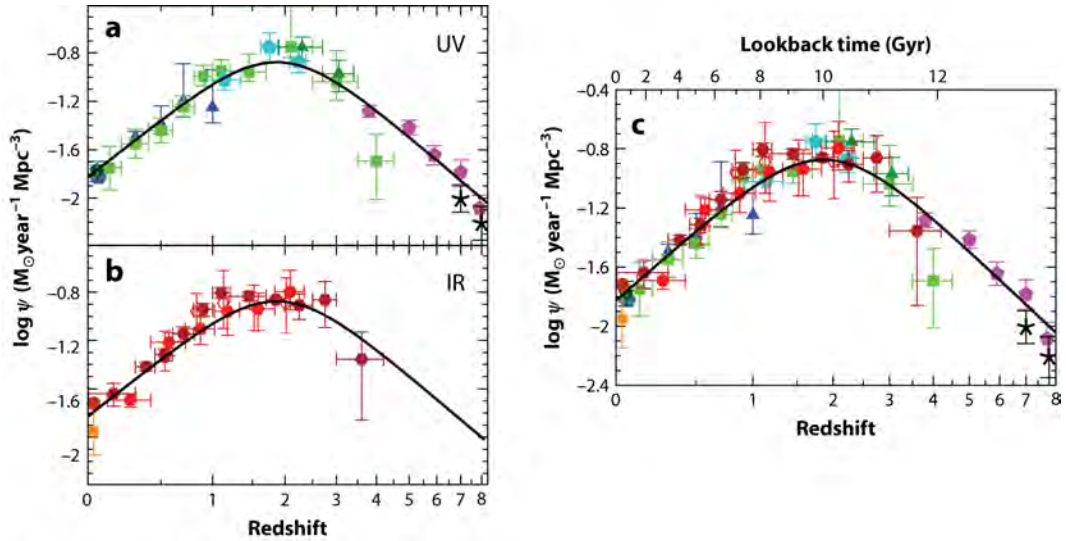
In terms of galaxy evolution, the time scales are significantly larger than the lifetime of a human being. Observations of the evolution of individual galaxies are therefore impossible. However, due to the expansion of the Universe, a distant galaxy will have a larger receding velocity that results in a larger redshift compared to a nearby galaxy. In addition, since light travels at a finite speed, it takes time for the photons to cover large distances. The light from the earliest galaxies has traveled for more than 13 billion years before reaching us on Earth. By taking advantage of this unique property, we are able to observe galaxies at various redshifts, such as when the Universe was younger than its present age and galaxies were less evolved. Since high-redshift galaxies are the progenitors of the present day galaxies, they are important tracers of the evolution of the Universe.

Large galaxy surveys covering a broad range of redshift have been an important tool for understanding how various galaxy populations are forming stars. It has been discovered that the early universe was more active in terms of star formation,

¹The space between stars within a galaxy.

²The space between galaxies.

as galaxies formed the bulk of their stellar mass at redshifts between $z = 1 - 3$, where the cosmic star formation rate density peaked (Figure 1.1). This era is known as the epoch of galaxy assembly, where approximately half of the stars in our present Universe were formed [Carilli & Walter, 2013; Madau & Dickinson, 2014]. The comoving SFR density since this epoch has decreased exponentially, suggesting that the star formation activity was significantly higher in the past, where galaxies on average formed more stars compared to in our present Universe. The cause of this overall decrease in star formation is unknown, although a possible explanation is a higher rate of gas infall from the intergalactic medium onto galaxies that leads to larger amounts of gas and higher star formation rates in galaxies at high redshift. In addition, several physical processes such as transforming gas into stars, the enrichment of material in galaxies and the intergalactic medium, and feedback and cooling are all poorly understood processes that affect the star formation in galaxies. By comparing galaxies at different epochs, the ultimate goal is to understand how galaxies form and evolve with the diversity of sizes, structures, colors, and luminosities that we observe.




 Madau P, Dickinson M. 2014.
Annu. Rev. Astron. Astrophys. 52:415–86

Figure 1.1: The cosmic star formation history in the rest-frame FUV (a), IR (b), and FUV+IR (c). Based on these measurements it is clear that the SFH peaked when the Universe was approximately 3.5 Gyr (between $z = 2$ and $z = 1.5$).

1.2 THE CONNECTION BETWEEN MOLECULAR GAS AND STAR FORMATION

Stars are formed through complex processes in cold, dense clouds of gas that are often concentrated in galactic discs, as is the case in our own Milky Way [Solomon & Bout, 2005]. The gas reservoir within galaxies provides the raw material from which stars are formed and is therefore linked to the star formation rate. They are mainly dominated by neutral and molecular hydrogen, where the latter is thought to precede star formation [Mo et al., 2010]. For the Milky Way and nearby galaxies, the atomic gas (H_I) is organized in clumps with masses of $10^5 - 10^6 M_\odot$ and tens of parsec in size that dominate the diffuse neutral ISM and can be relatively easily observed [Gao & Solomon, 2004b]. In the densest part of the ISM, such as towards the galactic center or in the spiral arms where stars are formed, the molecular form of hydrogen tends to dominate. For galaxies at higher redshifts the atomic gas mass M_{H_I} only accounts for a fraction of the total gas mass meaning $M_{\text{gas}} = M_{\text{H}_\text{I}} + M_{\text{H}_2} \approx M_{\text{H}_2}$, where M_{H_2} is the molecular gas mass [Obreschkow & Rawlings, 2009; Popping et al., 2012].

Schmidt [1959] was the first to observe a power-law relation between the rate of star formation and the volume density of interstellar gas in galaxies. The trend was later confirmed by R. C. Kennicutt Jr. [1989], who observed a correlation between the star formation rate density and the molecular gas density, where star formation is thought to occur. This empirical relation has since been referred to as the Kennicutt-Schmidt (KS) Law, which has proven to be consistent for a large dynamical range of star-forming galaxies [R. C. Kennicutt & Evans, 2012].

1.3 THE MAIN-SEQUENCE OF GALAXIES

An important insight into galaxy evolution was gained when it was observed that the majority of star-forming disk galaxies tend to obey a well-defined correlation between the rate at which they are forming stars (SFR) and their stellar mass (M_*). This relatively narrow trend defines the "main-sequence" of galaxies. It has been observed to exist both in our local universe [Brinchmann et al., 2004; Peng et al., 2010; Salim et al., 2007] and at higher redshift [Daddi et al., 2007; Noeske et al., 2007], where the normalization factor in the SFR- M_* relation increases with redshift. The tightness of this correlation suggests that the majority of stars in galaxies are formed during a secular evolution, where the star formation is fueled by smooth gas accretion [Bouché et al., 2010].

More recent studies have observed outliers with elevated SFRs from this well-defined SFR- M_* correlation, which are classified as starburst galaxies. For a given M_* they contain much larger SFRs and are therefore located above the main-sequence of galaxies. Starbursts are relatively rare systems as they only make up a few percent of the total population [Rodighiero et al., 2011]. The physical explanation of a galaxy's position along the SFR- M_* plane is not fully understood and might be related to how efficiently the gas in the ISM is being converted into

stars.

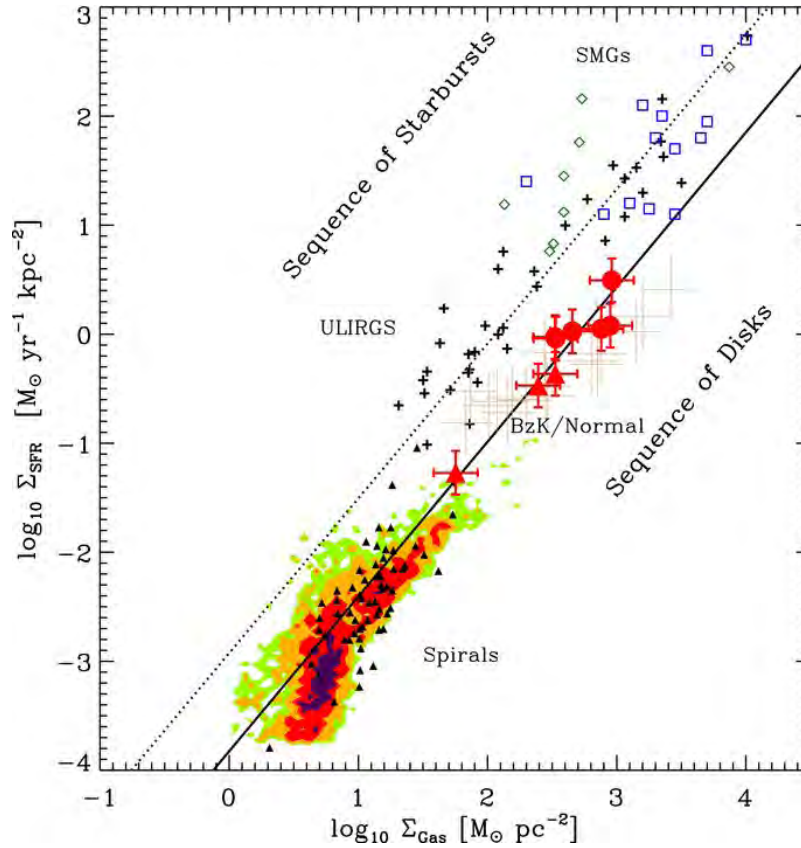


Figure 1.2: Star formation rate density (Σ_{SFR}) versus gas surface density Σ_{Gas} . Two distinct sequences are shown. On the main-sequence most spiral and normal star-forming galaxies are located, whereas ULIRGs and high- z SMGs are systematically located above on a separate sequence. Figure from Daddi et al. [2010].

1.4 STAR FORMATION EFFICIENCY

The star formation efficiency is defined as $\text{SFE} \equiv \text{SFR}/M_{\text{gas}}$, which is the ratio between the rate at which stars are formed and the available amount of gas. The gas depletion timescale, $\tau_{\text{dep}} \equiv M_{\text{gas}}/\text{SFR}$, is the time it would take a galaxy to use up its entire gas reservoir assuming a constant SFR. For a starburst galaxy, its evolutionary stage is thought to be short-lived, due to the high SFRs resulting in a rapid depletion of its gas supply. In our local universe, a main-sequence galaxy typically has a timescale on the order of $\sim 10^9$ yr, whereas a starburst burns up its gas supply much faster resulting in a gas depletion timescale 10-20 times shorter. The significant contrast between a main-sequence galaxy and a starburst suggests they might undergo two distinct modes of star formation. This claim highly depends on observations of the molecular gas, where direct observations of the gas have proven to be challenging.

Molecular gas clouds within galaxies are mainly dominated by molecular hydrogen, which unfortunately does not radiate in the dense regions of the ISM. Molecular CO lines can instead be used to trace the molecular gas. Recent studies of the CO-inferred molecular gas mass suggest that starbursts and main sequence galaxies really do have significantly different SFE [Figure 1.2; Daddi et al., 2010]. However, the difference between starburst and main-sequence galaxies might be enhanced by the bimodal conversion factor, α_{CO} , which is often used to convert CO line emission into the molecular gas mass of a given galaxy. The conversion factor has been found to differ for normal disk galaxies and those that fall above the main-sequence.

In addition, even though the CO line can be observed from the ground, these observations are time intensive. Unfortunately this issue is amplified when studying galaxies in the early universe, where a single galaxy might require several hours of integration. The limitations related to observing the molecular gas therefore means that existing studies of CO detected galaxies are limited to relatively small sample sizes.

1.5 INFRARED GALAXIES

In our local Universe, starburst galaxies are known as Ultra-Luminous InfraRed Galaxies (ULIRGs) dominating in the infrared regions with luminosities exceeding $10^{12} L_{\odot}$. They are dust-obscured gas-rich mergers, where major galaxy merger has compressed the gas enhancing the star formation activity [Sanders & Mirabel, 1996; Veilleux et al., 2009]. Stars formed in local ULIRGs are thought to undergo a more violent and stochastic star formation, triggered by a merger-event.

Large surveys and observations of the cosmic background radiation have revealed that a large fraction of light emitted by galaxies are produced at far-infrared and submillimeter wavelengths, suggesting that infrared bright galaxies might be an important piece in the evolution of galaxies at higher redshift. Even though ULIRGs are uncommon in our local Universe, previous studies have shown that these extreme IR bright galaxies were the dominant population at $z = 2$, where the SFRs in galaxies on average were higher. These galaxies were responsible for the majority of the energy density at this epoch influencing the build-up of stellar mass and dominating the star formation activity [Le Floch et al., 2005]. Figure 1.3 shows the dominant galaxy populations as a function of redshift in terms of comoving infrared energy density. At $z \sim 0$ the LIRGs and ULIRGs do not contribute significantly to the total comoving IR energy density (left axis), which is instead dominated by normal star-forming galaxies. However, at higher redshift the fraction of IR galaxies increase steadily and at $z \sim 2$ becomes the dominant population.

Thus, it is vital to determine how star formation progresses in IR galaxies at higher redshift. Do they resemble local starburst galaxies, where the star formation is driven by major mergers, or are they forming stars in steady processes similar to local disk galaxies on the main sequence? If the majority of galaxies at high- z are related to local ULIRGs, it suggests that starburst galaxies were responsible for the

buildup of stellar mass in the early universe with high star formation efficiencies and short gas depletion timescales. This would imply that stars within galaxies are formed during two modes of star formation: a long, secular evolution with smooth gas accretion, and one rapid, violent with high SFEs. On the contrary, if high- z galaxies reveal similar properties as main-sequence galaxies, the majority of stars in the early universe were formed during a single mode of star formation.

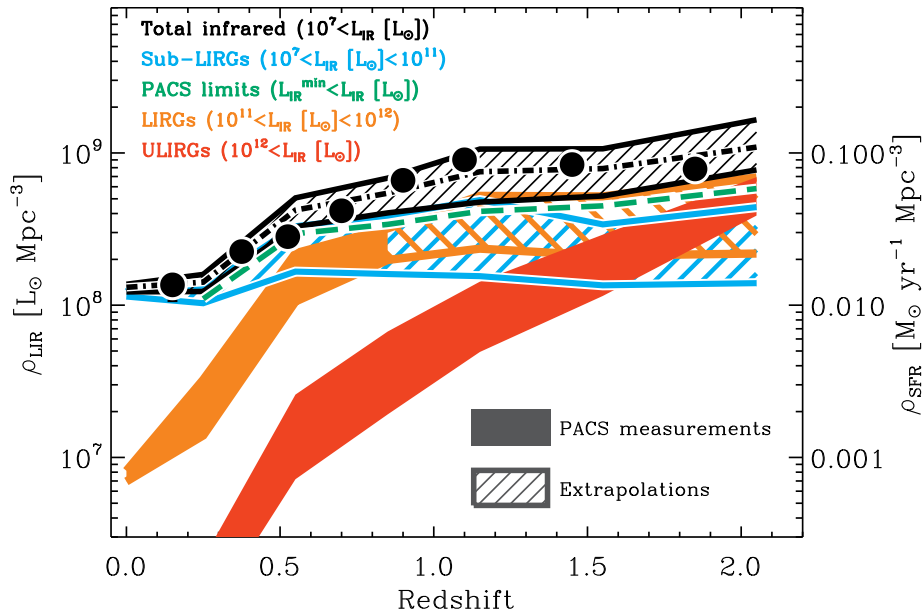


Figure 1.3: The total comoving IR energy density is indicated as the black regions, whereas the blue show the faint galaxies. LIRGs and ULIRGs are represented in orange and red, respectively. The right axis shows the comoving infrared energy density, whereas the right axis represent the obscured SFR density from dust emission. The green line shows the detection limit of PACS, which is a one of the instruments on the Herschel Space Telescope operating at far-IR and submillimeter regions. Figure from Magnelli et al. [2013]

1.6 SUMMARY

The main goal of this work is to determine if two distinct modes of star formation exist. In our local universe the majority of stars are formed during smooth and steady processes in normal disk galaxies. ULIRGs with elevated SFRs and enhanced SFEs are rare systems and only contribute with a small fraction to the buildup of stellar mass. However, this is less clear at higher redshifts, where IR bright galaxies tend to dominate. Since the normalization factor in the $\text{SFR}-M_*$ increases with redshift, it means these IR bright galaxies at high- z are located on the main-sequence. If these high- z main-sequence galaxies resemble local starbursts with merger-driven star formation, it supports the existence of two distinct star formation modes.

In this thesis, the distinction between main-sequence and starburst galaxies will be examined, and how the star formation efficiency of galaxies changes with

redshift. This will be done by studying the SFR (through dust grains) and gas content (CO line emission) in galaxies over a broad range of redshifts.

To overcome the issues related to the small sample sizes of previous studies, all CO detected galaxies from the literature will be collected to create a statistically representative sample that spans a wide dynamical range.

2 METHODS

2.1 MEASURING MOLECULAR GAS MASS

The molecular gas in galaxies is mainly dominated by molecular hydrogen (H_2) in its lowest two rotational states. However, due to symmetry, H_2 lacks a permanent dipole moment meaning its radiative transitions are forbidden and require extremely high temperatures in order to be excited. Since stars are formed in the cold, dense parts of molecular clouds, emission from molecular hydrogen is rarely detected. Therefore, a more preferable gas tracer is often used to observe the diffuse gas. A proper candidate is the rotational lines of carbon monoxide (CO), which is the most abundant molecule within galaxies after H_2 . It has been observed to overlap in the same regions as molecular hydrogen in nearby galaxies, and it is often assumed that the H_2 column density is proportional to the $\text{CO}(1-0)$ surface brightness [Draine et al., 2007]. In addition, the CO molecule has low excitation requirements and can easily be observed from the ground [Carilli & Walter, 2013].

2.1.1 ESTIMATING THE MOLECULAR GAS MASS

From Solomon & Bout [2005] the CO line luminosity can be converted into an H_2 mass using

$$M(\text{H}_2) = \alpha_{\text{CO}} L'_{\text{CO}} \quad (2.1)$$

where α_{CO} is the highly-debated CO - M_{gas} conversion factor. For the Milky Way $\alpha_{\text{CO}} \equiv 4.6 M_{\odot} (\text{K km s}^{-1} \text{pc}^2)^{-1}$. However, the conversion factor seems to differ for various environments and galaxy populations influencing the resulting estimated gas mass [Bolatto et al., 2013; Casey et al., 2014; Downes & Solomon, 1998]. For ULIRGs and EMGs a value of $\alpha_{\text{CO}} = 4.6 M_{\odot} (\text{K km s}^{-1} \text{pc}^2)^{-1}$ results in gas masses greater than the dynamical mass (Bryant & Scoville 1999). Derivations of the conversion factor have instead suggested $\alpha_{\text{CO}} \sim 0.8 M_{\odot} (\text{K km s}^{-1} \text{pc}^2)^{-1}$ for "starbursty" galaxies such as SMGs and QSO hosts, whereas for disk galaxies $\alpha_{\text{CO}} \sim 4 M_{\odot} (\text{K km s}^{-1} \text{pc}^2)^{-1}$ is recommended [Bolatto et al., 2013]. In addition, it appears that the conversion factor rises in low-metallicity environments at high- z , which could be due to CO photodissociation [Casey et al., 2014; Genzel et al., 2012; Tan et al., 2013]. This indicates that the conversion factor highly depends on environmental parameters including gas density and temperature.

2.1.2 HIGHER CO EXCITATION LEVELS

Observations of the molecular gas at high redshifts are often based on emission from CO lines with rotational quantum numbers higher than $J = 1$ [Carilli & Walter, 2013]. Table 2.1 lists the rest frequency of common excitation levels of the CO molecule observed in galaxies. The listed values are from Carilli & Walter [2013].

J -transition	1 – 0	2 – 1	3 – 2	4 – 3	5 – 4	6 – 5	7 – 6
ν_{CO} [GHz]	115.27	230.54	345.80	461.04	576.27	691.47	806.65

Table 2.1: Rest frequencies for various J transitions of the CO molecule.

CO can be excited to higher states through collisions with other molecules in the gas and through radiative absorptions. The CO excitation ladder is known as the CO Spectral Line Energy Distribution (CO SLED) [Carilli & Walter, 2013]. These thermal excitations can be described by the Boltzmann distribution. Since the total molecular gas mass is determined using a conversion factor based on emission from the $J = 1 - 0$ transition, higher CO line transitions have to be converted. The assumed conversion scheme listed in Table 2.2 is from Bothwell et al. [2013], where $r_{J,J-1/10}$ is the ratio of CO luminosities $L'_{\text{CO}(J,J-1)}/L'_{\text{CO}(1-0)}$.

Rotational transition	Value
$r_{21/10}$	0.84 ± 0.13
$r_{32/10}$	0.52 ± 0.09
$r_{43/10}$	0.41 ± 0.07
$r_{54/10}$	0.32 ± 0.05
$r_{65/10}$	0.21 ± 0.04
$r_{76/10}$	0.18 ± 0.04

Table 2.2: Conversion factors for higher CO rotational states.

2.1.3 MEASURING DENSE GAS

A commonly used proxy for denser molecular gas within galaxies is HCN, which traces gas at densities $n(\text{H}_2) \gtrsim 3 \times 10^4 \text{ cm}^{-3}$ [Gao & Solomon, 2004a]. It has a higher dipole moment than CO and is thought to be more closely associated with the star-forming regions within giant molecular clouds [Gao & Solomon, 2004b]. One disadvantage of using HCN is that the line emission is often 10 – 20 times weaker than CO [Gao & Solomon, 2004a].

2.1.4 LINE LUMINOSITIES

The spectral line emission is often expressed either as L_{line} or L'_{line} , where the former is given in units of L_{\odot} and the latter is expressed via the areal integrated

source brightness temperature and is given in units of $\text{K km s}^{-1} \text{ pc}^2$. The L_{line} is the power that is being emitted through a given line which therefore can be used to calculate the cooling capability (in relation to the FIR luminosity $L_{\text{line}}/L_{\text{FIR}}$). Solomon & Bout [2005] find that the CO line luminosity in units of L_{\odot} (the power that is being emitted through a CO line) can be estimated from:

$$L_{\text{CO}} = 1.04 \times 10^{-3} S_{\text{CO}} \Delta v \nu_{\text{rest}} (1+z)^{-1} D_L^2 \quad (2.2)$$

where $S_{\text{CO}} \Delta v$ is the velocity integrated flux in Jy km s^{-1} , $\nu_{\text{obs}} = \nu_{\text{rest}}/(1+z)$ is the observed frequency of the line in GHz, $D_L = D_A(1+z)^2$ is the luminosity distance in Mpc where D_A is the angular size diameter and z is the redshift of the source. The CO line luminosity in units of $\text{K km s}^{-1} \text{ pc}^2$ is given as

$$L'_{\text{CO}} = 3.25 \times 10^7 S_{\text{CO}} \Delta v \nu_{\text{obs}}^{-2} D_L^2 (1+z)^{-3} \quad (2.3)$$

or

$$L'_{\text{CO}} = 23.5 \Omega_{\text{s}^* \text{b}} D_L^2 I_{\text{CO}} (1+z)^{-3} \quad (2.4)$$

where $\Omega_{\text{s}^* \text{b}}$ is the solid angle of the source convolved with the telescope beam, and I_{CO} is the observed integrated line intensity measuring the beam diluted brightness temperature $I_{\text{CO}} = \int T_{\text{mb}} dv$. The main-beam brightness temperature is $T_{\text{mb}} = T_A^* (F_{\text{eff}}/B_{\text{eff}})$ where T_A^* is the antenna temperature and F_{eff} , B_{eff} are the forward and effective beam efficiencies, respectively.

An alternative way to determine L'_{CO} is

$$L'_{\text{CO}} = \frac{\Omega_{\text{b}} D_L^2 I_{\text{CO}}}{(1+z)^3} \quad (2.5)$$

where Ω_{b} is the beam solid angle $\Omega_{\text{b}} = \pi \theta_{\text{B}}^2 / (4 \times \ln 2)$ and θ_{B} is the main beam size [Morokuma-Matsui et al., 2015].

2.2 MEASURING SFR (L_{IR} AND DUST PROPERTIES)

2.2.1 DUST EMISSION

Thermal dust emission peaks at rest-frame wavelengths $\lambda \sim 40 - 200 \mu\text{m}$ and dominates the FIR SED in dusty star forming galaxies. Therefore, in order to probe the bulk of the infrared emission, it is necessary to select galaxies with sufficient photometric FIR observations. By fitting the IR and FIR part of a galaxy's SED, it is possible to obtain several physical parameters including the total IR luminosity, L_{IR} , and the total dust mass within the galaxy M_{dust} . In the following I will describe a dust model, which can be used to model the thermal region of a galaxy's SED. All calculations are determined assuming a cosmology of $\Omega_{\text{m}} = 0.3$, $\Omega_{\Lambda} = 0.7$, and $H_0 = 70 \text{ km s}^{-1} \text{ Mpc}^{-1}$.

2.2.2 DRAINE & LI (2007) DUST MODELS

The FIR part of a galaxy's SED can be fitted using Draine & Li [2007] (DL07) dust models, assuming the interstellar dust is a mixture of carbonaceous and amorphous silicate grains with the same properties as polycyclic aromatic carbonaceous molecules (PAHs) and size distributions similar to the extinction law in the Milky Way, Large Magellanic Cloud, or Small Magellanic Cloud. The dust distribution can be found in two different regions: the diffuse ISM and enclosed in photo-dissociation regions (PDRs) [Draine & Li, 2007]. In the diffuse ISM, which contains the dominant amount of dust, the dust is heated by a radiation field of constant intensity noted as U_{\min} . Only a fraction of the dust (γ) is trapped within the PDRs, and is therefore exposed to starlight with an intensity range between U_{\min} to U_{\max} . However, dust that is enclosed in the PDR regions can contribute the majority of dust emission at mid-IR wavelengths. The sum of the diffuse ISM model and the PDR model then gives:

$$\frac{dM_{\text{dust}}}{dU} = (1 - \gamma)M_{\text{dust}}\delta(U - U_{\min}) + \gamma M_{\text{dust}} \times \frac{\alpha - 1}{U_{\min}^{\alpha-1} - U_{\max}^{\alpha-1}} \times U^{-\alpha} \quad (2.6)$$

where dM_{dust} is the dust mass heated by starlight intensities in the range $[U, U + dU]$, $(1 - \gamma)$ is the fraction of dust exposed to a starlight intensity of U_{\min} , δ is the delta function representing the diffuse interstellar radiation field of intensity $U = U_{\min} = U_{\max}$, α is a power-law index, and M_{dust} is the total dust mass. A range of dust to gas ratios from Draine & Li [2007] are used for each model and the radiation intensities range from $0.80 < U < 25.0$.

The emission spectrum of the two models at a distance D is then a linear combination

$$f_{\nu}^{\text{model}} = \frac{M_{\text{dust}}}{4\pi D^2} [(1 - \gamma)p_{\nu}^{(0)} + \gamma p_{\nu}] \quad (2.7)$$

where $p_{\nu}^{(0)} = p_{\nu}^{(0)}(q_{\text{PAH}}, U_{\min})$ and $p_{\nu} = p_{\nu}(q_{\text{PAH}}, U_{\min}, U_{\max}, \alpha)$ are the emitted power per unit frequency per unit dust mass for dust heated by starlight intensity U_{\min} , and dust heated by a power-law distribution of starlight intensities $dM/dU \propto U^{-\alpha}$ in the range from U_{\min} to U_{\max} , respectively. The DL07 model includes a total of 6 free parameters; q_{PAH} , U_{\min} , U_{\max} , α , γ , and M_{dust} . In Draine et al. [2007] they discovered after studying 65 SINGS galaxies that a fixed value of $\alpha = 2$ and $U_{\max} = 10^6$ would not change the individual galaxy SED significantly. I have therefore chosen to set these two parameters to the above values. The total model returns the remaining parameters, where the goodness of the fit is determined by performing a reduced χ^2 given by

$$\chi_{\nu}^2 = \frac{\chi^2}{\nu} = \frac{1}{\nu} \sum \frac{(O - E)^2}{\sigma^2} \quad (2.8)$$

where χ^2 is the weighted sum of squared errors, O is the observed quantify, E is the expected values, and ν is the number of degrees of freedom.

The L_{IR} is then estimated as the integrated emission in the wavelength range of $8\mu\text{m}$ to $1000\mu\text{m}$

$$L_{\text{IR}} = \int_{8\mu\text{m}}^{1000\mu\text{m}} L_{\nu}(\lambda) \frac{c}{\lambda^2} d\lambda \quad (2.9)$$

with the rest-frame luminosity, $L_{\nu}(\lambda) = 4\pi D_L^2 S_{\nu}(\lambda)$, where D_L is the luminosity distance of the galaxy and $S_{\nu}(\lambda)$ is the flux density.

The infrared luminosity is a measure of the energy, mainly from star formation, that was absorbed by dust. An L_{IR} measurement is therefore directly proportional to the absorbed fraction of energy arising from star formation. The obscured star formation rate, SFR_{IR} (hereafter SFR) can be estimated using the following conversion listed in R. C. Kennicutt Jr. [1998]

$$\text{SFR}_{\text{IR}} = 1.72 \times 10^{-10} \times L_{\text{IR}} \quad (2.10)$$

in units of $M_{\odot} \text{ yr}^{-1}$ and where a Chabrier [2003] IMF is assumed.

2.2.3 ESTIMATING THE DUST MASS

The dust mass is determined using

$$M_{\text{dust}} = \left(\frac{M_{\text{dust}}}{M_{\text{H}}} \right) m_{\text{H}} \frac{L_{\nu}}{4\pi j_{\nu}} \quad (2.11)$$

where $M_{\text{dust}}/M_{\text{H}}$ is the dust-hydrogen ratio of the dust models from Draine & Li [2007]. The dust mass absorption coefficient is set to $\kappa_0 = 5.1 \text{ m}^2 \text{ kg}^{-1}$. The ratio $L_{\text{IR}}/M_{\text{dust}}$ is proportional to the mean radiation field $\langle U \rangle$ and is a proxy for the gas temperature.

2.3 MEASURING THE DISTANCE TO THE MAIN-SEQUENCE AND SFE

Several SFR indicators can be used to determine the star formation rate, such as the infrared luminosity, which provides a measure of the energy from stars that has been absorbed by dust grains. It therefore traces the obscured star formation within galaxies. The interstellar dust grains absorb the UV light from newly formed O and B stars and re-radiates it thermally at far-infrared wavelengths, meaning the FIR emission of a dusty galaxy can be used as a tracer for its current SFR.

The SFR of main-sequence galaxies varies with redshift and stellar mass [Noeske et al., 2007; Speagle et al., 2014]. It can be determined by using the following expression from Schreiber et al. [2015]:

$$\log \text{SFR}_{\text{MS}} [M_{\odot} \text{ yr}^{-1}] = m - m_0 + a_0 r - a_1 [\max(0, m - m_1 - a_2 r)]^2, \quad (2.12)$$

where $r \equiv \log(1 + z)$, $m \equiv \log(M_*/10^9 M_{\odot})$, $m_0 = 0.50 \pm 0.07$, $a_0 = 1.50 \pm 0.15$, $a_1 = 0.30 \pm 0.08$, $m_1 = 0.36 \pm 0.30$, and $a_2 = 2.50 \pm 0.60$. The distance of a galaxy

with respect to the main-sequence is expressed as the ratio $\Delta\text{SFR} \equiv \text{SFR}/\text{SFR}_{\text{MS}}$, and a galaxy is considered to be located on the main-sequence if $1/3 < \Delta\text{SFR} < 3$, whereas galaxies with $\Delta\text{SFR} < 1/3$ and $\Delta\text{SFR} > 3$ are classified as quiescent and starburst galaxies, respectively. Eq. 2.12 is based on a sample of galaxies with mass bins with widths of 0.3 dex.

The star formation efficiency is defined as the ratio between a galaxy's current SFR and the available amount of gas

$$\text{SFE} = \frac{\text{SFR}}{M_{\text{gas}}} \propto \frac{L_{\text{IR}}}{L'_{\text{CO}}} \quad (2.13)$$

where $L_{\text{IR}}/L_{\text{CO}}$ is in units of $L_{\odot}/(\text{K km s}^{-1} \text{ pc}^2)$. The gas consumption timescale is given as $\tau_{\text{gas}} = 1/\text{SFE}$, which is the time it takes for a galaxy to use up its entire gas reservoir with the current SFR [Carilli & Walter, 2013].

3 COLLECTING AND PROCESSING DATA

3.1 DATA OVERVIEW

To obtain a broad dynamical range of star-forming galaxies at both high and low redshift, all CO detected galaxies from the literature with direct measurements of the molecular gas mass are collected. For this purpose I built a MySQL database to store the data. Additional emission lines measurements are saved including CO, HCN, and [CII] from a variety of large galaxy surveys such as the COLDGASS, GOALS, EGNOC, among others.

The L_{CO} values for the full data sample are drawn from Bauermeister et al. [2013], Bothwell et al. [2013], Bothwell et al. [2014], Carilli & Walter [2013] (and references therein), Evans et al. [2006], Gao & Solomon [2004a,b], García-Burillo et al. [2012], Graciá-Carpio et al. [2006], Graciá-Carpio et al. [2008], Juneau et al. [2009] (HCN data are from Bussmann et al. [2008]), Magdis et al. [2012], Magdis et al. [2014], Morokuma-Matsui et al. [2015], Saintonge, Kauffmann, Kramer, et al. [2011], Sharon et al. [2016], Silverman et al. [2015], Solomon et al. [1997], Tacconi et al. [2013], and Zavala et al. [2015] (see the following section for details about each data set).

Figure 3.1 illustrates how each data sample was collected and cross-matched with the NASA/IPAC Extragalactic database³. The additional databases were used to search for specific published galaxy properties including flux measurements, spectroscopic redshifts, stellar mass measurements, and infrared luminosities. In the following sections, I describe the most important tools developed in Python and MySQL in order to create the final catalog

- MySQL database collecting data from NED, ViZieR, Simbad, and IRSA
- Python scripts extracting, converting, and correcting data

The most important scripts are described in Appendix ??.

³The NASA/IPAC Extragalactic Database is operated by the Jet Propulsion Laboratory, California Institute of Technology, under contract with the National Aeronautics and Space Administration.

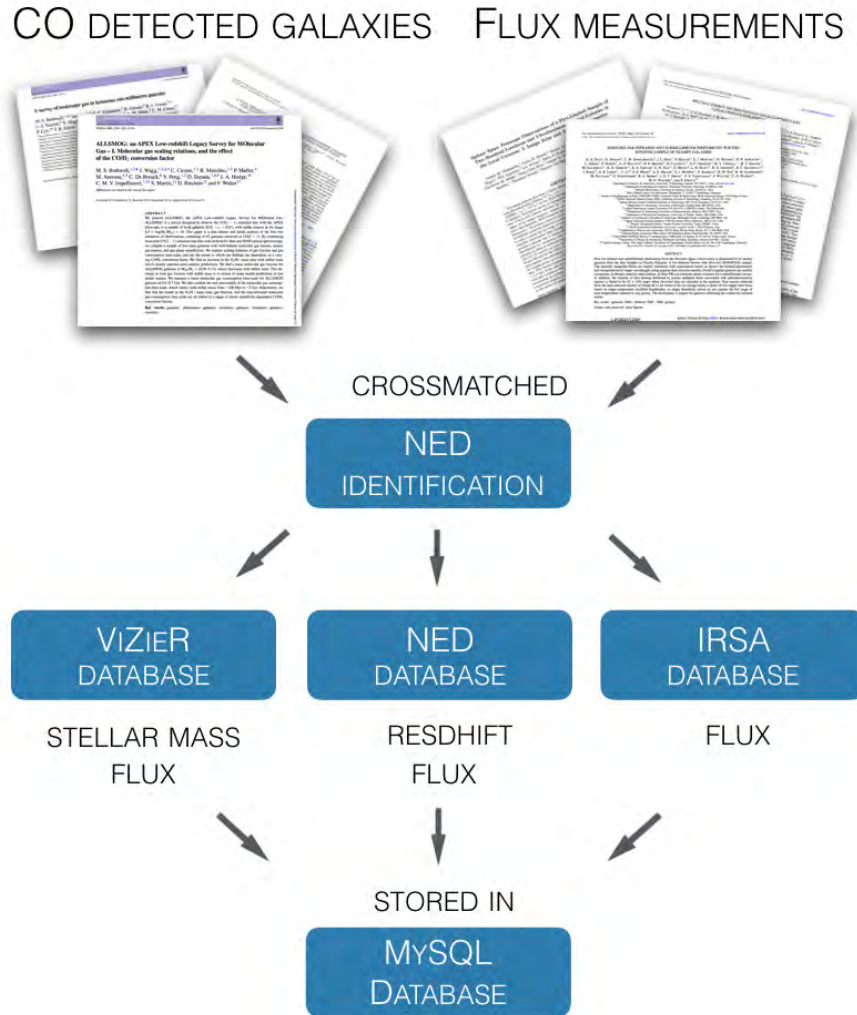


Figure 3.1: A schematic overview of the data collection and combining measurements from the NED, ViZier, and IRSA database. Each CO detected galaxy and flux measurements was cross-matched with the NED database and stored in the MySQL database.

3.1.1 MySQL DATABASE CONTAINING THE GAS MEASUREMENTS

The database contains the raw data measurements (in various units) extracted directly from the published papers or online data tables. The individual data samples are stored in a MySQL views. To obtain a fairly consistent catalog, a range of important parameters was required for each sample before being included in the final data set. For every data set or measurement used the galaxy’s ID name (`ref_name`), coordinates (`ra,dec`), reference (`src`), line and transition (`line`), and redshift or distance are listed (`z,dist`). In addition, the telescope which was used during the observation to measure the line luminosity. This was in particular important if the line measurement was given in units of antenna temperature and therefore needed to be converted into a line luminosity. Furthermore, each CO

detected galaxy in the MySQL database was also matched with the NED database using either the coordinates of the galaxy or by its given ID name listed in the paper. I decided to use the official NED name for the source in order to avoid adding a galaxy to the database multiple times (which could occur if a given galaxy has multiple official ID names). If the galaxy is identified in the NED database and contains numerous names, these would be stored and linked to the official NED name along with information about the galaxy's redshift, distance, coordinates, and photometry measurements (See Section 3.2 for further details).

LOCAL GALAXIES

Among the nearby galaxies, there was a possibility that the physical size of a given galaxy was larger than the beam-size of the telescope. Some of the observed line measurements would then only cover a particular region of a galaxy, if no mapping was completed. Since the scientific goal addresses global star formation laws and processes in galaxies, only L_{IR} measurements based on the galaxy's entire disc was considered. In addition, complications would arise during the following analysis such as determining star formation efficiencies. If a line measurement for a giving galaxy only covers the central regions of its galactic disk, a comparison between the SFR and the molecular gas mass would be insufficient. Therefore, in order to avoid this issue, each line and infrared measurements was listed with a `g_flag` note are listed with values ranging from 0 to 3:

- 0: the line measurement covers the entire galaxy
- 1: the emission is measured from a region of the galactic disc
- 2: the line measurement has been aperture corrected
- 3: the line measurement traces the emission from the entire galaxy obtained through mappings

If `m_flag` \neq `null` then the line measurement is a combination of several observations, where the mapped line measurements are linked together by the same `m_flag` value. (For example the CO reservoir of a nearby galaxy can be obtained through several mappings, where the total line emission then is the integrated CO flux density). Upper and lower limits are marked as `g_limit` = 0 and 1, respectively. Galaxies listed with `g_limit` = 1 indicate galaxies where additional mapping of the galaxy is needed to determine the total line emission of the entire galactic disc. These galaxies are excluded from the final catalog but are stored in the database.

DISTANT GALAXIES

For the high- z galaxies, there was a possibility that some sources might be affected by gravitational lensing due to a massive foreground object. This effect distorts the emitted light from the galaxy, which can influence the data analysis (especially

if the magnification factor was not well-determined). `magn` lists the magnification factor as provided in the reference paper. See Section 3.3.4 for further details.

LINE MEASUREMENTS

During the process of combining all line measurements of the CO detected galaxies, it was found that the detected line emission typically was listed as one of the following

- `l_line`, `l_line_err`: The line luminosity (and error) in $[L'_{\text{line}}] = \text{K km s}^{-1} \text{ pc}^2$
- `i_line`, `i_line_err`: The line intensity (and error) given in $[I_{\text{line}}] = \text{K km s}^{-1}$
- `sdv`, `sdv_err`: The velocity integrated flux density (and error) in $[S\Delta v] = \text{Jy km s}^{-1}$

Line measurements listed as either a line intensity or a velocity integrated flux density were converted to a line luminosity using eq. 2.4 or eq. 2.3, respectively. For galaxies with line emission in units of antenna temperature, the measurement was converted to a line luminosity if a continuum sensitivity on the T_{mb} scale was provided in the paper. These were then converted from a temperature-dependent value to a flux measurement for a point source ($[S/T_{\text{mb}}] = \text{Jy K}^{-1}$.)

3.2 PYTHON SCRIPTS

In order to estimate L_{IR} and M_{dust} measurements using the Draine et al. [2007] dust models (Section 2.2.2), sufficient flux measurements covering a wide range of wavelengths are crucial. Figure 3.2 shows template of a galaxy SED at various redshift. A galaxy at high redshift is shifted towards longer wavelengths, where far-IR and submillimeter flux measurements are essential in order to cover the thermal region, where the dust emission dominates.

Flux measurements (and stellar masses if they were listed) were used from selected papers including Dale et al. [2012], Mazzarella et al. (in prep.), Melbourne et al. [2012], Magdis et al. [2012], U et al. [2012], and Zavala et al. [2015]. In addition, both PACS and SPIRE flux catalogs have been cross-matched with the CO detected galaxies stored in MySQL. Furthermore, several online databases were used to extract additional flux values. The following telescopes and instruments were included: 2MASS, APEX (LABOCA), *Herschel Space Observatory* (SPIRE and PACS), IRAS, Planck, *Spitzer Space Telescope* (IRAC and MIPS), JCMT (SCUBA 1 and 2), and WISE (W1-W4). Table B.1 in Appendix lists the telescope with their instruments and relevant wavebands. Figure 3.3 illustrates the flux coverage. Flux measurements and stellar masses were extracted from several databases including NED, ViZieR, and IRSA. The ViZieR consists of a more than 13,000 published catalogues and data tables⁴, whereas IRSA contains science products

⁴For additional information: <http://vizier.cfa.harvard.edu/index.gml>

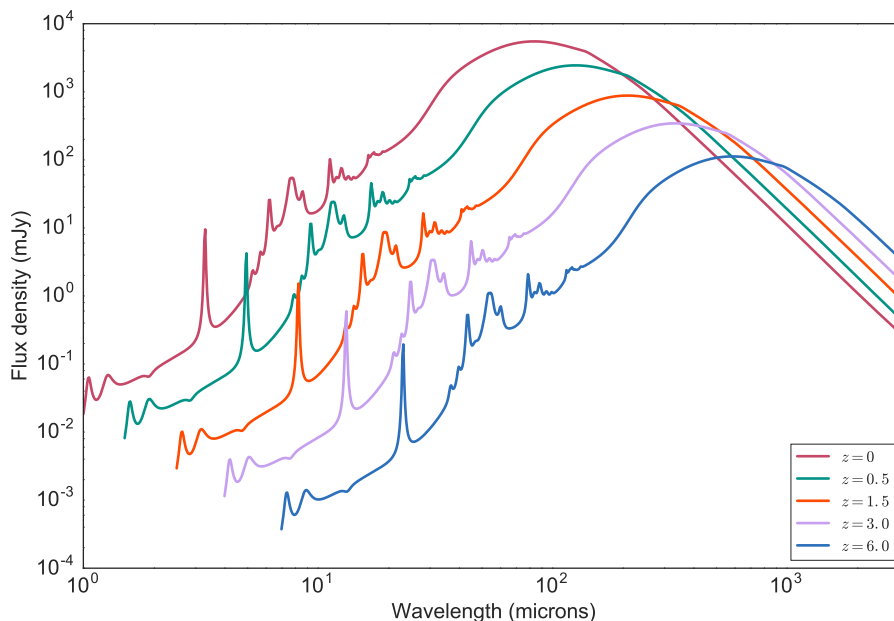


Figure 3.2: SED template of a galaxy at various redshift.

of NASA's infrared and submillimeter missions including archives with data from 2MASS, Spitzer, WISE, Herschel, and the COSMO sample⁵.

In order to extract these data measurements, I wrote several Python scripts to store each result and cross match them with the catalog stored in MySQL. These scripts use Astroquery⁶ to obtain the relevant information including diameter, coordinates, alternative names and photometry values which are inserted into MySQL tables and views. For a given data set with listed galaxies and their respective coordinates, the `try_ned_from_query_name` function in Python uses the reference name from a given list to search in the NED database. If the input name gives a match, the official NED name of the object is saved along with redshift, diameter, photometry, position, references, and notes. These are all saved in different views in MySQL (for example `ned_diameters_v` and `ned_photometry_v` for the diameter and photometry measurements, respectively). The NED name or coordinates is then used to search in the additional databases; Simbad, ViZier, and IRSA.

For example all Simbad outputs are saved in a MySQL view as `simbad_table_v` similar for the ViZier outputs, which are saved as `vizier_tablename_v`. For the IRSA database the script is written to complete a cone search within a radius of 2 arcsec for nearby galaxies, and 10 arcsec for galaxies at higher redshift. This is done using the function `full_name_search_on_query` in Python. If a galaxy was found in one or several IRSA catalogs, the extracted results from the IRSA database will be saved into MySQL view(s) with the following structure: `IRSA_catalogue_v` where `catalogue` is the catalogue code (the most relevant modules are explained in Appendix A). For every completed galaxy search, a log will automatically be saved. This procedure is performed regardless of the search

⁵More information about IRSA: <http://irsa.ipac.caltech.edu/frontpage/>

⁶<http://astroquery.readthedocs.org/>

was successful in order to avoid searching for a galaxy within a given database more than once.

3.3 DATA PROCESSING

3.3.1 COMBINING MEASUREMENTS FROM VARIOUS SOURCES

FLUX MEASUREMENTS

In order to obtain a consistent data sample, all flux measurements in the final catalog is stored in units of Jy. Since several catalogs in IRSA were listed in units of mag, those were converted using the following conversion

$$F_\nu = F_0 \times 10^{-\left(\frac{f_{\text{mag}}}{2.5}\right)} \quad (3.1)$$

where f_{mag} is the flux magnitude in a specific band, and F_0 is the corresponding zero magnitude flux density in Jy.

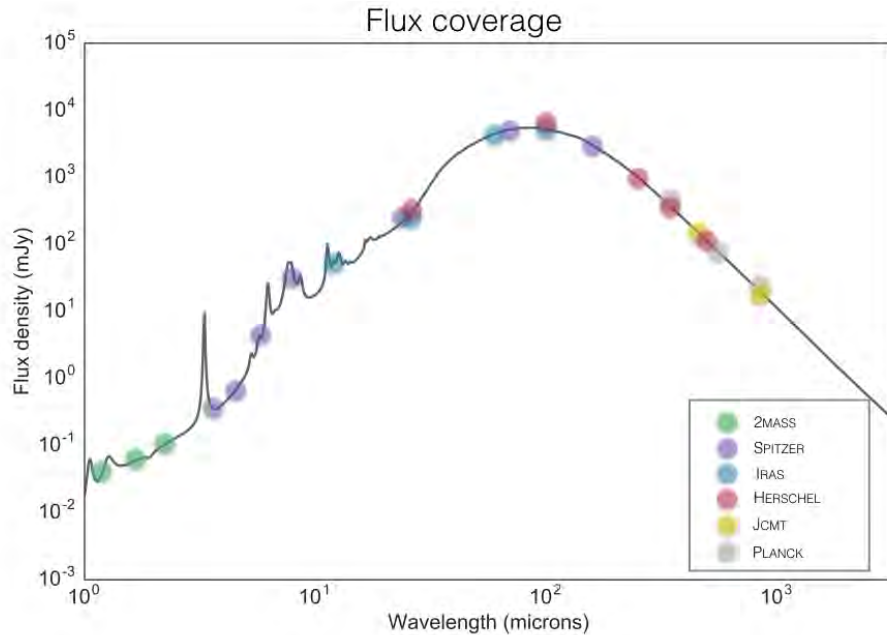


Figure 3.3: Included telescopes and instruments and their individual wavebands shown on a galaxy SED template at $z = 0$.

Figure 3.3 shows the wavelength coverage of the selected instruments for a typical star-forming dusty galaxy SED at low redshift. Photometric observations are often detected in different wavebands, where the observed flux will be affected by the transmission of the waveband filter, the atmospheric transmission, and the telescope and instrument efficiency [Mo et al., 2010]. Transmission curves for each flux value is used to calibrate the measurements during the SED fitting procedure (The majority is available on: <http://svo2.cab.inta-csic.es/svo/>

theory/fps3/index.php?mode=browse&gname=Herschel). A weighted mean is calculated if a galaxy contains multiple flux densities and error estimates from the same telescope or instrument in a given waveband. The weighted mean is determined using

$$\mu = \frac{\sum x_i / \sigma_i^2}{\sum 1 / \sigma_i^2} \quad (3.2)$$

where the error of the weighted mean is defined as

$$\sigma^2(\mu) = \frac{1}{\sum 1 / \sigma_i^2} \quad (3.3)$$

3.3.2 STELLAR MASSES

Since the stellar mass values were collected from various sources and databases, only those with an IMF of either a Chabrier [2003], Kroupa [2001] or Salpeter [1955] IMF are included. The stellar masses are corrected to a Chabrier [2003] IMF using the conversion given in Speagle et al. [2014]: $M_{*,C} = M_{*,S}/1.7 = M_{*,K}/1.06$, where $M_{*,S}$ and $M_{*,K}$ are stellar masses obtained using a Kroupa [2001] or Salpeter [1955] IMF, respectively.

3.3.3 HIGHER J-TRANSITIONS

To obtain a consistent sample all CO line measurements are stored as CO(1 – 0). Galaxies detected with a higher CO rotational excitations are therefore converted to an estimated ground state CO(1 – 0) measurement (Section 2.1.2). Table 2.2 from [Bothwell et al., 2013] is used to correct the higher CO line luminosities.

3.3.4 GRAVITATIONALLY LENSED GALAXIES

If the galaxy is gravitationally lensed the emitted light has been distorted meaning the given L'_{CO} and L_{IR} will be the apparent luminosity. For a lensed galaxy, the intrinsic luminosity can be obtained using $L'_{int} = L'_{app}/\mu$, where μ is the magnification factor of the gravitational lens [Solomon & Bout, 2005]. For the lensed galaxies in the final catalog both the line luminosity and the infrared/far-infrared luminosity are corrected (the magnification factors used are listed in the database along with a link to the original paper).

3.3.5 DETERMINING SFR/SFR_{MS}

Galaxies listed with either L_{IR} or FIR are converted into SFR in order to calculate the off-set from the main-sequence. FIR luminosities obtained from the literature is converted assuming the following relation L_{FIR} : $L_{IR} = 1.3 \times L_{FIR}$ [García-Burillo et al., 2012]. The infrared luminosities is converted to SFR using eq. 2.10 in Section 2.2.2. The SFR_{MS} is determined using eq. 2.12 from Schreiber et al. [2015].

3.4 GALAXY SURVEYS

Large galaxy surveys such as the Sloan Digital Sky Survey (SDSS), All-Wavelength Extended Groth Strip International Survey (AEGIS), and the COLD GASS survey have covered large areas of the sky in order to obtain a representative sample of galaxies at both high and low redshifts. In the following section each sub-sample is described including dynamical ranges and selection criteria (color-selection, flux limitations etc.)

3.4.1 COLD GASS

For nearby galaxies COLDGASS (CO Legacy Data base) has been used which is a subsample of the GASS survey (GALEX Arecibo SDSS Survey); designed to measure neutral hydrogen in a large, unbiased sample of approximately 1000 massive galaxies (with $M_* > 10^{10} M_\odot$ [Saintonge, Kauffmann, Kramer, et al., 2011]). The survey contains CO(1-0) line measurements for ~ 360 nearby galaxies ($0.025 < z < 0.05$) with stellar masses in the range $10^{10} - 10^{11.5} M_\odot$. Huang & Kauffmann [2014].

Saintonge, Kauffmann, Kramer, et al. [2011]; Saintonge, Kauffmann, Wang, et al. [2011] The data sample consists of 164 CO(1-0) detected galaxies with optical redshifts ($0.002 < z_{\text{opt}} < 0.09$), stellar masses ($\log(M_*)$), observed flux in the central pointing ($S_{\text{dv}_{\text{obs}}}$), extrapolated total flux ($S_{\text{dv}_{\text{cor}}}$), and the coordinates (RA and DEC in degrees). Observations are from the IRAM 30m and all galaxies are classified as ULIRGs or LIRGs. Upper limits were given as $\log M_{\text{HII}}$ with $\alpha_{\text{CO}} = 3.2$. The line luminosities were then calculated using the relation $L'_{\text{CO}} = M_{\text{HII}}/\alpha_{\text{CO}}$.

3.4.2 GOALS

The Great Observatories All-Sky LIRG Survey (GOALS) combines several observatories including NASA's Spitzer Space Telescope, Chandra X-Ray Observatory, Hubble Space Telescope (HST), Galaxy Evolution Explorer (GALEX), and ground-based data Armus et al. [2009]. The survey consists of imaging and spectroscopic data of more than 200 low-redshift ($z < 0.088$) LIRGs from IRAS Revised Bright Galaxy Sample (RBGS).

3.4.3 ALLSMOG

The ALLSMOG survey traces the cold molecular gas reservoir by detecting the CO(2-1) in local galaxies ($0.01 < z < 0.03$) with stellar masses $10^8 < M_* < 10^{10} M_\odot$. The data set contains selected galaxies from the MPA-JHU catalogs (from SDSS DR7) [Bothwell et al., 2014].

Bothwell et al. [2014] The data sample contains 42 galaxies. As the APEX beam at 230 GHz has a size of ~ 27 arcsec, only galaxies with a physical size smaller than the beam size was considered. However, a few galaxies have slightly larger optical extents where most of the CO emitting regions are covered by the telescope beam. These are corrected with an aperture correction factor. Beam coverage in percentage are listed in the table. Non-detected CO galaxies are listed with a CO flux density 3σ upper limit $S_{\text{CO}} < 3\sigma\sqrt{\Delta V_{\text{CO}}dv}$.

3.4.4 EGN0G SURVEY

The EGN0G survey (Gas in Normal Galaxies) at the Combined Array for Research in Millimeter-wave Astronomy (CARMA) traces the molecular gas in 31 galaxies from $z = 0.05$ to $z = 0.5$ by observing rotational lines of the CO molecule [Bauermeister et al., 2013]. The full sample is split into four redshift bins; A: $z = 0.05 - 0.1$, B: $z = 0.16 - 0.20$, C: $z = 0.28 - 0.32$, and D: $z = 0.47 - 0.53$. The galaxies were selected from the parent samples, SDSS and COSMOS, to be as representative as possible of the main-sequence of SFGs. The stellar mass range for these galaxies is $(4 - 30) \times 10^{10} M_{\odot}$.

Bauermeister et al. [2013] use the EGN0G C sample with CO(1-0) and CO(3-2) detection of 24 galaxies. The galaxies are selected from $0.05 < z < 0.5$ with stellar masses in the range $(4 - 30) \times 10^{10} M_{\odot}$ and SFRs of $4 - 100 M_{\odot} \text{ yr}^{-1}$. In Bauermeister et al. [2013] some galaxies are 3σ upper limits on the velocity integrated flux.

3.4.5 ULIRGS AND LIRGS

Gao & Solomon [2004a,b] contains 53 infrared galaxies; 7 ULIRGs, approximately 20 LIRGs, and more than a dozen normal main-sequence spiral galaxies, which all have bright detected CO emission. All galaxies are listed with FWHM (and error estimates), integrated line fluxes, and coordinates in degrees. In addition, Graciá-Carpio et al. [2008, 2006] have collected CO redshift and luminosities for 17 local LIRGs and ULIRGs. The data sample from García-Burillo et al. [2012] also contains CO measurements of selected LIRGs and ULIRGs. Juneau et al. [2009] have follow-up HCN(3 - 2) observations with the 10 m Heinrich Hertz Submillimeter Telescope of 22 galaxies in the Gao & Solomon [2004a,b] data sample.

Combes et al. [2013] use their data set from 2011, containing 30 galaxies with redshifts $z \sim 0.2 - 0.6$ and detected CO emission using the IRAM 30 m telescope [Combes et al., 2011]. All sources are selected to be classified as ULIRGs. In addition, in Combes et al. [2013] they add a total of 39 galaxies at $z \sim 0.6 - 1.0$, where they detect CO emission by using the IRAM 30 m telescope. They list their full CO detected data set with coordinates, optical redshifts, frequencies, flux densities (Jy km s^{-1} and error, fluxes (from NED), central velocities, FWHM,

line luminosities, FIR luminosities, and stellar mass. They select ULIRGs with $L_{\text{FIR}} > 10^{12.45}$ between $0.6 < z < 1$, which have spectroscopic redshifts, and are detected at $60 \mu\text{m}$ with IRAS or at $70 \mu\text{m}$ with *Spitzer*.

Evans et al. [2006] collects a data sample consisting of 9 CO(1–0) detected host galaxies of infra-red excess Palomar-Green (PG) QSOs. They measure CO(1–0) emission lines and either HCN(1–0) or HCN(2–1).

García-Burillo et al. [2012] obtained HCN(1–0) observations of 19 LIRGs, where the majority are extracted from the sample studied by Alonso-Herrero et al. [2006] originally drawn from the IRAS Revised Bright Galaxy Sample (RBGS). All galaxies have $L_{\text{IR}} > 10^{11.05} L_{\odot}$. The estimated sizes are $< 10''$, which is equivalent to $1.7 - 3.6$ kpc meaning the total emission is contained within the telescope beam of $\sim 28''$ [García-Burillo et al., 2012]. In addition, they also include galaxies from Gao & Solomon [2004a,b], QSOs from Evans et al. [2006], and high- z galaxies from Gao et al. [2007].

González-Alfonso et al. [2015] collects 29 local galaxies with $z < 0.1$ included in the *Herschel* SHINING program and three OT programs. All CO measurements are unpublished data from previous studies including García-Burillo et al. [2012], Weiß et al. [2005] (M82), Houghton et al. [1997] (NGC 253), Scoville et al. [1983] (NGC 1068), Papadopoulos et al. [2012], Solomon et al. [1997], Casoli et al. [1999] (Arp 299), Mirabel et al. [1990], Chung et al. [2009], and Henkel et al. [1994] (NGC 4945). The sample is biased toward ULIRGs, where the most luminous sources are from IRAS RBGS. In addition, it also contains Seyfert and H_{II} galaxies. Some galaxies are corrected for extended emission.

Graciá-Carpio et al. [2008, 2006] observe HCN(1–0), HCN(3–2), HCO⁺(1–0), HCO⁺(3–2) in 17 LIRGs and ULIRGs in the infrared luminosity range $10^{11.3} L_{\odot} < L_{\text{IR}} < 10^{12.5} L_{\odot}$. All galaxies have distances larger than 50 kpc in order to measure the total emission of the molecular gas.

3.4.6 SMGs

Bothwell et al. [2013] have selected 40 galaxies with redshifts $z \sim 1 - 4$ drawn from the optical spectroscopic survey of SMGs by C05, the SCUBA Cluster Lens Survey [Smail et al., 2002], and the SCUBA Half Degree Extragalactic Survey (SHADES) of the Subaru/*XMM-Newton* Deep Field [Coppin et al., 2006]. In addition, they also included spectroscopically identified galaxies from the MAMBO imaging survey described in Bertoldi et al. [2002] and Greve et al. [2004]. All galaxies have been detected by either measuring the Lyman α emission, the H α emission and/or PAH emission from mid-IR spectroscopy with *Spitzer*.

Sharon et al. [2016] have selected 14 $z \sim 2 - 3$ SMGs and AGN host galaxies with existing CO(3 – 2) measurements. The data set consists of 11 AGN hosts, where 6 of these are lensed galaxies, and 3 SMGs, where one is unlensed. All galaxies are considered U/LIRGs and hyper-luminous infrared galaxies (HyLIRGs) with $10^{11.2} L_{\odot} \leq L_{\text{FIR}} \leq 10^{13.3} L_{\odot}$.

3.5 *Herschel*-DETECTED DATA SAMPLE

The galaxies selected for the SED fitted procedure using the DL07 dust models were all detected by the *Herschel Space Telescope*. The sample contains 122 galaxies at both high and low redshift (69 at $z < 0.1$ and 53 at redshift above). A few examples are presented in with the estimated parameters listed in Table 3.1. Figure 3.4 shows SEDs of two dusty low- z galaxy, where flux density is shown as a function of wavelength (Arp 220 on Figure 3.4(a) and IC 0883 on 3.4(b)). The black diamonds represent the flux densities obtained from the database as described in Section 3.2. The best fit is determined by the procedure explained in Section 2.2.2 is shown as the green, solid line. The estimated IR luminosity and dust mass were found to be $L_{\text{IR}} = 10^{12.00} L_{\odot}$, and $M_{\text{dust}} = 10^{8.78} M_{\odot}$, respectively. Another local galaxy is shown on Figure 3.4(b), where the estimated values were $L_{\text{IR}} = 10^{11.58} L_{\odot}$ and $M_{\text{dust}} = 10^{8.25} M_{\odot}$.

Galaxy	z	χ^2_{ν}	$\log L_{\text{IR}}$ [L_{\odot}]	$\log M_{\text{dust}}$ [M_{\odot}]	U_{min}	$\langle U \rangle$	γ %
ARP 220	0.02	3.67	12.02	8.78	12.00	13.12	0.00
IC 0883	0.02	4.89	11.58	8.25	15.00	16.52	0.00
SDSS J095900.61+022833.0	0.48	4.42	11.43	8.13	15.00	15.76	0.00
SDSS J141914.95+524929.5	1.20	7.18	12.71	9.43	12.00	15.72	0.03
.
.
.

Table 3.1: SED fitted parameters for selected *Herschel*-selected galaxies in the catalog. Columns are (from left) galaxy reference name, redshift, reduced χ^2 value, logarithmic infrared luminosity, logarithmic dust mass, intensity field, dust weighted mean starlight intensity, and the fraction of dust enclosed in PDR regions. All galaxies in the sample are listed in Appendix B.2.

Similarly, the SEDs of two galaxies in the high- z regime are represented in Figure 3.5. The solid, purple line shows the combined SED model, with $L_{\text{IR}} = 10^{11.43} L_{\odot}$ and $M_{\text{dust}} = 10^{8.13} M_{\odot}$ for SDSS J095900.61+022833.0 (Figure 3.5(a)), and $L_{\text{IR}} = 10^{12.71} L_{\odot}$ and $M_{\text{dust}} = 10^{9.43} M_{\odot}$ for SDSS J141914.95+524929.5 (Figure 3.5(b)). All results and parameters determined for these two galaxies are shown in Table 3.1. All the SED fits are presented in Appendix C.1, whereas the parameters are listed in Appendix B.2.

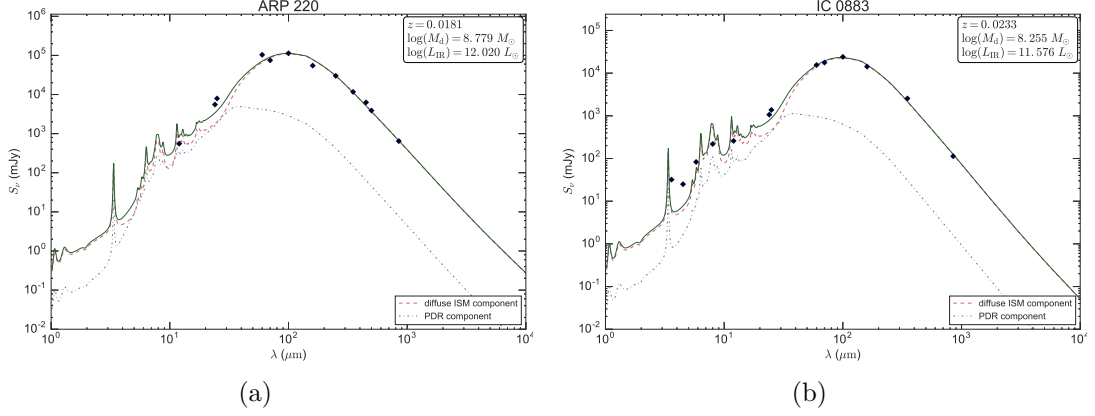


Figure 3.4: Spectral energy distribution (SED) of two low- z CO detected galaxies from the database. The solid dark green line represents the optimal fit using Draine & Li [2007] dust models described in Section 2.2.2. The model is a linear combination of two components; one describing the diffuse ISM (red dashed line) and the other describing dust in PDR regions (blue dotted line). Fitted parameters are listed in Table 3.1. (a): Arp 220 at $z = 0.0181$. (b): IC 0883 at $z = 0.0233$.

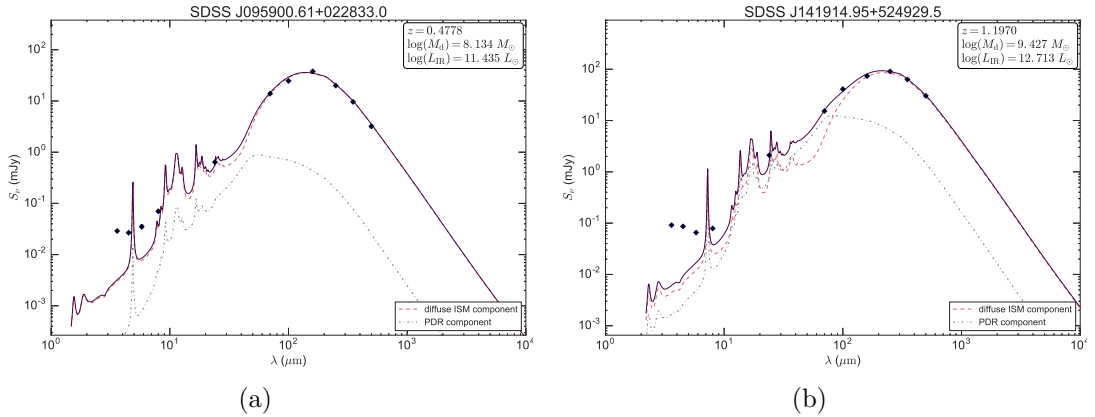


Figure 3.5: Spectral energy distribution (SED) of two high- z CO detected galaxies from the database. The solid dark green line represents the optimal fit using Draine & Li [2007] dust models described in Section 2.2.2. The model is a linear combination of two components; one describing the diffuse ISM (red dashed line) and the other describing dust in PDR regions (blue dotted line). Fitted parameters are listed in Table 3.1. (a): SDSS J095900.61+022833.0 at $z = 0.4778$. (b): SDSS J141914.95+524929.5 at $z = 1.1970$.

4 RESULTS AND DISCUSSION

As mentioned in Section 2.1.1, a galaxy’s molecular gas mass can be estimated from measurements of the CO line luminosity by using the α_{CO} conversion factor. However, the exact value of α_{CO} is very uncertain, as previous studies have shown it can vary up to a factor of ~ 5 . Since $M_{\text{gas}} = \alpha_{\text{CO}} \times L'_{\text{CO}}$, variations in α_{CO} can greatly impact the derived gas mass. Therefore, in order to examine the KS law without making assumptions on α_{CO} , only the direct observables are considered throughout the analysis.

4.1 ALL CO DETECTED GALAXIES

Figure 4.1 presents the observed quantities used to derive the physical parameters in the KS Law, with $L_{\text{IR}} \sim \text{SFR}$ and $L'_{\text{CO}} \sim M_{\text{gas}}$. 801 galaxies are included in the data sample with CO luminosities spanning a range of $1.5 \times 10^7 < L'_{\text{CO}} [\text{K km s}^{-1} \text{ pc}^2] < 4.3 \times 10^{12}$ and infrared luminosities $7.6 \times 10^7 < L_{\text{IR}} [L_{\odot}] < 4.6 \times 10^{13}$. The color map on the vertical axis shows the redshift distribution. Galaxies with upper limit CO measurements are marked as arrows. A prominent trend between the two parameters is observed at all redshifts. The large scatter in the $L_{\text{IR}} - L'_{\text{CO}}$ relation could be caused by galaxies where the CO luminosity arises from higher CO rotational states, and the different techniques used to estimate L'_{CO} from the literature. Similarly, the infrared luminosity have been obtained through a variety of different methods and/or SFR indicators, which might influence where the star-forming galaxies are located in the $L_{\text{IR}} - L'_{\text{CO}}$ relation. Each measurement from the literature has been corrected to be as consistent as possible including excitation corrections and IMF adjustments; CO line emissions above $J = 1 - 0$, independent of galaxy types, have been converted using the same excitation correction from Bothwell et al. [2013]. Stellar mass measurements were corrected for IMF variations.

In order to determine whether the scatter can be affected by the different determinations of L_{IR} in the literature, I selected *Herschel*-detected CO galaxies from the catalog with sufficient photometric coverage in the rest-frame FIR region of the SED. The L_{IR} values for the subsample have been obtained in a consistent way using the DL07 dust models described in Section 2.2.2. The $L_{\text{IR}} - L'_{\text{CO}}$ relation for the *Herschel*-detected sample is shown in Figure 4.2, where the color bar illustrates

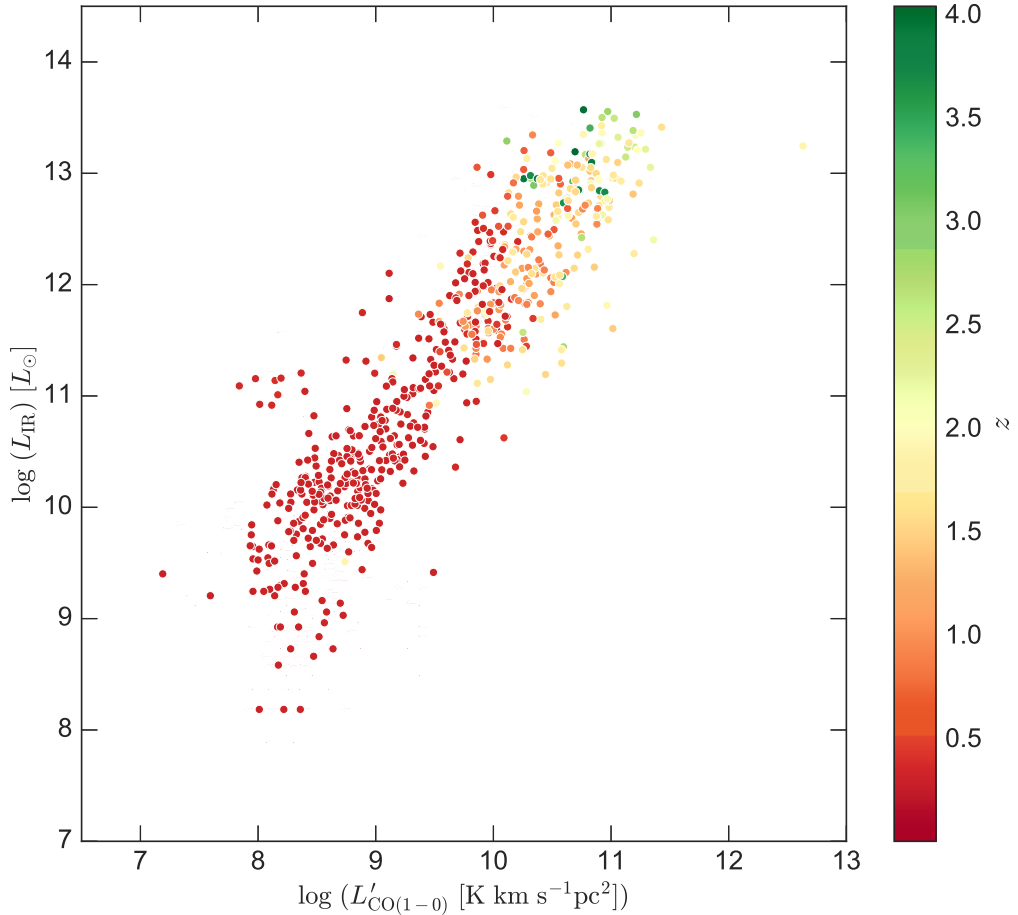


Figure 4.1: Correlation between L_{IR} and $L'_{\text{CO}(1-0)}$ for the full data sample consisting of 801 galaxies. The color bar on the right side show the redshift distribution of the sample, and upper limit CO measurements are marked as arrows.

the redshift distribution. A total of 122 galaxies are included at both high and low redshift, and a clear correlation between the two observables is visible. The *Herschel*-selected sample shows no systematic difference from the sources gathered in the literature, suggesting that the different methods used to estimate infrared luminosity are not significantly affecting the final results.

In Figure 4.3, I investigate how these direct observables match the expected trends for main-sequence and starburst galaxies, by comparing the data to the best-fit regression lines from Sargent et al. [2014], which are based on both high and low- z galaxies. Sargent et al. [2014] find that main sequence galaxies in the $\text{SFR}-M_*$ relation follow the relationship:

$$\log \left(\frac{L'_{\text{CO}(J=1 \rightarrow 0)}}{\text{K km s}^{-1} \text{ pc}^2} \right) = 0.54 + 0.81 \times \log \left(\frac{L_{\text{IR}}}{L_{\odot}} \right) \quad (4.1)$$

with a dispersion of 0.21 dex (red line). The blue line represents the offset from the MS with an intercept of 0.08. Galaxies with higher CO transitions in the Sar-

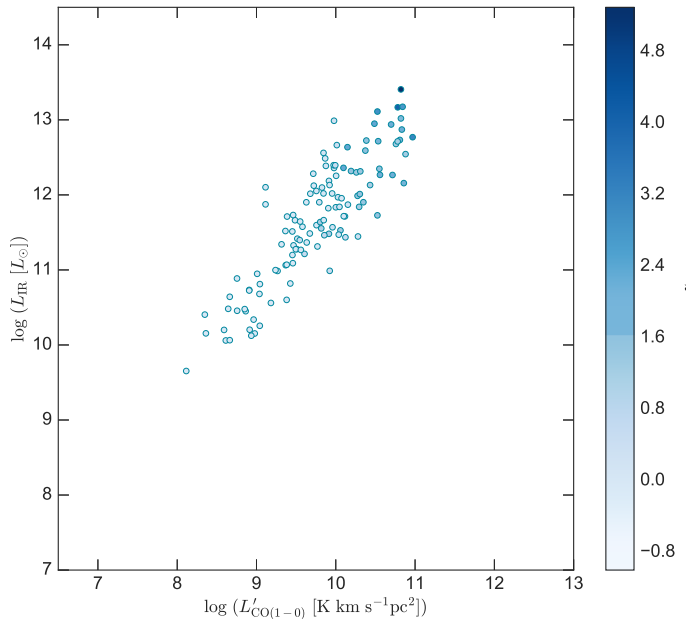


Figure 4.2: Correlation between L_{IR} and $L'_{\text{CO}(1-0)}$ for the *Herschel*-detected data sample consisting of 122 galaxies. The color bar on the right side shows the redshift distribution of the sample.

gent et al. [2014] sample were converted to CO(1-0) using excitation corrections in Dannerbauer et al. [2009] and Leroy et al. [2009]. As seen in Figure 4.3, the majority of star-forming galaxies in our sample follow the disk sequence, whereas local ULIRGs and high- z SMGs systematically lie above. For a fixed $L'_{\text{CO}(1-0)}$, galaxies with larger L_{IR} have higher SFRs. Since the star formation efficiency depends on the current SFR and the available amount of gas as $\text{SFE} \sim L_{\text{IR}}/L'_{\text{CO}(1-0)}$, it suggests that galaxies above the Sargent et al. [2014] disk sequence are systems undergoing more efficient star formation. This phase is thought to be short-lived due to the high SFE resulting in a rapid depletion of the gas supply, which serves as the fuel for star formation. Galaxies well above the disk sequence therefore have short gas depletion timescales, and are not expected to continue their current rate of star formation for a long period of time.

While the two sequences from Sargent et al. [2014] overlap with our data, a simple fit to the full sample would suggest a single linear relationship with a steeper slope would fit the data better. However, this full sample contains a mix of both main-sequence and starburst galaxies. In the following section, the galaxies will be classified by their off-set to the main-sequence in order to determine if separate trends really do exist for these populations.

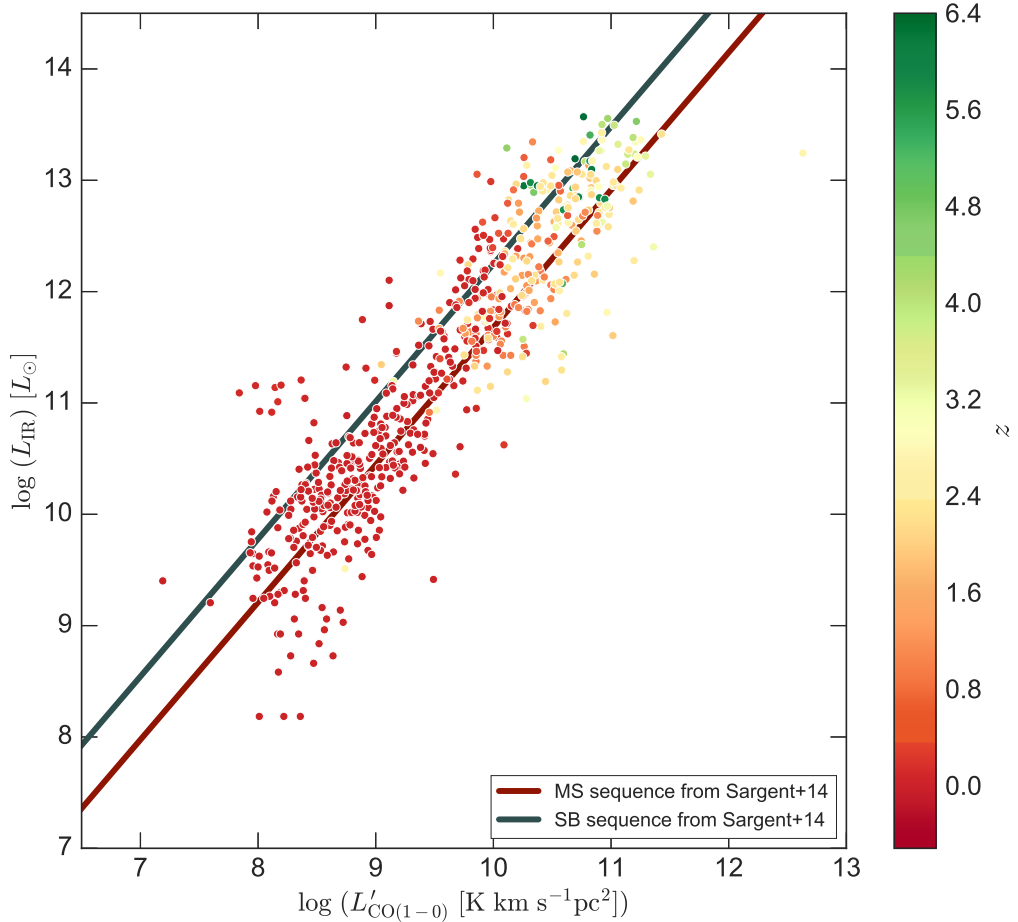


Figure 4.3: Correlation between L_{IR} and $L'_{\text{CO}(1-0)}$ for the full data sample consisting of 641 galaxies, where upper limits have been excluded. The color bar on the right side shows the redshift distribution of the sample. The red and blue lines represent the MS and SB sequences from Sargent et al. [2014], respectively.

4.2 DISTANCE TO THE MAIN-SEQUENCE

The existence of a relatively tight main-sequence of star formation in the $\text{SFR}-M_*$ plane suggests that the bulk of the galaxy population forms stars gradually, with long duty cycles. The off-set from the main-sequence (ΔSFR) can be obtained by comparing a given galaxy's SFR to the SFR_{MS} , which is the average SFR of a galaxy located on the main-sequence with the same redshift and stellar mass. Galaxies within $1/3 < \text{SFR}/\text{SFR}_{\text{MS}} < 3$ are generally deemed main-sequence galaxies, while galaxies above or below this range are assumed starbursts or quiescents, respectively (Section 2.3).

Since the full catalog contains galaxies below, on, and above the main-sequence, it is necessary to distinguish between the different galaxy populations. Each galaxy's position with respect to the main-sequence was derived according to its SFR, redshift, and stellar mass if sufficient published measurements were available. The $L'_{\text{CO}(1-0)}$ and L_{IR} correlation for the classified galaxies is plotted in Figure 4.4. A total of 322 galaxies spanning a wide range of redshift were included. The col-

ors indicate the various galaxy types: grey, red and blue data points represent quiescent, main-sequence, and starburst galaxies, respectively.

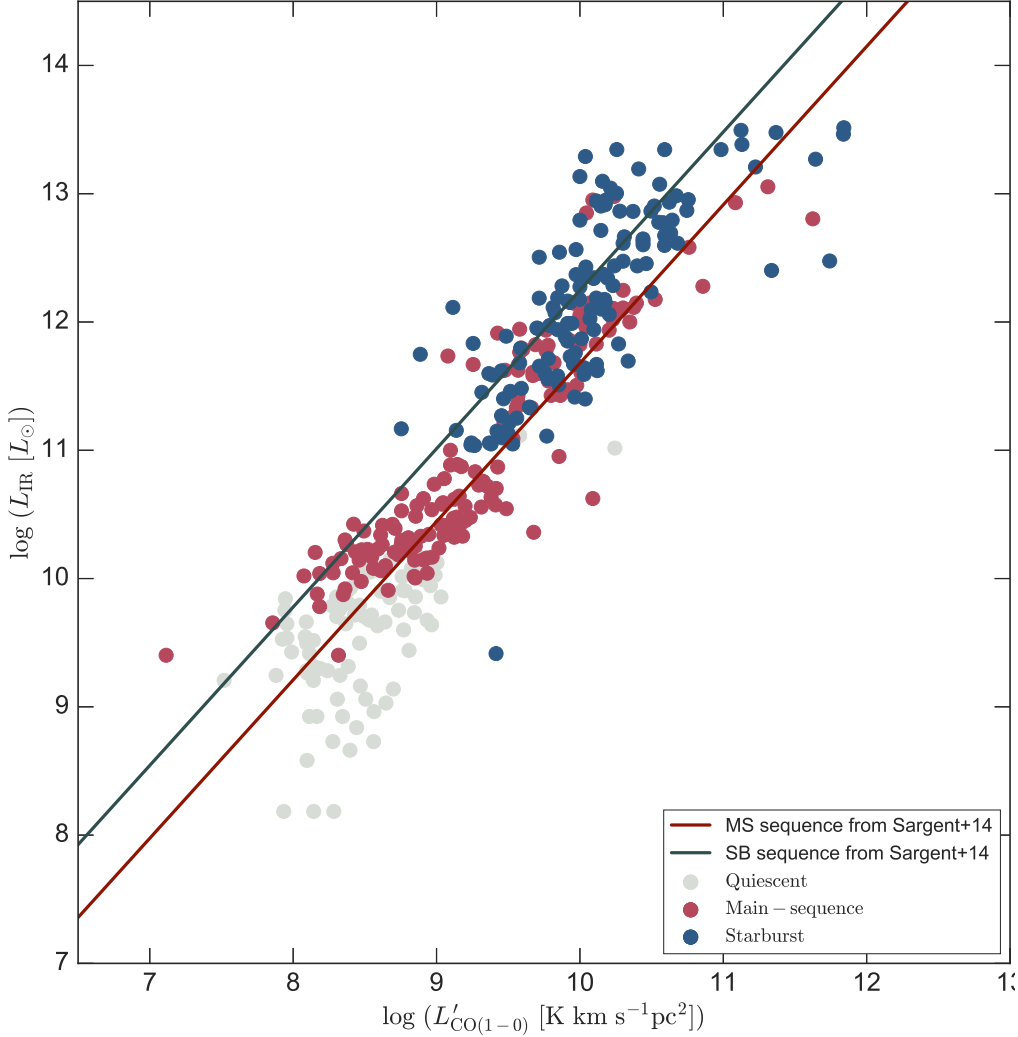


Figure 4.4: L_{IR} vs. $L'_{\text{CO}(1-0)}$ for the data sample including 322 galaxies, where upper limits have been excluded. The colors indicate the offset from the main sequence $\Delta\text{SFR} \equiv \text{SFR}/\text{SFR}_{\text{MS}}$ as described in Schreiber et al. [2015]. The quiescent, main sequence, and starburst galaxies are classified as having $\Delta\text{SFR} < 1/3$, $1/3 \leq \Delta\text{SFR} \leq 3$ and $\Delta\text{SFR} > 3$, respectively.

The result indicates that the majority of main-sequence galaxies in the catalog follow the Sargent et al. [2014] disk trend, while starburst galaxies systematically lie above this sequence. However, at $9 < \log L'_{\text{CO}(1-0)} < 11$, the distinction between these two galaxy populations is less clear, as a fraction of the starburst galaxies lie on the disk sequence. In order to test if the trend is redshift dependent, I divided the galaxies into two redshift regimes: one containing local galaxies with $z < 0.1$ and another sample at $1 < z < 3$. Since only galaxies with accurately measured stellar mass measurements were included, a broader redshift range was selected in

the high- z regime, in order to obtain a decent sample.

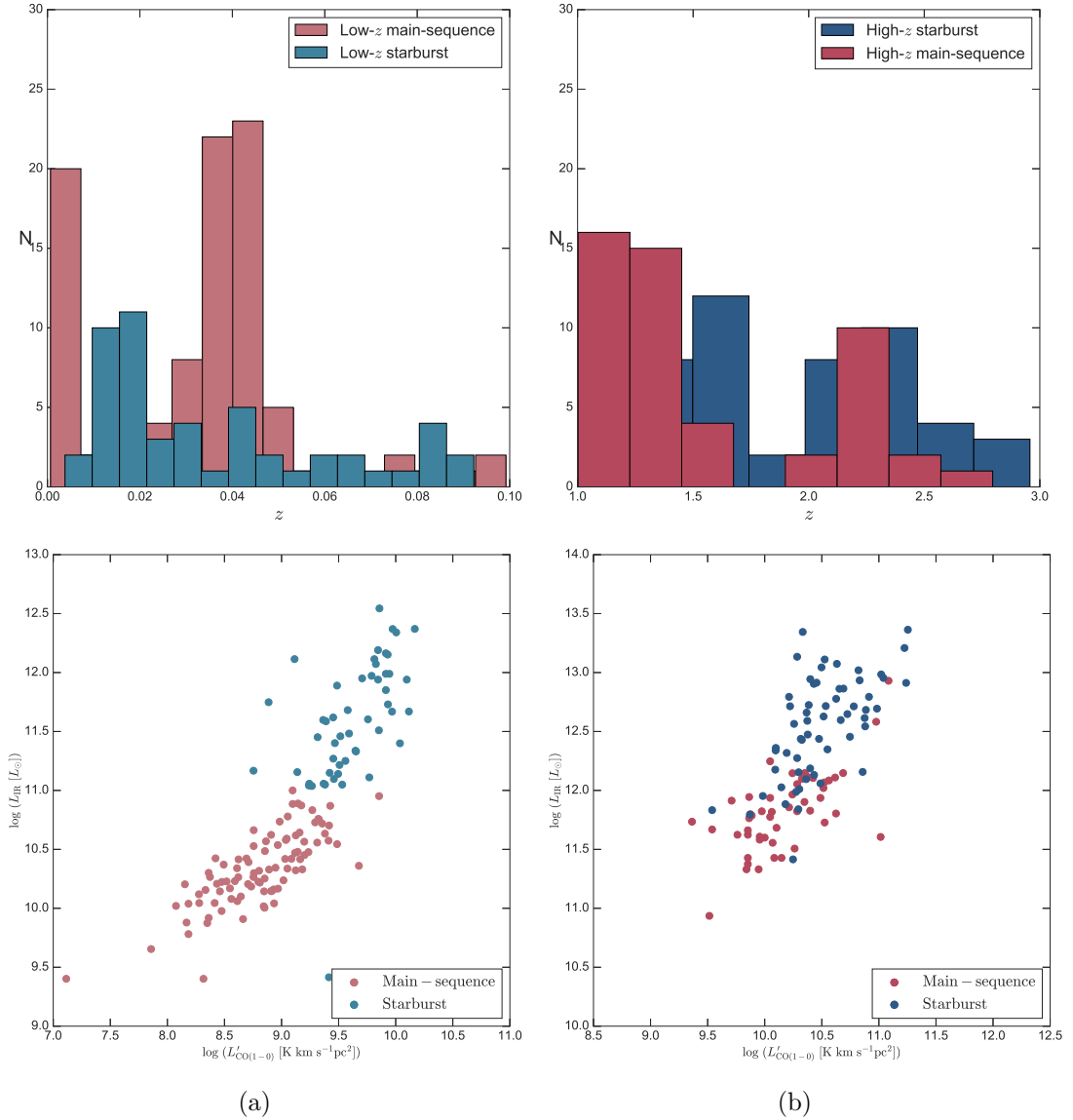


Figure 4.5: $L_{\text{IR}} - L'_{\text{CO}}$ relation for the data sample with stellar mass values. Main-sequence and starburst galaxies are included. Galaxies at $z < 0.1$ are shown in (a), whereas those at larger redshift are presented in (b).

Figure 4.5(a) represents the $L_{\text{IR}} - L'_{\text{CO}}$ correlation for local MS galaxies and starbursts, where a clear distinction between the two populations is visible. The main-sequence galaxies are all located below the starbursts, which appear to follow a steeper slope than main-sequence galaxies. At larger redshift (Figure 4.5(b)), the tendency is less clear as the two populations blend together at an infrared luminosity of $L_{\text{IR}} \sim 10^{12} L_{\odot}$. Nonetheless, they are located in the same regions as the galaxies in the low- z sample with no noticeable deviations present. From the results both at high and low- z , it is clear that two different populations are

present. Above each figure, the redshift distribution of the given sample is shown.

4.3 TWO MODES OF STAR FORMATION

As shown in Figure 4.3 the majority of star-forming galaxies in the catalog follow the Sargent et al. [2014] disk sequence, while a minor population lies above. However, the full catalog can also be described by one sequence with a steeper slope. To examine if these galaxies are located within the expected regimes in the $L_{\text{IR}} - L'_{\text{CO}}$ correlation, they were classified as either main-sequence or starburst galaxies. The result is presented in Figure 4.4, where the two galaxy populations follow two distinct sequences. This trend remains after separating the sample in redshift bins. These results suggest that main-sequence and starburst galaxies undergo different modes of star formation. Since only the observed quantities have been considered, the final result is not affected by the assumption of a bimodal α_{CO} conversion factor.

4.4 LINKING SFE WITH THE OFF-SET FROM THE MS

Previous studies claim a galaxy's SFE is directly related to its distance from the main-sequence. The star formation efficiency $SFE \sim L_{\text{IR}}/L'_{\text{CO}}$ is here defined as the ratio between the current SFR and the amount of available molecular gas. In starburst systems the SFE is significantly enhanced, with the star formation activity possibly triggered by a major merger event.

In Figure 4.6, we directly compare the SFE and distance to the main sequence for all galaxies with stellar mass measurements. A total of 376 galaxies were included, and the color bar represents the redshift distribution of the sample, which covers a broad range of redshift.

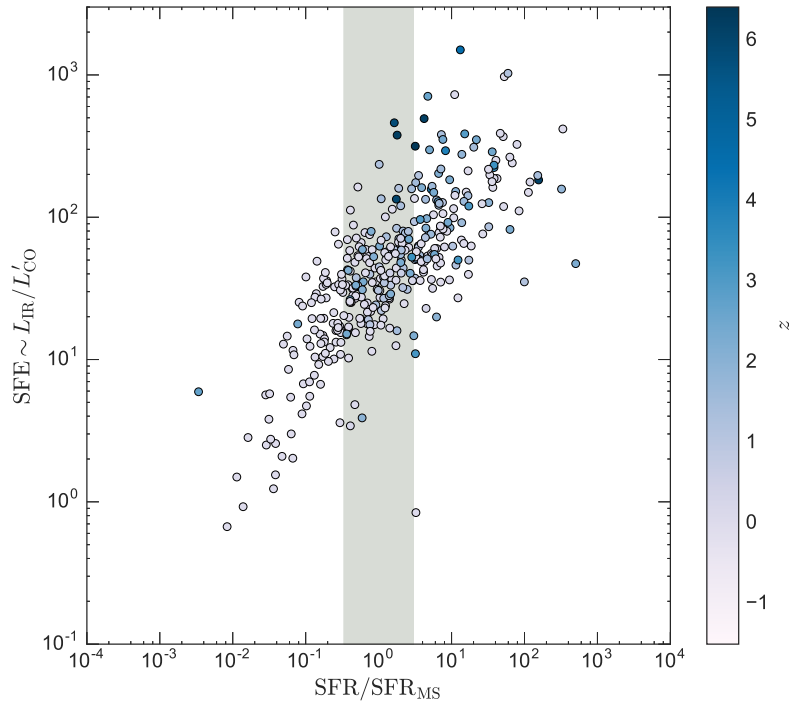


Figure 4.6: Correlation between SFR/SFR_{MS} and $SFE = L_{\text{IR}}/L'_{\text{CO}}$ for the full data sample with published M_* values, where upper limits have been excluded (consisting of 376 galaxies). The color scheme represents the redshift distribution.

In order to distinguish between local and distant galaxies, the sample have been divided using the same redshift cut as in the previous section. Figure 4.7(a) represents galaxies below $z < 0.1$ whereas Figure 4.7(b) includes galaxies within the range $1 < z < 3$. For the entire sample, there is a relatively tight correlation between SFE and distance to the main-sequence. However, the SFE of the main-sequence galaxies ($0.3 < SFR/SFR_{\text{MS}} < 3$) in the local sample have a large scatter (Figure 4.7(a)), which could be explained by variations in their gas fractions [Magdis et al., 2012]. The correlation is less prominent at larger redshift, but this may be due to selection effects, as only a few galaxies have $L_{\text{IR}}/L_{\text{CO}} < 10$ and $SFR/SFR_{\text{MS}} < 0.6$. Together, these results indicate that the star formation

efficiency in galaxies is responsible for the distance to the main-sequence.

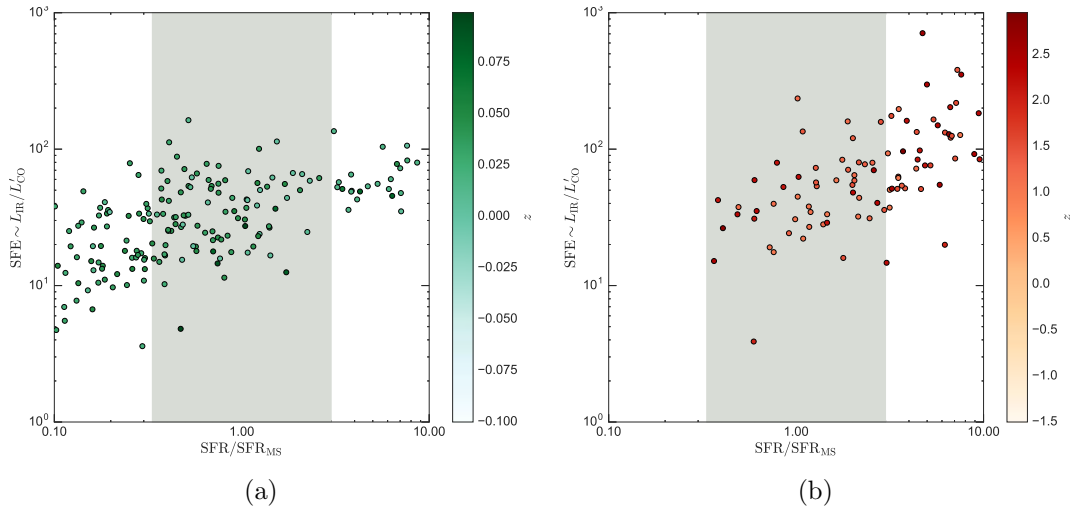


Figure 4.7: Correlation between SFE and SFR/SFR_{MS} . Galaxies at $z < 0.1$ are shown in (a), whereas those in the redshift range $1 < z < 3$ are shown in (b).

4.5 DUST TEMPERATURE AND DENSE GAS FRACTIONS

As discussed in Section 2.1, CO is primarily a tracer of more diffuse molecular gas, while other lines such as HCN trace the denser molecular gas where star formation takes place [Gao & Solomon, 2004a]. Figure 4.8 displays the correlation between the fraction of dense to diffuse gas ($L'_{\text{HCN}(1-0)}/L'_{\text{CO}(1-0)}$) and $L_{\text{IR}}/M_{\text{dust}}$ for galaxies with observations of both $L'_{\text{HCN}(1-0)}$ and $L'_{\text{CO}(1-0)}$. A total of 64 galaxies are included. Since the ratio of infrared luminosity to dust mass is directly proportional to the mean radiation field (Section 2.2.2), a higher $L_{\text{IR}}/M_{\text{dust}}$ indicates warmer dust temperatures. From the results it is shown that galaxies with higher fraction of dense molecular gas are observed to have warmer dust temperatures. This may reflect the expectation that galaxies with a higher dense molecular gas fraction will have more ongoing star formation that can heat the surrounding dust to warmer temperatures.

Figure 4.9 presents the relationship between SFE and $L_{\text{IR}}/M_{\text{dust}}$ for the 122 galaxies with the required observations at both high and low redshift. An increase in $L_{\text{IR}}/M_{\text{dust}}$ for higher SFE is observed, suggesting that galaxies that are very efficient in turning their gas into stars tend to have higher gas temperatures (since the $L_{\text{IR}}/M_{\text{dust}}$ is directly related to the mean intensity of the radiation field).

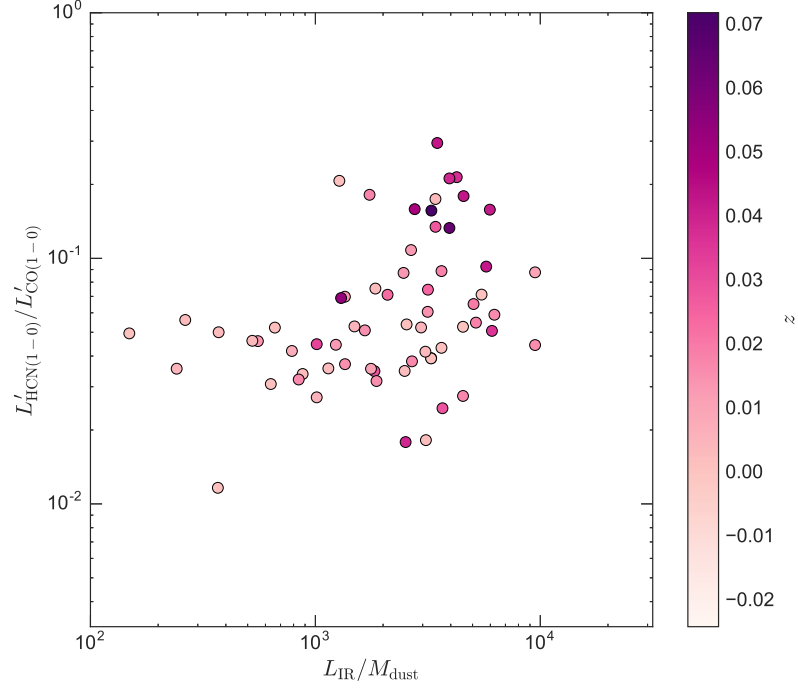


Figure 4.8: Correlation between $L_{\text{IR}}/M_{\text{dust}}$ and $L'_{\text{HCN}(1-0)}/L'_{\text{CO}(1-0)}$ for the *Herschel*-detected data sample consisting of 64 galaxies. The color bar on the right side shows the redshift distribution of the data set.

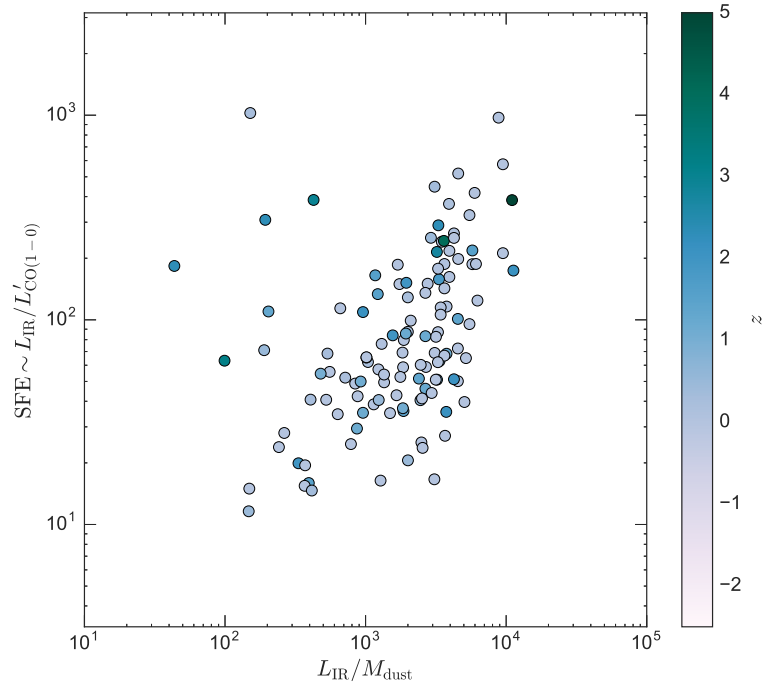


Figure 4.9: Correlation between $L_{\text{IR}}/M_{\text{dust}}$ and $\text{SFE} = L_{\text{IR}}/L'_{\text{CO}(1-0)}$ for the *Herschel*-detected data sample consisting of 64 galaxies. The color bar on the right side shows the redshift distribution of the data set.

4.5.1 FUTURE PERSPECTIVE

The final data sample have been corrected in a coherent way, where each CO excitation measurement has been converted using the same CO SLED. However, it has been suggested that the CO excitation conversions are different for MS and SB galaxies, and that they can vary by up to a factor of ~ 5 [Bolatto et al., 2013]. It would be interesting to investigate how different CO excitation conversions can affect the observed trends.

As previously mentioned, the final sample is a compilation of various studies where the line measurements, infrared luminosities, and stellar masses have been estimated using different methods and models. Since these variations might influence the results significantly, it would be optimal to avoid this issue by determining all parameters in a consistent way.

In addition, more observations of CO detected SFGs with ALMA or IRAM at various distances from the main-sequence will result in a statistically representative sample. This is needed in order to explore the different modes of star formation.

Furthermore, the dust and gas content in galaxies are linked together through metallicity [Berta et al., 2016]. The dust masses estimated using the Draine & Li [2007] dust models can be used to determine the total gas mass as $M_{\text{gas}} = M_{\text{dust}} \times \delta_{\text{GDR}}$, where δ_{GDR} is the gas-to-dust ratio of the galaxy, which depends on the metallicity [Magdis et al., 2012]. Since $M_{\text{gas}} = \alpha_{\text{CO}} \times L'_{\text{CO}}$, the dust and metallicity estimates can be used to determine and constrain the α_{CO} conversion factor.

5 CONCLUSION

To examine the possible two modes of star formation for main-sequence galaxies and starbursts, I collected a large sample by combining all published CO detected galaxies from the literature. This was done by studying the SFR and gas reservoir traced by molecular CO lines in star forming galaxies. The final catalog contains 801 galaxies and is a compilation of several studies, where the individual measurements have been estimated using various methods and techniques. I corrected each measurement to obtain a consistent sample as possible. Only the direct observables have been considered (L_{IR} and L'_{CO}), in order to obtain direct evidence for SFE variations in both main-sequence galaxies and starburst galaxies at various redshifts.

A significant scatter was observed in the $L_{\text{CO}} - L_{\text{IR}}$ relation. In order to examine if it was caused by the various L_{IR} estimates from previous studies, I determined infrared luminosities for a subsample of galaxies in the final catalog. I selected 122 *Herschel*-detected galaxies with sufficient photometric coverage, where L_{IR} values were estimated in a consistent way using DL07 dust models. The results showed no significant difference. The majority of star-forming galaxies in the full sample follow the disk sequence described in Sargent et al. [2014], whereas a fraction lie on the parallel starburst line above the sequence. In order to investigate the dispersion in the $L'_{\text{CO}} - L_{\text{IR}}$ relation, each galaxy was classified as either main-sequence or starburst galaxies. This was done by determining the off-set from the MS ($\Delta\text{SFR} = \text{SFR}/\text{SFR}_{\text{MS}}$). A total of 322 SFGs with sufficient measurements were included. The majority of main-sequence galaxies from the SFR- M_* relation follow a unique sequence in the $L_{\text{CO}} - L_{\text{IR}}$ relation, whereas starburst galaxies systematically lie above. This trend remains after the sample was divided in redshift bins. The results support the existence of two distinct modes of star formation.

Furthermore, an increase in star formation efficiency was observed with increasing offset from the main-sequence. These results indicate that the SFE in galaxies drives the offset from the main-sequence. Star forming galaxies with enhanced SFE showed revealed higher dust temperatures, indicating ongoing star formation in galaxies heat the surrounding dust in the ISM.

With the current analysis, statistical analyses are necessary to observe any possible statistical significance to determine the possible modes of star formation in main-sequence and starburst galaxies. However, examining the observed properties clearly reveal general trends, where the results are not affected by α_{CO} .

REFERENCES

- Alonso-Herrero, A., Rieke, G. H., Rieke, M. J., Colina, L., Pérez-González, P. G., & Ryder, S. D. (2006, October). Near-Infrared and Star-forming Properties of Local Luminous Infrared Galaxies. *ApJ*, *650*, 835-849. doi: 10.1086/506958
- Armus, L., Mazzarella, J. M., Evans, A. S., Surace, J. A., Sanders, D. B., Iwasawa, K., ... Xu, K. (2009, June). GOALS: The Great Observatories All-Sky LIRG Survey. *PASP*, *121*, 559-576. doi: 10.1086/600092
- Bauermeister, A., Blitz, L., Bolatto, A., Bureau, M., Leroy, A., Ostriker, E., ... Wright, M. (2013, May). The EGN0G Survey: Molecular Gas in Intermediate-Redshift Star-Forming Galaxies. *ApJ*, *768*, 132. doi: 10.1088/0004-637X/768/2/132
- Berta, S., Lutz, D., Genzel, R., Förster-Schreiber, N. M., & Tacconi, L. J. (2016, March). Measures of galaxy dust and gas mass with Herschel photometry and prospects for ALMA. *A&A*, *587*, A73. doi: 10.1051/0004-6361/201527746
- Bertoldi, F., Menten, K. M., Kreysa, E., Carilli, C. L., & Owen, F. (2002). The dawn of galaxies: deep MAMBO imaging surveys. *Highlights of Astronomy*, *12*, 473-476.
- Bolatto, A. D., Wolfire, M., & Leroy, A. K. (2013, August). The CO-to-H₂ Conversion Factor. *ARA&A*, *51*, 207-268. doi: 10.1146/annurev-astro-082812-140944
- Bothwell, M., Smail, I., Chapman, S., Genzel, R., Ivison, R., Tacconi, L., ... others (2013). A survey of molecular gas in luminous sub-millimetre galaxies. *Monthly Notices of the Royal Astronomical Society*, *429*(4), 3047–3067.
- Bothwell, M. S., Wagg, J., Cicone, C., Maiolino, R., Møller, P., Aravena, M., ... Walter, F. (2014, December). ALLSMOG: an APEX Low-redshift Legacy Survey for MOlecular Gas - I. Molecular gas scaling relations, and the effect of the CO/H₂ conversion factor. *MNRAS*, *445*, 2599-2620. doi: 10.1093/mnras/stu1936
- Bouché, N., Dekel, A., Genzel, R., Genel, S., Cresci, G., Förster Schreiber, N. M., ... Tacconi, L. (2010, August). The Impact of Cold Gas Accretion Above a

- Mass Floor on Galaxy Scaling Relations. *ApJ*, *718*, 1001-1018. doi: 10.1088/0004-637X/718/2/1001
- Brinchmann, J., Charlot, S., White, S. D. M., Tremonti, C., Kauffmann, G., Heckman, T., & Brinkmann, J. (2004, July). The physical properties of star-forming galaxies in the low-redshift Universe. *MNRAS*, *351*, 1151-1179. doi: 10.1111/j.1365-2966.2004.07881.x
- Bussmann, R. S., Narayanan, D., Shirley, Y. L., Juneau, S., Wu, J., Solomon, P. M., ... Walker, C. K. (2008, July). The Star Formation Rate-Dense Gas Relation in Galaxies as Measured by HCN(3-2) Emission. *ApJ*, *681*, L73. doi: 10.1086/590181
- Carilli, C., & Walter, F. (2013). Cool gas in high redshift galaxies. *arXiv preprint arXiv:1301.0371*.
- Casey, C. M., Narayanan, D., & Cooray, A. (2014). Dusty star-forming galaxies at high redshift. *Physics Reports*, *541*(2), 45-161.
- Casoli, F., Willaime, M.-C., Viallefond, F., & Gerin, M. (1999, June). Molecular gas in the system of merging galaxies ARP 299. *A&A*, *346*, 663-674.
- Chabrier, G. (2003, July). Galactic Stellar and Substellar Initial Mass Function. *PASP*, *115*, 763-795. doi: 10.1086/376392
- Chung, A., Narayanan, G., Yun, M. S., Heyer, M., & Erickson, N. R. (2009, September). The Redshift Search Receiver Observations of ^{12}CO $J = 1 \rightarrow 0$ in 29 Ultraluminous Infrared Galaxies. *AJ*, *138*, 858-872. doi: 10.1088/0004-6256/138/3/858
- Combes, F., García-Burillo, S., Braine, J., Schinnerer, E., Walter, F., & Colina, L. (2011, April). Galaxy evolution and star formation efficiency at $0.2 < z < 0.6$. *A&A*, *528*, A124. doi: 10.1051/0004-6361/201015739
- Combes, F., García-Burillo, S., Braine, J., Schinnerer, E., Walter, F., & Colina, L. (2013, February). Gas fraction and star formation efficiency at $z < 1.0$. *A&A*, *550*, A41. doi: 10.1051/0004-6361/201220392
- Coppin, K., Chapin, E. L., Mortier, A. M. J., Scott, S. E., Borys, C., Dunlop, J. S., ... Willott, C. J. (2006, November). The SCUBA Half-Degree Extragalactic Survey - II. Submillimetre maps, catalogue and number counts. *MNRAS*, *372*, 1621-1652. doi: 10.1111/j.1365-2966.2006.10961.x
- Daddi, E., Bournaud, F., Walter, F., Dannerbauer, H., Carilli, C. L., Dickinson, M., ... Stern, D. (2010, April). Very High Gas Fractions and Extended Gas Reservoirs in $z = 1.5$ Disk Galaxies. *ApJ*, *713*, 686-707. doi: 10.1088/0004-637X/713/1/686

- Daddi, E., Dickinson, M., Morrison, G., Chary, R., Cimatti, A., Elbaz, D., ... Mignoli, M. (2007, November). Multiwavelength Study of Massive Galaxies at $z \sim 2$. I. Star Formation and Galaxy Growth. *ApJ*, *670*, 156-172. doi: 10.1086/521818
- Dale, D. A., Aniano, G., Engelbracht, C. W., Hinz, J. L., Krause, O., Montiel, E. J., ... Zibetti, S. (2012, January). Herschel Far-infrared and Submillimeter Photometry for the KINGFISH Sample of nearby Galaxies. *ApJ*, *745*, 95. doi: 10.1088/0004-637X/745/1/95
- Dannerbauer, H., Daddi, E., Riechers, D. A., Walter, F., Carilli, C. L., Dickinson, M., ... Morrison, G. E. (2009, June). Low Milky-Way-Like Molecular Gas Excitation of Massive Disk Galaxies at $z \sim 1.5$. *ApJ*, *698*, L178-L182. doi: 10.1088/0004-637X/698/2/L178
- Downes, D., & Solomon, P. M. (1998, November). Rotating Nuclear Rings and Extreme Starbursts in Ultraluminous Galaxies. *ApJ*, *507*, 615-654. doi: 10.1086/306339
- Draine, B. T., Dale, D. A., Bendo, G., Gordon, K. D., Smith, J. D. T., Armus, L., ... Teplitz, H. I. (2007, July). Dust Masses, PAH Abundances, and Starlight Intensities in the SINGS Galaxy Sample. *ApJ*, *663*, 866-894. doi: 10.1086/518306
- Draine, B. T., & Li, A. (2007, March). Infrared Emission from Interstellar Dust. IV. The Silicate-Graphite-PAH Model in the Post-Spitzer Era. *ApJ*, *657*, 810-837. doi: 10.1086/511055
- Evans, A. S., Solomon, P. M., Tacconi, L. J., Vavilkin, T., & Downes, D. (2006, December). Dense Molecular Gas and the Role of Star Formation in the Host Galaxies of Quasi-stellar Objects. *AJ*, *132*, 2398-2408. doi: 10.1086/508416
- Gao, Y., Carilli, C. L., Solomon, P. M., & Vanden Bout, P. A. (2007, May). HCN Observations of Dense Star-forming Gas in High-Redshift Galaxies. *ApJ*, *660*, L93-L96. doi: 10.1086/518244
- Gao, Y., & Solomon, P. M. (2004a, May). HCN Survey of Normal Spiral, Infrared-luminous, and Ultraluminous Galaxies. *ApJS*, *152*, 63-80. doi: 10.1086/383003
- Gao, Y., & Solomon, P. M. (2004b, May). The Star Formation Rate and Dense Molecular Gas in Galaxies. *ApJ*, *606*, 271-290. doi: 10.1086/382999
- García-Burillo, S., Usero, A., Alonso-Herrero, A., Graciá-Carpio, J., Pereira-Santaella, M., Colina, L., ... Arribas, S. (2012, March). Star-formation laws in luminous infrared galaxies. New observational constraints on models. *A&A*, *539*, A8. doi: 10.1051/0004-6361/201117838

- Genzel, R., Tacconi, L. J., Combes, F., Bolatto, A., Neri, R., Sternberg, A., ... Weiner, B. (2012, February). The Metallicity Dependence of the CO \rightarrow H₂ Conversion Factor in $z \geq 1$ Star-forming Galaxies. *ApJ*, *746*, 69. doi: 10.1088/0004-637X/746/1/69
- Ginsburg, A., Robitaille, T., Parikh, M., Deil, C., Mirocha, J., Woillez, J., ... Shiga, D. (2013, 9). Astroquery v0.1. Retrieved from https://figshare.com/articles/Astroquery_v0_1/805208 doi: 10.6084/m9.figshare.805208.v2
- González-Alfonso, E., Fischer, J., Sturm, E., Graciá-Carpio, J., Veilleux, S., Meléndez, M., ... Genzel, R. (2015, February). High-lying OH Absorption, [C II] Deficits, and Extreme L_{FIR}/M_{H2} Ratios in Galaxies. *ApJ*, *800*, 69. doi: 10.1088/0004-637X/800/1/69
- Graciá-Carpio, J., García-Burillo, S., & Planesas, P. (2008, January). Dense molecular gas in a sample of LIRGs and ULIRGs: The low-redshift connection to the huge high-redshift starbursts and AGNs. *Ap&SS*, *313*, 331-335. doi: 10.1007/s10509-007-9629-y
- Graciá-Carpio, J., García-Burillo, S., Planesas, P., & Colina, L. (2006, April). Is HCN a True Tracer of Dense Molecular Gas in Luminous and Ultraluminous Infrared Galaxies? *ApJ*, *640*, L135-L138. doi: 10.1086/503361
- Greve, T. R., Ivison, R. J., Bertoldi, F., Stevens, J. A., Dunlop, J. S., Lutz, D., & Carilli, C. L. (2004, November). A 1200- μ m MAMBO survey of ELAISN2 and the Lockman Hole - I. Maps, sources and number counts. *MNRAS*, *354*, 779-797. doi: 10.1111/j.1365-2966.2004.08235.x
- Henkel, C., Whiteoak, J. B., & Mauersberger, R. (1994, April). Dense gas in nearby galaxies. VII: The active nucleus of NGC 4945. *A&A*, *284*, 17-27.
- Houghton, S., Whiteoak, J. B., Koribalski, B., Booth, R., Wiklind, T., & Wielebinski, R. (1997, September). The extended CO J=1-0 emission in NGC 253. *A&A*, *325*, 923-932.
- Huang, M.-L., & Kauffmann, G. (2014, September). The variation in molecular gas depletion time among nearby galaxies: what are the main parameter dependences? *MNRAS*, *443*, 1329-1338. doi: 10.1093/mnras/stu1232
- Juneau, S., Narayanan, D. T., Moustakas, J., Shirley, Y. L., Bussmann, R. S., Kennicutt, R. C., Jr., & Vanden Bout, P. A. (2009, December). Enhanced Dense Gas Fraction in Ultraluminous Infrared Galaxies. *ApJ*, *707*, 1217-1232. doi: 10.1088/0004-637X/707/2/1217
- Kennicutt, R. C., & Evans, N. J. (2012, September). Star Formation in the Milky Way and Nearby Galaxies. *ARA&A*, *50*, 531-608. doi: 10.1146/annurev-astro-081811-125610

- Kennicutt, R. C., Jr. (1989, September). The star formation law in galactic disks. *ApJ*, *344*, 685-703. doi: 10.1086/167834
- Kennicutt, R. C., Jr. (1998). Star Formation in Galaxies Along the Hubble Sequence. *ARA&A*, *36*, 189-232. doi: 10.1146/annurev.astro.36.1.189
- Kroupa, P. (2001, April). On the variation of the initial mass function. *MNRAS*, *322*, 231-246. doi: 10.1046/j.1365-8711.2001.04022.x
- Le Floch, E., Papovich, C., Dole, H., Bell, E. F., Lagache, G., Rieke, G. H., ... Mould, J. (2005, October). Infrared Luminosity Functions from the Chandra Deep Field-South: The Spitzer View on the History of Dusty Star Formation at $0 \lesssim z \lesssim 1$. *ApJ*, *632*, 169-190. doi: 10.1086/432789
- Leroy, A. K., Walter, F., Bigiel, F., Usero, A., Weiss, A., Brinks, E., ... Roussel, H. (2009, June). Heracles: The HERA CO Line Extragalactic Survey. *AJ*, *137*, 4670-4696. doi: 10.1088/0004-6256/137/6/4670
- Madau, P., & Dickinson, M. (2014). Cosmic star formation history. *arXiv preprint arXiv:1403.0007*.
- Magdis, G. E., Daddi, E., Béthermin, M., Sargent, M., Elbaz, D., Pannella, M., ... others (2012). The evolving interstellar medium of star-forming galaxies since $z=2$ as probed by their infrared spectral energy distributions. *The Astrophysical Journal*, *760*(1), 6.
- Magdis, G. E., Rigopoulou, D., Hopwood, R., Huang, J.-S., Farrah, D., Pearson, C., ... Vaccari, M. (2014, November). A Far-infrared Spectroscopic Survey of Intermediate Redshift (Ultra) Luminous Infrared Galaxies. *ApJ*, *796*, 63. doi: 10.1088/0004-637X/796/1/63
- Magnelli, B., Popesso, P., Berta, S., Pozzi, F., Elbaz, D., Lutz, D., ... Valtchanov, I. (2013, May). The deepest Herschel-PACS far-infrared survey: number counts and infrared luminosity functions from combined PEP/GOODS-H observations. *A&A*, *553*, A132. doi: 10.1051/0004-6361/201321371
- Melbourne, J., Soifer, B. T., Desai, V., Pope, A., Armus, L., Dey, A., ... Alberts, S. (2012, May). The Spectral Energy Distributions and Infrared Luminosities of $z \approx 2$ Dust-obscured Galaxies from Herschel and Spitzer. *AJ*, *143*, 125. doi: 10.1088/0004-6256/143/5/125
- Mirabel, I. F., Booth, R. S., Johansson, L. E. B., Garay, G., & Sanders, D. B. (1990, September). CO(1-0) emission from luminous infrared galaxies in the southern hemisphere. *A&A*, *236*, 327-332.
- Mo, H., Van den Bosch, F., & White, S. (2010). *Galaxy formation and evolution*. Cambridge University Press.

- Morokuma-Matsui, K., Baba, J., Sorai, K., & Kuno, N. (2015, June). CO emissions from optically selected galaxies at $z \sim 0.1-0.2$: Tight anti-correlation between molecular gas fraction and 4000 Å break strength. *PASJ*, *67*, 36. doi: 10.1093/pasj/psv005
- Noeske, K. G., Faber, S. M., Weiner, B. J., Koo, D. C., Primack, J. R., Dekel, A., ... Bundy, K. (2007, May). Star Formation in AEGIS Field Galaxies since $z=1.1$: Staged Galaxy Formation and a Model of Mass-dependent Gas Exhaustion. *ApJ*, *660*, L47-L50. doi: 10.1086/517927
- Obreschkow, D., & Rawlings, S. (2009, April). Understanding the H₂/HI ratio in galaxies. *MNRAS*, *394*, 1857-1874. doi: 10.1111/j.1365-2966.2009.14497.x
- Papadopoulos, P. P., van der Werf, P. P., Xilouris, E. M., Isaak, K. G., Gao, Y., & Mühle, S. (2012, November). The molecular gas in luminous infrared galaxies - I. CO lines, extreme physical conditions and their drivers. *MNRAS*, *426*, 2601-2629. doi: 10.1111/j.1365-2966.2012.21001.x
- Peng, Y.-j., Lilly, S. J., Kovač, K., Bolzonella, M., Pozzetti, L., Renzini, A., ... Scaramella, R. (2010, September). Mass and Environment as Drivers of Galaxy Evolution in SDSS and zCOSMOS and the Origin of the Schechter Function. *ApJ*, *721*, 193-221. doi: 10.1088/0004-637X/721/1/193
- Popping, G., Caputi, K. I., Somerville, R. S., & Trager, S. C. (2012, September). An indirect measurement of gas evolution in galaxies at $0.5 < z < 2.0$. *MNRAS*, *425*, 2386-2400. doi: 10.1111/j.1365-2966.2012.21702.x
- Rodighiero, G., Daddi, E., Baronchelli, I., Cimatti, A., Renzini, A., Aussel, H., ... Zamorani, G. (2011, October). The Lesser Role of Starbursts in Star Formation at $z = 2$. *ApJ*, *739*, L40. doi: 10.1088/2041-8205/739/2/L40
- Saintonge, A., Kauffmann, G., Kramer, C., Tacconi, L. J., Buchbender, C., Catinella, B., ... Sievers, A. (2011, July). COLD GASS, an IRAM legacy survey of molecular gas in massive galaxies - I. Relations between H₂, H I, stellar content and structural properties. *MNRAS*, *415*, 32-60. doi: 10.1111/j.1365-2966.2011.18677.x
- Saintonge, A., Kauffmann, G., Wang, J., Kramer, C., Tacconi, L. J., Buchbender, C., ... Sievers, A. (2011, July). COLD GASS, an IRAM legacy survey of molecular gas in massive galaxies - II. The non-universality of the molecular gas depletion time-scale. *MNRAS*, *415*, 61-76. doi: 10.1111/j.1365-2966.2011.18823.x
- Salim, S., Rich, R. M., Charlot, S., Brinchmann, J., Johnson, B. D., Schiminovich, D., ... Yi, S. K. (2007, December). UV Star Formation Rates in the Local Universe. *ApJS*, *173*, 267-292. doi: 10.1086/519218
- Salpeter, E. E. (1955, January). The Luminosity Function and Stellar Evolution. *ApJ*, *121*, 161. doi: 10.1086/145971

- Sanders, D. B., & Mirabel, I. F. (1996). Luminous Infrared Galaxies. *ARA&A*, *34*, 749. doi: 10.1146/annurev.astro.34.1.749
- Sargent, M. T., Daddi, E., Béthermin, M., Aussel, H., Magdis, G., Hwang, H. S., ... da Cunha, E. (2014, September). Regularity Underlying Complexity: A Redshift-independent Description of the Continuous Variation of Galaxy-scale Molecular Gas Properties in the Mass-star Formation Rate Plane. *ApJ*, *793*, 19. doi: 10.1088/0004-637X/793/1/19
- Schmidt, M. (1959, March). The Rate of Star Formation. *ApJ*, *129*, 243. doi: 10.1086/146614
- Schreiber, C., Pannella, M., Elbaz, D., Béthermin, M., Inami, H., Dickinson, M., ... Scott, D. (2015, March). The Herschel view of the dominant mode of galaxy growth from $z = 4$ to the present day. *A&A*, *575*, A74. doi: 10.1051/0004-6361/201425017
- Scoville, N. Z., Young, J. S., & Lucy, L. B. (1983, July). The distribution of molecular clouds in the nuclear region of NGC 1068. *ApJ*, *270*, 443-445. doi: 10.1086/161139
- Sharon, C. E., Riechers, D. A., Hodge, J., Carilli, C. L., Walter, F., Weiß, A., ... Wagg, J. (2016, August). A Total Molecular Gas Mass Census in $Z \sim 2 - 3$ Star-forming Galaxies: Low-J CO Excitation Probes of Galaxies' Evolutionary States. *ApJ*, *827*, 18. doi: 10.3847/0004-637X/827/1/18
- Silverman, J. D., Daddi, E., Rodighiero, G., Rujopakarn, W., Sargent, M., Renzini, A., ... Zamorani, G. (2015, October). A Higher Efficiency of Converting Gas to Stars Pushes Galaxies at $z \sim 1.6$ Well Above the Star-forming Main Sequence. *ApJ*, *812*, L23. doi: 10.1088/2041-8205/812/2/L23
- Smail, I., Ivison, R. J., Blain, A. W., & Kneib, J.-P. (2002, March). The nature of faint submillimetre-selected galaxies. *MNRAS*, *331*, 495-520. doi: 10.1046/j.1365-8711.2002.05203.x
- Solomon, P., & Bout, P. (2005). Molecular gas at high redshift. *arXiv preprint astro-ph/0508481*.
- Solomon, P. M., Downes, D., Radford, S. J. E., & Barrett, J. W. (1997, March). The Molecular Interstellar Medium in Ultraluminous Infrared Galaxies. *ApJ*, *478*, 144-161.
- Sparke, L. S., & Gallagher III, J. S. (2000). Galaxies in the universe: an introduction. *Galaxies in the Universe, by Linda S. Sparke and John S. Gallagher, III, pp. 416. ISBN 0521592410. Cambridge, UK: Cambridge University Press, September 2000., 1.*

- Speagle, J. S., Steinhardt, C. L., Capak, P. L., & Silverman, J. D. (2014, October). A Highly Consistent Framework for the Evolution of the Star-Forming "Main Sequence" from $z \sim 0-6$. *ApJS*, *214*, 15. doi: 10.1088/0067-0049/214/2/15
- Tacconi, L. J., Neri, R., Genzel, R., Combes, F., Bolatto, A., Cooper, M. C., ... Weiner, B. (2013, May). Phibss: Molecular Gas Content and Scaling Relations in $z \sim 1-3$ Massive, Main-sequence Star-forming Galaxies. *ApJ*, *768*, 74. doi: 10.1088/0004-637X/768/1/74
- Tan, Q., Daddi, E., Sargent, M., Magdis, G., Hodge, J., Béthermin, M., ... Walter, F. (2013, October). A Deep Search for Molecular Gas in Two Massive Lyman Break Galaxies at $z = 3$ and 4: Vanishing CO-emission Due to Low Metallicity? *ApJ*, *776*, L24. doi: 10.1088/2041-8205/776/2/L24
- U, V., Sanders, D. B., Mazzarella, J. M., Evans, A. S., Howell, J. H., Surace, J. A., ... Petric, A. O. (2012, November). Spectral Energy Distributions of Local Luminous and Ultraluminous Infrared Galaxies. *ApJS*, *203*, 9. doi: 10.1088/0067-0049/203/1/9
- Veilleux, S., Rupke, D. S. N., Kim, D.-C., Genzel, R., Sturm, E., Lutz, D., ... Barnes, J. E. (2009, June). Spitzer Quasar and Ullirg Evolution Study (QUEST). IV. Comparison of 1 Jy Ultraluminous Infrared Galaxies with Palomar-Green Quasars. *ApJS*, *182*, 628-666. doi: 10.1088/0067-0049/182/2/628
- Weiß, A., Walter, F., & Scoville, N. Z. (2005, August). The spectral energy distribution of CO lines in M 82. *A&A*, *438*, 533-544. doi: 10.1051/0004-6361:20052667
- Zavala, J. A., Yun, M. S., Aretxaga, I., Hughes, D. H., Wilson, G. W., Geach, J. E., ... Zeballos, M. (2015, September). Early Science with the Large Millimeter Telescope: observations of dust continuum and CO emission lines of cluster-lensed submillimetre galaxies at $z=2.0-4.7$. *MNRAS*, *452*, 1140-1151. doi: 10.1093/mnras/stv1351

LIST OF FIGURES

1.1	Cosmic star formation History	4
1.2	SFRD vs. gas surface density	6
1.3	Comoving IR energy density vs. lookback time	8
3.1	Database overview	18
3.2	SED template	21
3.3	Included wavebands	22
3.4	SED of two low- z galaxies	28
3.5	SED of two high- z galaxies	28
4.1	L_{IR} and $L'_{\text{CO}(1-0)}$ for the full data sample	30
4.2	L_{IR} and $L'_{\text{CO}(1-0)}$ for the <i>Herschel</i> -detected data sample	31
4.3	L_{IR} and $L'_{\text{CO}(1-0)}$ for the full data sample with regression line from Sargent+14	32
4.4	L_{IR} vs. $L'_{\text{CO}(1-0)}$ for the data sample excluding upper limits	33
4.5	$L_{\text{IR}} - L'_{\text{CO}}$ relation for the data sample with stellar mass values	34
4.6	SFR/SFR _{MS} and SFE = $L_{\text{IR}}/L'_{\text{CO}}$ for the full data sample	36
4.7	SFE vs. distance to MS	37
4.8	$L_{\text{IR}}/M_{\text{dust}}$ and $L'_{\text{HCN}(1-0)}/L'_{\text{CO}(1-0)}$ for the <i>Herschel</i> -detected data sample	38
4.9	$L_{\text{IR}}/M_{\text{dust}}$ and SFE = $L_{\text{IR}}/L'_{\text{CO}(1-0)}$ for the <i>Herschel</i> -detected data sample	38
C.1	SEDs part 1 of 16	68
C.2	SEDs 2 of 16	69
C.3	SEDs 3 of 16	70
C.4	SEDs 4 of 16	71
C.5	SEDs 5 of 16	72
C.6	SEDs 6 of 16	73
C.7	SEDs 7 of 16	74
C.8	SEDs 8 of 16	75
C.9	SEDs 9 of 16	76
C.10	SEDs 10 of 16	77
C.11	SEDs 11 of 16	78
C.12	SEDs 12 of 16	79

C.13 SEDs 13 of 16	80
C.14 SEDs 14 of 16	81
C.15 SEDs 15 of 16	82
C.16 SEDs 16 of 16	83

LIST OF TABLES

2.1	Rest frequencies for various J transitions of the CO molecule.	12
2.2	Conversion factors for higher CO rotational states.	12
3.1	SED fitted parameters for selected <i>Herschel</i> -selected galaxies in the catalog. Columns are (from left) galaxy reference name, redshift, reduced χ^2 value, logarithmic infrared luminosity, logarithmic dust mass, intensity field, dust weighted mean starlight intensity, and the fraction of dust enclosed in PDR regions. All galaxies in the sample are listed in Appendix B.2.	27
B.1	Overview of each telescope, instrument, wavebands, and references used to create the database.	64
B.2	SED fitted parameters for all <i>Herschel</i> -selected galaxies in the catalog. Columns are (from left) galaxy reference name, redshift, reduced χ^2 value, logarithmic infrared luminosity, logarithmic dust mass, intensity field, dust weighted mean starlight intensity, and the fraction of dust enclosed in PDR regions.	66

A THE PROGRAM

A.1 USED SOFTWARE

For this project I decided to use python (version 2.7) as the programming language and saving data using a MySQL database. Both technologies was new to me, so time was spent on learning the language and syntax and studying the astropy package ⁷ and the astroquery package Ginsburg et al. [2013].

A.1.1 THE CHALLENGES

The major challenge was handling the different format of data. The overall principal was to read the data with astroquery and save it in a common format in order to search the data across different sources. Most of the data would be retrieved as astropy.table, but with very different column definitions. The solution to this was saving all table rows in a single database table `catalogue_reads` consisting of 4 key columns and 300 columns of text (named from `col1` to `col300`). The key columns was an unique row id (auto value), the catalogue name (for example NED, ViZier etc.), the table name (within the catalogue) and a reference name for the object (by default the NED reference name). The number of columns was found by experimenting with the maximum of retrieved columns using astroquery. Every time a new table was read within a catalogue, the column definition was saved in another table `catalogue_cols`. This information was then used to create a database view for that table as a subset of the rows in `catalogue_reads` and with a translation of the text columns to the actual read table definition. Using this approach all read astropy.table could be saved in the same database table event though they had different column definitions.

A.1.2 THE BUILDING BLOCKS

The resulting program consists of different modules written to perform subtasks in order to read and handle the data retrieved using astroquery or imported into the database otherwise (for example loaded from excel) or work with the actual created data. Overall the following modules has been created:

⁷This research made use of Astropy, a community-developed core Python package for Astronomy (Astropy Collaboration, 2013) <http://www.astropy.org/>

- `cat_reader`: the main module performing querying, saving data and building the database, extracting data to idl and creating some of the plots.
- `cat_mappings`: extracting data columns from different data tables to be used in calculations and new columns in resulting data tables.
- `cat_load_data`: loading data into the database with excel as primary source, mostly used to load data from articles.
- `cat_fits`: module used to load fits data.

Using these modules additional python scripts was written in order to handle data for specific surveys.

A.2 SELECTED FUNCTION DECLARATIONS

This section contains the declarations for some of the used functions from the created modules. The modules contains far more functions (and sub functions).

A.2.1 `CAT_READER.TRY_NED_FROM_QUERY_NAME`

```
def try_ned_from_query_name(queryname, namecol, fromname = ''):
    """
    Perform NED search based on result of query in mySql.

    Parameters
    -----
    queryname: str
        The mySQL query returning a list of names

    namecol: str
        The column name in query containing then object name to search on

    Returns
    -----
    None
    """
```

A.2.2 `CAT_READER.FULL_NAME_SEARCH_ON_QUERY`

```
def full_name_search_on_query(queryname, namecol, r):
    """
    Perform search in all used catalogues based on name query in mySql.

    Parameters
    -----
    queryname: str
        The mySQL query returning a list of names

    namecol: str
        The column name in query containing then object name to search on

    r: unit
        The radius to be used if searching in IRSA.

    Returns
```

```

-----
None
"""

```

A.2.3 CAT_READER.LOAD_EXCEL

Used by the `cat_load_data` module to load different Excel files.

```

def load_excel(filename, namecol, racol=None, deccol=None, unit='deg', r=10*u.
arcsec):
    """
    Loads an Excel file of data to the catalogue "Manual"

    Parameters
    -----
    filename: str
        The Excel file name to load

    namecol: str
        The column name containing the object name to check against NED db

    racol: str
        The column name containing the object RA coordinate - if no name match is
        found, the coordinate is used to find the actual object.

    deccol: str
        The column name containing the object DEC coordinate - if no name match is
        found, the coordinate is used to find the actual object.

    unit: str
        The unit of the given coordinates

    r: radius
        The radius used when searching on the coordinate

    Returns
    -----
    tablename: str
        The given tablename containing the Excel data.
    """

```

A.2.4 CAT_READER.ADD_CALC_COLUMN

This function is used to map existing datacolumns to new calculated columns.

```

def add_calc_column(toview, tocolumn, fromview, fromcolumn=None, calc=None, where=
None):
    """
    This function adds a calculated column to a view.
    (if the value of the "fromcolumn" in the source view "fromview" is null
    then the calculation is replaced by a null value)

    Parameters:
    -----
    toview : str
        The receiving view
    tocolumn : str
        The new column name.
    fromview : str
        The name of the source mysql view.
    fromcolumn : str
        The source column name in the mysql source view.
        If None, the calculation is performed without ref. to a specific column (
        error i ? is used)

```

```

calc : str
    A calculation made on the fromcolumn.
    Use ? to refer to the from column name.
where : str
    A where clause to be used when fetching data
    Default None
"""

```

A.3 SELECTED PYTHON SCRIPTS

A.3.1 RESULT_BUILDER.PY

The script is an example of how to build a table of results, combining different sources and creating the output files needed to further work.

```

__author__ = 'isabellacortzen'
import cat_reader as cat
import cat_mappings as map
import cat_fits as cfits

# Build results:
def buildresult(resultname):
    # Clear previous data
    cat.clearview(resultname)
    # Add auto column mapping from NED photometry (some of them)
    cat.add_ned_photometry(resultname)
    # Add auto column mapping from Vizier photometry (some of them)
    cat.add_vizier_photometry(resultname)

    # Add all manual data
    map.add_all_manuel(resultname)
    map.add_man_vizier(resultname)

    cfits.add_calc_fits_all(resultname)

    # Now build mySql table named resultname...
    if cat.buildtable(resultname):
        # Finally insert data...
        cat.inserttable(resultname)
    return

def plotsubset(sourceresult, targetresult, targetdir, requirementsql=None):
    # Where do we want output?
    workdir = cat.initdir(targetdir, True) # Last parameter: if True old files
        are deleted first...

    # Copy result table
    cat.copytable(sourceresult, targetresult)

    # Remove unwanted ref_names based on sql query
    if requirementsql is not None:
        cat.refnamerequired(targetresult, requirementsql)

    # Write resulting data:
    cat.flush_all(targetresult, workdir)

    # Create pro files
    cat.plot_all('csv', workdir)
    cat.profile_all('csv', workdir)
    cat.plot_all_idl(workdir, 'png' , workdir)

# =====

```



```

#   MAIN PART
# =====

# Build the complete dataset and call it "result"
buildresult('result')

# > OBS!!!! <
# Once the above table has been build, you can comment out the call, som that it
# is faster - you only need to rebuild if new data has been added!!!

# Create subset table of table "result" called "my_ref_names_result", placed in
# folder /my_ref_names, containing all ref_names from galaxdb.my_ref_names_v:
plotsubset('result', 'my_ref_names_result', 'my_ref_names', "select ref_name from
galaxdb.my_ref_names_v")

```

A.3.2 ADD_COLS.PY

This script is an example of how to extract column values from data views by searching for columns based on search patterns. The script results in a new python script (named the selected resultname and the extension py) containing all the found columns matching the search criteria written as a commented call to the function `cat_reader.add_calc_column`. The script also contains the complete dataview definition in order to understand if the column is correct to add. The task is to read the file, look at the dataview definition and evaluate if the found columns is a candidate to be added to the resulting view; if this is the case the line is to be uncommented and at the columns are then added by actually running the script.

```

__author__ = 'isabellacortzen'
import cat_reader as cat
import sys

"""
    Set the resultname - the result will be saved in a python file called the same
"""

resultname = 'stellarmass'

# Redirect output to new python file
orig_stdout = sys.stdout
fname = resultname + '.py'
f = file(fname, 'w')
print ("Output is written to file " + fname)
sys.stdout = f

# Write already existing column mapping to begin with
cat.print_mappings(resultname, False)

# Output possible column mapping based on search criterias:
#
# cat.print_unused_columns(unit, name, formula, where, cat)
#
# Retrieve all columns not mapped based on unit or name filter
# and print them to screen to use it for further editing.
# The outcome is a series of add_calc_column calls to be edited.
#
# Parameters
# -----
# unit: str
#     Filter query on unit, use % as wildcard.

```

```

#           Ex: "%Hz%" will match GHz, MHz etc.
# name: str
#           Filter query on field name, use % as wildcard.
#           Ex: "%allwise" will match w4mpro_allwise, w4sigmpro_allwise, AllWISE etc
#
# formula: str or 'None'
#           Contains a mySql calculation, where the char '?' will be replaced
#           at runtime with the table field name and added as a parameter to cat.
#           add_calc_column.
#           Ex: "abs(convert(replace(replace(?, '+', ''), '/', ''), decimal(20,10)))" on
#           field F10
#           produces "abs(convert(replace(replace(F10, '+', ''), '/', ''), decimal
#           (20,10)))"
#           If 'None' then only field value will be used as value.
# where: str or None
#           Contains a mySql where clause, where the char '?' will be replaced
#           at runtime with the table field name and added as a parameter to cat.
#           add_calc_column.
# cat: str or None
#           Contains a filter of catalogue in order to only look at table results from
#           one catalogue.
# constants: array of str or 'None'
#           Contains array of constants column names to be added each view at runtime a
#           cat.add_const_column
#           will be added for each column name in the array.
#
# Example: searching for unit of stellarmasses on columns:
cat.print_unused_columns('%MSUN%', '%', '', 'ifnull(?,0)>0', '%', ['IMF', 'imf_link
'])

sys.stdout = orig_stdout

print "Finished with creating the python file."
print
print "Please edit the file (determine if add_calc_columns call should be in
commented), "
print "and run the edited file in order to create the mappings."
print
print "Then edit add_cols.py with a new filter setting and repeat the process,"
print "until all column mapping is finished."

```

Running the script results in the following stellarmass.py:

```

import cat_reader as cat

# Autogenerated from print_mappings with parameter newviewname = 'stellarmass'

#-----
#   stellarmass
#-----

# Now build results:
newviewname = 'stellarmass'
# Clear previous data
cat.clearview(newviewname)
# Add column mappings:

# --- Catalogue IRSA, table cosmos_xgal --- select * from readerdb.
#   IRSA_cosmos_xgal_v

#           1. gal_id           gal_id           None           object None
#           2. mag_auto         mag_auto         mag             float64 %r
#           3. ra               ra               deg             float64 %7.3f
#           4. dec              dec              deg             float64 %7.3f
#           5. clon             clon             None            object None
#           6. clat             clat             None            object None
#           7. sm               sm               log(M / Msun)  float64 %r

```

```

#      8. sm_err          sm_err          log(M / Msun) float64 %r
#      9. zphot          zphot          None          float64 %r
#     10. zphot_errlo    zphot_errlo    None          float64 %r
#     11. zphot_errhi    zphot_errhi    None          float64 %r
#     12. mmggs          mmggs          None          int32  None
#     13. p_mem          p_mem          None          float64 %r
#     14. group_id       group_id       None          int32  None
#     15. group_flag     group_flag     None          int32  None
#     16. dist_mmggs     dist_mmggs     1 / R199      float64 %r
#     17. mmggs_zbest    mmggs_zbest    None          int32  None
#     18. p_mem_zbest    p_mem_zbest    None          float64 %r
#     19. group_id_zbest group_id_zbest None          int32  None
#     20. group_flag_zbest group_flag_zbest None          int32  None
#     21. dist_mmggs_zbest dist_mmggs_zbest 1 / R199      float64 %r
#     22. mnuv_mr       mnuv_mr       mag           float64 %r
#     23. dist          dist          arcs          float64 %r
#     24. angle         angle         deg           float64 %r
#     25. id            id            None          object None

cat.add_calc_column(newviewname, 'sm_err', 'readerdb.IRSA_cosmos_xgal_v', 'sm_err',
, '', 'ifnull(sm_err,0)>0') # Column [sm_err] (Unit='log(M / Msun)') :
cat.add_const_column(newviewname, 'IMF', 'readerdb.IRSA_cosmos_xgal_v', '', '
ifnull(sm_err,0)>0') # Constant column IMF
cat.add_const_column(newviewname, 'imf_link', 'readerdb.IRSA_cosmos_xgal_v', '', '
ifnull(sm_err,0)>0') # Constant column imf_link

-----
Skipping over 7000 lines...
-----

# --- Catalogue VIZIER, table J/PAZh/38/571/catalog --- select * from readerdb.
VIZIER_J_PAZh_38_571_catalog_v

#      1. _RAJ2000      _RAJ2000      deg          float64 %8.4f Right ascension (FK5,
Equinox=J2000.0) (computed by Vizier, not part of the original data)
#      2. _DEJ2000      _DEJ2000      deg          float64 %8.4f Declination (FK5, Equinox=
J2000.0) (computed by Vizier, not part of the original data)
#      3. _r            _r            arcmin       float64 %5.3f Distance from center
(009.8936+02.8342) [Galactic]
#      4. Cluster       Cluster       None         |S17      None     Cluster name
#      5. n_Cluster     n_Cluster     None         |S1       None     [*] far Cluster (1)
#      6. GLON          GLON          deg          float64 %8.4f Galactic longitude
#      7. GLAT          GLAT          deg          float64 %8.4f Galactic latitude
#      8. d              d             pc           int32     None     ? Heliocentric distance [
NULL integer written as an empty string]
#      9. x              x             pc           int32     None     ? Heliocentric distance
towards Gal. center [NULL integer written as an empty string]
#     10. y              y             pc           int32     None     ? Heliocentric distance
towards Gal. rotation [NULL integer written as an empty string]
#     11. z              z             pc           int32     None     ? Heliocentric distance
towards N. Gal. Pole [NULL integer written as an empty string]
#     12. RG            RG            kpc          float32 %5.2f ? Galactocentric radius
#     13. VR            VR            km / s       float32 %5.1f ? Galactocentric cylindrical
velocity component towards Gal. anticenter
#     14. VH            VH            km / s       float32 %5.1f ? Galactocentric cylindrical
velocity component towards Gal. rotation
#     15. VZ            VZ            km / s       float32 %6.1f ? Galactocentric cylindrical
velocity component towards N. Gal. Pole
#     16. e              e             None         float32 %5.2f ? Orbital eccentricity
#     17. Zmax          Zmax         kpc          float32 %5.2f ? Maximum distance above the
Galactic plane
#     18. Ra            Ra            kpc          float32 %5.2f ? Apogalactic distance
#     19. Rp            Rp            kpc          float32 %5.2f ? Perigalactic distance
#     20. Age           Age           Gyr          float32 %6.3f ? Cluster age
#     21. logM          logM         [Msun]       float32 %5.2f ? Cluster mass
#     22. CC            CC            [-]          float32 %5.2f ? Central concentration, log
(rcl/rco)
#     23. ell           ell           None         float32 %5.2f ? Cluster ellipticity

```

```

# 24. __Fe_H_ __Fe_H_ [Sun] float32 %5.2f ? Cluster metallicity
# 25. r__Fe_H_ r__Fe_H_ None |S5 None Reference for [Fe/He], in
refs.dat file
# 26. __Mg_Fe_ __Mg_Fe_ [Sun] float32 %5.2f ? Mg/Fe abundance ratio
# 27. r__Mg_Fe_ r__Mg_Fe_ None |S29 None Reference for [Mg/Fe], in
refs.dat file
# 28. Sub Sub None uint8 None [1/3]? Subsystem: 1=thin
disk, 2=thick disk, 3=halo [NULL integer written as an empty string]
# 29. SimbadName SimbadName None |S20 None Designation understandable
by the FireBrick Simbad data-base
# 30. _RA.icrs _RA.icrs deg float64 %8.4f Right ascension (ICRS) (
computed by Vizier, not part of the original data)
# 31. _DE.icrs _DE.icrs deg float64 %8.4f Declination (ICRS) (computed
by Vizier, not part of the original data)

cat.add_calc_column(newviewname, 'logM', 'readerdb.VIZIER_J_PAZh_38_571_catalog_v'
, 'logM', '', 'ifnull(logM,0)>0') # Column [logM] (Unit='[Msun]') : ? Cluster
mass
#cat.add_const_column(newviewname, 'IMF', 'readerdb.VIZIER_J_PAZh_38_571_catalog_v'
, '', 'ifnull(logM,0)>0') # Constant column IMF
#cat.add_const_column(newviewname, 'imf_link', 'readerdb.
VIZIER_J_PAZh_38_571_catalog_v', '', 'ifnull(logM,0)>0') # Constant column
imf_link

# Total : 549 lines.

```

B TABLES

B.1 INCLUDED TELESCOPES AND INSTRUMENTS

Telescope	Instrument	Wavebands	Reference
2MASS	2MASS J 2MASS H 2MASS K _s	<i>J</i> (1.235 μm) <i>H</i> (1.662 μm) <i>K_s</i> (2.159 μm)	Ref 2MASS
APEX	LABOCA	870 μm	Ref APEX
<i>Herschel</i>	PACS1 PACS2 PACS3 SPIRE1 SPIRE2 SPIRE3	70 μm 100 μm 160 μm 250 μm 350 μm 500 μm	Ref Herschel
IRAS	Survey Array 1 Survey Array 2 Survey Array 3 Survey Array 4	12 μm 25 μm 60 μm 100 μm	Ref IRAC
Planck	LFI-3 HFI-2 HFI-3 HFI-4 HFI-5 HFI-6	70 GHz (4260 μm) 143 GHz (2098 μm) 217 GHz (1382 μm) 353 GHz (850 μm) 545 GHz (550 μm) 857 GHz (350 μm)	Ref Planck
<i>Spitzer</i>	IRAC1 IRAC2 IRAC3 IRAC4 MIPS1 MIPS2 MIPS3	3.6 μm 4.5 μm 5.8 μm 8.0 μm 24 μm 70 μm 160 μm	Ref Spitzer
JCMT	SCUBA 1 SCUBA 2	450 μm 850 μm	Ref JCMT
WISE/NEOWISE	WISE/NEOWISE 1 WISE/NEOWISE 2 WISE 3 WISE 4	3.4 μm 4.6 μm 12 μm 24 μm	WISE ref

Table B.1: Overview of each telescope, instrument, wavebands, and references used to create the database.

B.2 *Herschel*-DETECTED SAMPLE

Galaxy	z	χ^2_ν	$\log L_{\text{IR}}$ [L_\odot]	$\log M_{\text{dust}}$ [M_\odot]	U_{min}	$\langle U \rangle$	γ %
2MASS J10323767+5808446	0.25	16.53	11.97	8.67	15	15	0
2MASX J05210136-2521450	0.04	0.14	12.1	8.34	15	45.32	0.2
2MASX J10200023+0813342	0.05	12.53	11.66	8.22	20	20.79	0
2MASX J10522356+4408474	0.09	8.1	12.19	8.63	25	27.4	0.01

Continued on next page

Table B.2 Continued from previous page

Galaxy	z	χ^2_ν	$\log L_{\text{IR}}$ [L_\odot]	$\log M_{\text{dust}}$ [M_\odot]	U_{min}	$\langle U \rangle$	γ %
2MASX J10591815+2432343	0.04	15.98	12.05	8.39	25	34.6	0.04
2MASX J11531422+1314276	0.13	62.95	12.39	8.65	25	41.79	0.07
2MASX J13463926+2306181	0.14	0.2	12.28	8.69	25	32.20	0.03
2MASX J14284971+3432397	0.22	0.5	11.87	9.01	5	5.39	0.01
2MASX J17232194-0017009	0.04	8.20	12.36	8.82	25	26.2	0
2MASX J18113342+0131427	0.03	0.55	11.6	8.33	12	14.48	0.02
2MASX J19322229-0400010	0.09	0.36	12.4	8.77	25	32.20	0.03
2MASX J23390127+3621087	0.06	8.78	12.13	8.54	25	29.8	0.02
ARP 220	0.02	3.67	12.02	8.78	12	13.12	0.01
ARP 299	0.01	8.85	11.87	7.9	25	72.98	0.2
AzGN 01.2	4.05	17.48	13.17	9.61	25	27.16	0.01
BLAST J032904-284759	0.29	0.62	11.84	9.11	4	4.02	0
BzK 04171	1.47	11.38	11.9	8.63	15	15	0
BzK 12591	1.6	12.85	12.35	8.82	25	27.4	0.01
BzK 16000	1.52	11.45	11.73	9.13	3	3.35	0.01
BzK 17999	1.41	11.5	11.99	8.61	20	20	0
BzK 21000	1.52	9.52	12.32	9.23	7	10.04	0.04
COSBO 11	1.83	12.21	13.02	9.5	25	26.2	0
Cosmic Eyelash	2.32	0.98	12.36	10.72	12	12	0
DEEP2 13011148	1.17	15.01	11.64	8.06	25	32.20	0.03
DEEP2 13017614	1.18	11.1	11.84	8.86	8	8	0
FFN 228	1.22	13.52	12.54	9.12	20	20	0
GALEX J032818.0-274307	0.25	0.19	11.84	8.82	8	8	0
GALEXASC J004014.61-432008.6	0.27	0.14	11.57	8.96	3	3.28	0.01
GALEXMSC J042604.91+144340.8	0.08	0.16	12.02	8.44	25	29.8	0.02
GALEXMSC J090302.89-014125.5	2.31	0.21	12.64	10.35	4	26.86	0.5
GOODS J123632.56+620800.2	1.99	14.24	12.16	9.63	0.8	2.89	0.2
GOODS J123750.89+621601.1	1.17	13.4	11.53	8.59	7	7	0
GOODS J123759.47+621733.2	1.08	14.79	11.48	8.22	15	15	0
HERMES J105751.1+573027	2.96	2.02	13.11	10.48	25	37	0.05
IC 0342	0	2.53	10.15	7.98	1.2	1.2	0
IC 0860	0.01	14.3	10.89	7.46	20	20	0
IC 0883	0.02	4.89	11.58	8.25	15	16.52	0.01
IC 1623	0.02	2.34	11.71	8.01	25	39.4	0.06
II Zw 096	0.04	5.38	11.9	8.12	25	46.59	0.09
III Zw 035	0.03	4.19	11.51	7.98	25	25.72	0
IRAC J123618.33+621550.8	2	10	12.72	9.43	15	15	0
IRAC J123711.34+621331.4	2	13.21	12.73	9.54	12	12	0
IRAS 02483+4302	0.05	0.09	11.73	8.5	12	12.74	0.01
IRAS 03158+4227	0.13	1.91	12.56	8.9	25	34.6	0.04
IRAS 08572+3915	0.06	5.73	12.1	8.16	25	72.98	0.2
IRAS 12112+0305	0.07	7.27	12.25	8.74	25	25.24	0
IRAS 17138-1017	0.02	15.22	11.33	7.67	25	37	0.05
Lock 850.16	1.6	10.41	12.59	9.52	7	9.28	0.03
MCG +12-02-001	0.02	9.57	11.42	8.14	10	15.26	0.05
MESSIER 063	0	10.62	10.12	7.56	3	3	0
MESSIER 064	0	6.31	9.65	6.85	5	5.11	0
MESSIER 066	0	13.16	10.48	6.99	25	25	0
MESSIER 077	0	3.73	11.34	7.81	7	29.83	0.3
MESSIER 082	0	4.06	10.46	6.8	25	37	0.05
MESSIER 083	0	16.03	10.73	7.17	25	29.8	0.02
MIPS J123644.0+621450.5	2.1	15.44	12.27	8.64	25	32.20	0.03
MIPS J142824.0+352619	1.33	12.12	12.3	9.99	12	12.25	0
MM J100020.54+023509.3	5.3	25.21	13.41	9.36	8	85.3	0.9
MRK 0231	0.04	13.42	12.49	8.71	25	48.99	0.1
MRK 0273	0.04	4.02	12.12	8.49	25	32.20	0.03
MRK 0331	0.02	5.33	11.49	7.77	25	39.4	0.06
NGC 0023	0.02	0.77	11.06	7.93	8	11.44	0.04
NGC 0253	0	53.95	10.64	6.9	25	41.79	0.07
NGC 0660	0	0.8	10.45	7.39	7	9.28	0.03
NGC 0695	0.03	0.09	11.66	8.66	7	8.52	0.02
NGC 0891	0	16.11	10.26	7.15	10	10.32	0

Continued on next page

Table B.2 Continued from previous page

Galaxy	z	χ^2_ν	$\log L_{\text{IR}}$ [L_\odot]	$\log M_{\text{dust}}$ [M_\odot]	U_{min}	$\langle U \rangle$	γ %
NGC 1144	0.03	4.57	11.47	7.91	25	29.8	0.02
NGC 1365	0.01	5.21	11.31	8.14	10	12.1	0.02
NGC 1614	0.02	6.63	11.71	7.73	25	72.98	0.2
NGC 2146	0	2.44	10.81	7.54	15	15.45	0
NGC 2276	0.01	25.83	10.95	7.43	25	26.44	0.01
NGC 2388	0.01	0.87	11.2	8.45	3	4.41	0.04
NGC 2623	0.02	11.51	11.52	7.96	25	27.4	0.01
NGC 2903	0	12.86	10.15	6.64	25	26.68	0.01
NGC 3079	0	1.79	10.6	7.11	25	25.12	0
NGC 3110	0.02	4.18	11.28	7.85	20	21.96	0.01
NGC 3628	0	6.6	10.48	7.53	7	7.15	0
NGC 3893	0	0.42	10.06	7.64	2	2.24	0.01
NGC 4030	0	5.97	10.56	8.18	2	2.05	0
NGC 4041	0	0.12	10.20	7.48	4	4.46	0.01
NGC 4414	0	2	10.06	6.67	20	21.18	0.01
NGC 4631	0	5.51	10.4	7.58	5	5.34	0.01
NGC 5005	0	0.19	10.20	7.63	3	3.11	0
NGC 5135	0.01	2.98	11.28	7.88	15	19.55	0.03
NGC 5653	0.01	0.72	10.99	7.74	12	14.48	0.02
NGC 5713	0.01	1.37	10.73	7.72	7	8.52	0.02
NGC 5775	0.01	9.17	10.68	7.21	25	25	0
NGC 5936	0.01	0.32	11	7.91	7	10.04	0.04
NGC 6240	0.02	0.1	11.82	8.32	15	24.1	0.06
NGC 6946	0	15.71	10.34	6.93	20	20	0
NGC 7469	0.02	4.37	11.64	7.85	25	48.99	0.1
NGC 7479	0.01	0.09	10.82	7.92	3	6.52	0.1
NGC 7591	0.02	0.51	11.07	8.14	5	6.68	0.03
NGC 7771	0.01	0.62	11.37	8.23	10	11.05	0.01
RG J105209.31+572202.8	2.11	14.36	12.27	8.69	20	29.82	0.05
SDSS J095900.61+022833.0	0.48	4.42	11.43	8.13	15	15.76	0
SDSS J095939.07+022249.6	0.47	14.13	10.99	8.82	1.2	1.2	0
SDSS J103557.85+585846.6	0.37	0.61	11.45	8.83	3	3.35	0.01
SDSS J105141.39+571951.7	1.21	12.1	12.68	9.25	20	20	0
SDSS J123548.03+621034.9	0.64	0.09	11.46	8.07	20	20	0
SDSS J123554.09+621043.5	0.51	1.10	11.4	9.12	0.8	1.63	0.08
SDSS J123642.56+620934.0	0.53	0.11	11.21	8.12	10	10	0
SDSS J123645.73+620754.4	1.43	11.3	12.31	8.66	25	37	0.05
SDSS J123646.20+621142.4	1.02	12.18	11.55	8.87	4	4	0
SDSS J140931.25+051131.2	0.27	inf	12.99	10.81	25	240.93	0.9
SDSS J141914.95+524929.5	1.2	7.18	12.71	9.43	12	15.72	0.03
SDSS J142005.35+530115.4	1.12	8.85	12.13	9.17	5	7.8	0.05
SDSS J143234.90+332832.2	0.25	1.54	11.9	8.6	15	15	0
SDSS J143631.95+343829.2	0.35	0.45	12.66	9.17	15	25.61	0.07
SDSS J171331.51+585804.4	0.44	1.13	12.39	8.93	20	21.96	0.01
SHADES J105307+572431	1.52	8.86	12.01	8.5	25	27.4	0.01
SMM J163541.2+661144	3.18	11.16	12.77	10.77	0.8	0.8	0
SSTXFLS J171411.5+601109	1.56	9.85	12.72	8.96	25	48.99	0.1
SSTXFLS J171822.6+590154	2.77	23.32	13.17	9.67	25	25.96	0
SSTXFLS J172109.1+601501	2.12	20.48	12.94	8.89	25	96.98	0.3
SSTXFLS J172422.0+593150	2.13	17.56	12.87	9.89	8	8	0
SSTXFLS J172428.4+601533	2.33	5.87	12.95	9.43	3	27.61	0.7
UGC 01845	0.02	0.43	11.09	7.87	10	13.15	0.03
UGC 03351	0.01	1.91	11.27	7.77	25	25.48	0
UGC 04881	0.04	1.37	11.72	8.31	15	19.55	0.03
UGC 05101	0.04	3.3	12.02	8.42	25	29.8	0.02
VII Zw 031	0.05	11.55	11.96	8.84	8	10.58	0.03

Table B.2: SED fitted parameters for all *Herschel*-selected galaxies in the catalog. Columns are (from left) galaxy reference name, redshift, reduced χ^2 value, logarithmic infrared luminosity, logarithmic dust mass, intensity field, dust weighted mean starlight intensity, and the fraction of dust enclosed in PDR regions.

Concluded

C FIGURES

C.1 *Herschel*-DETECTED SAMPLE

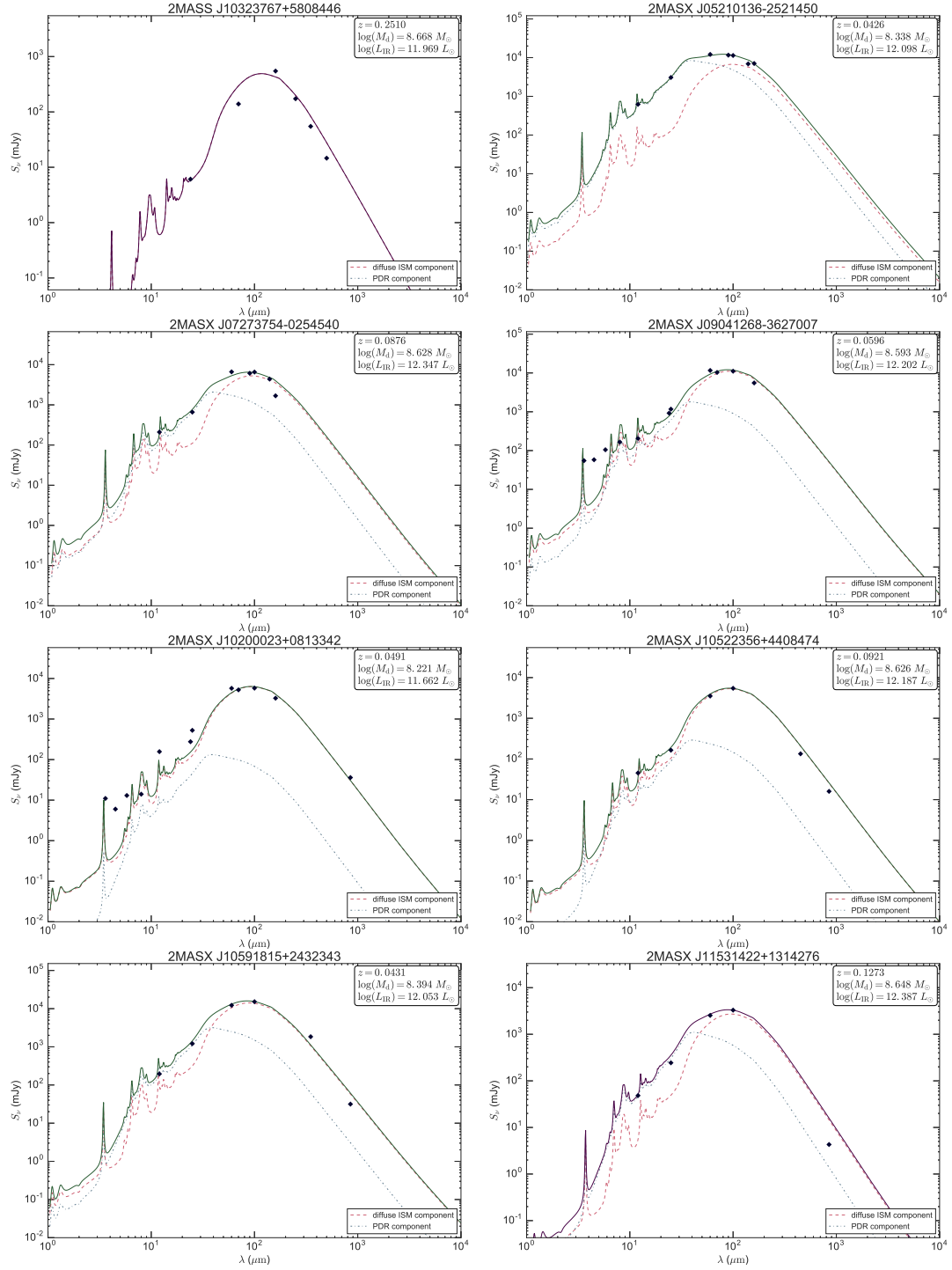


Figure C.1: Spectral energy distributions (SEDs) 1 of 16

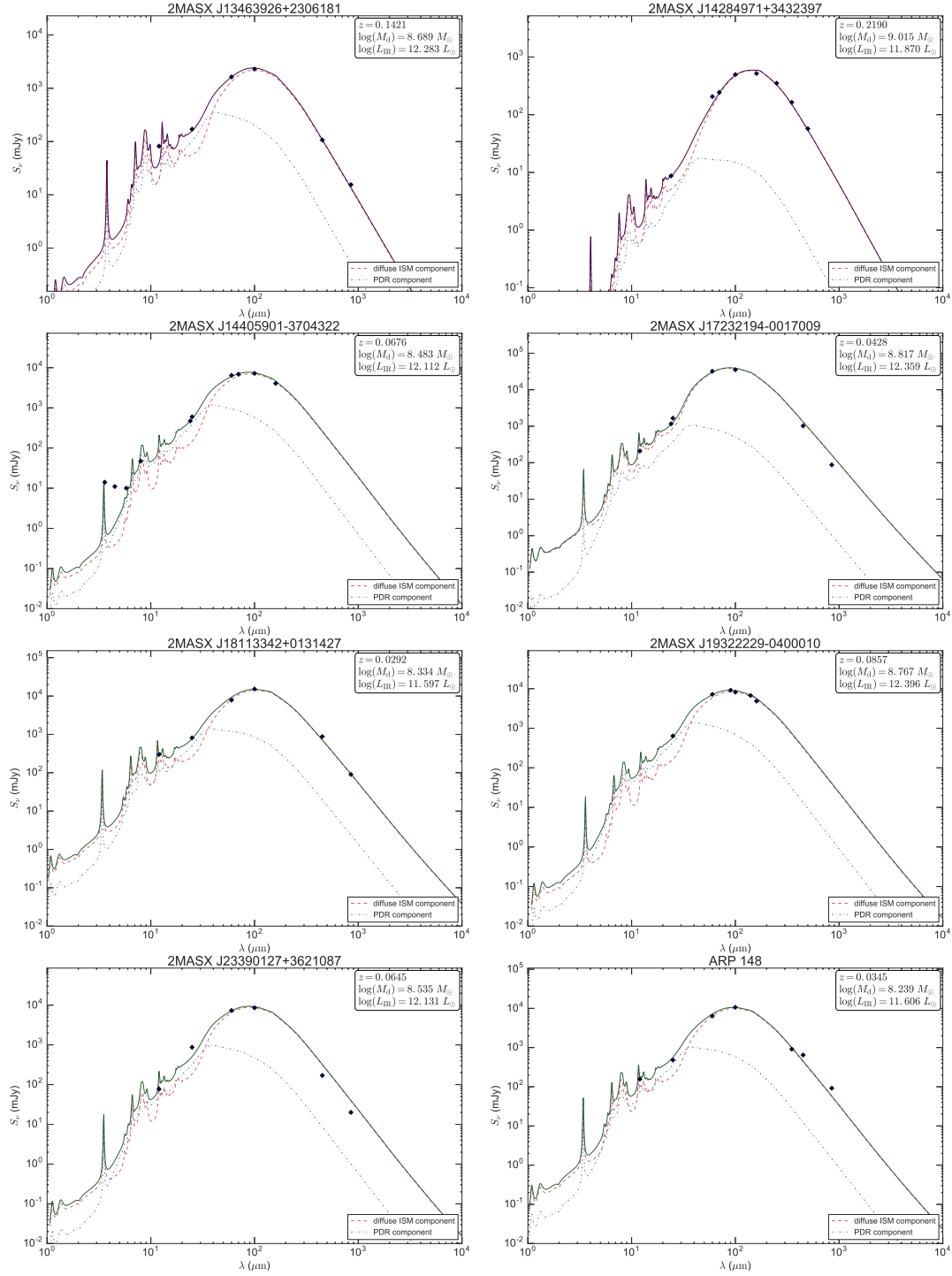


Figure C.2: Spectral energy distributions (SEDs) 2 of 16

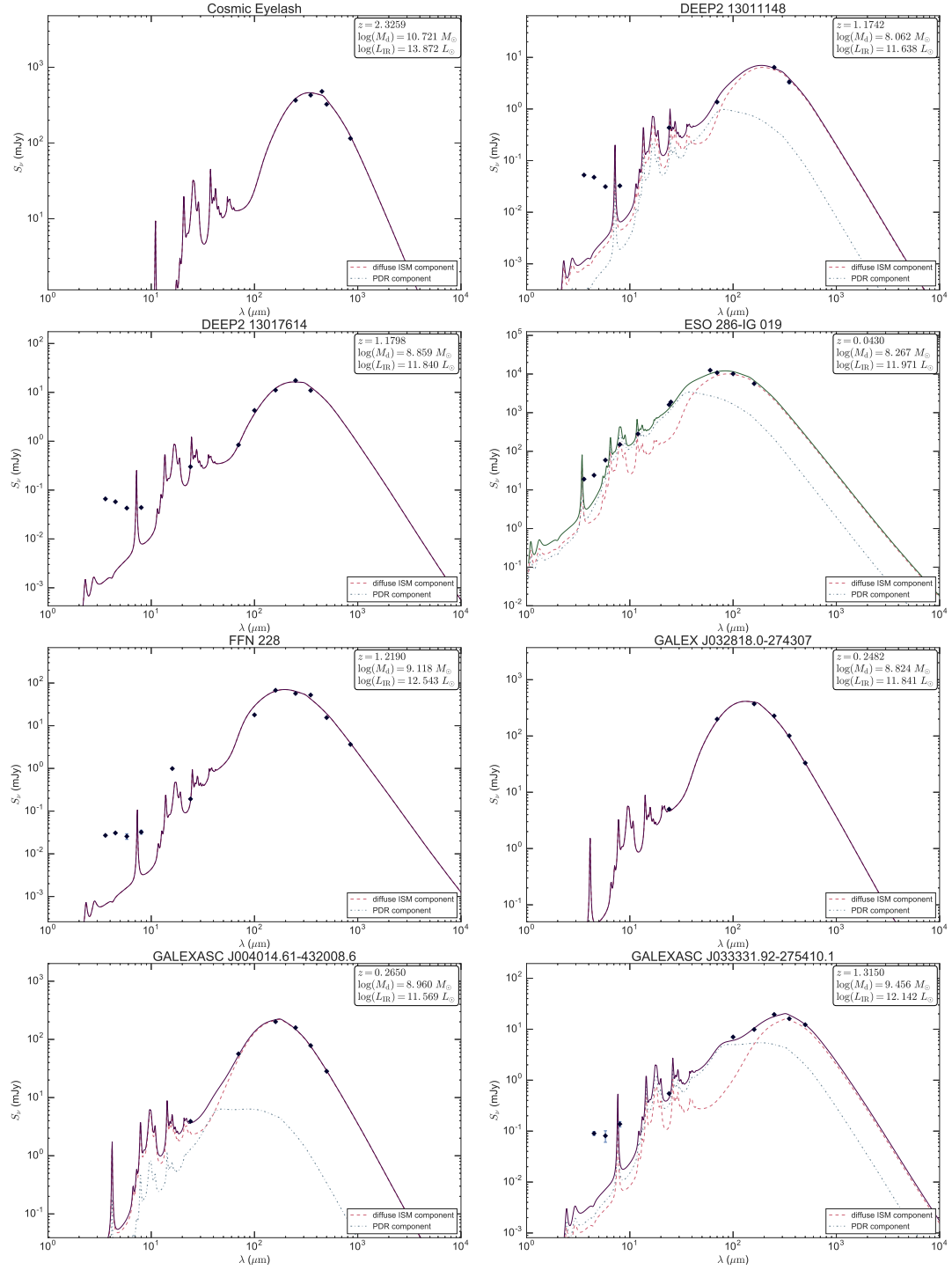


Figure C.3: Spectral energy distributions (SEDs) 3 of 16

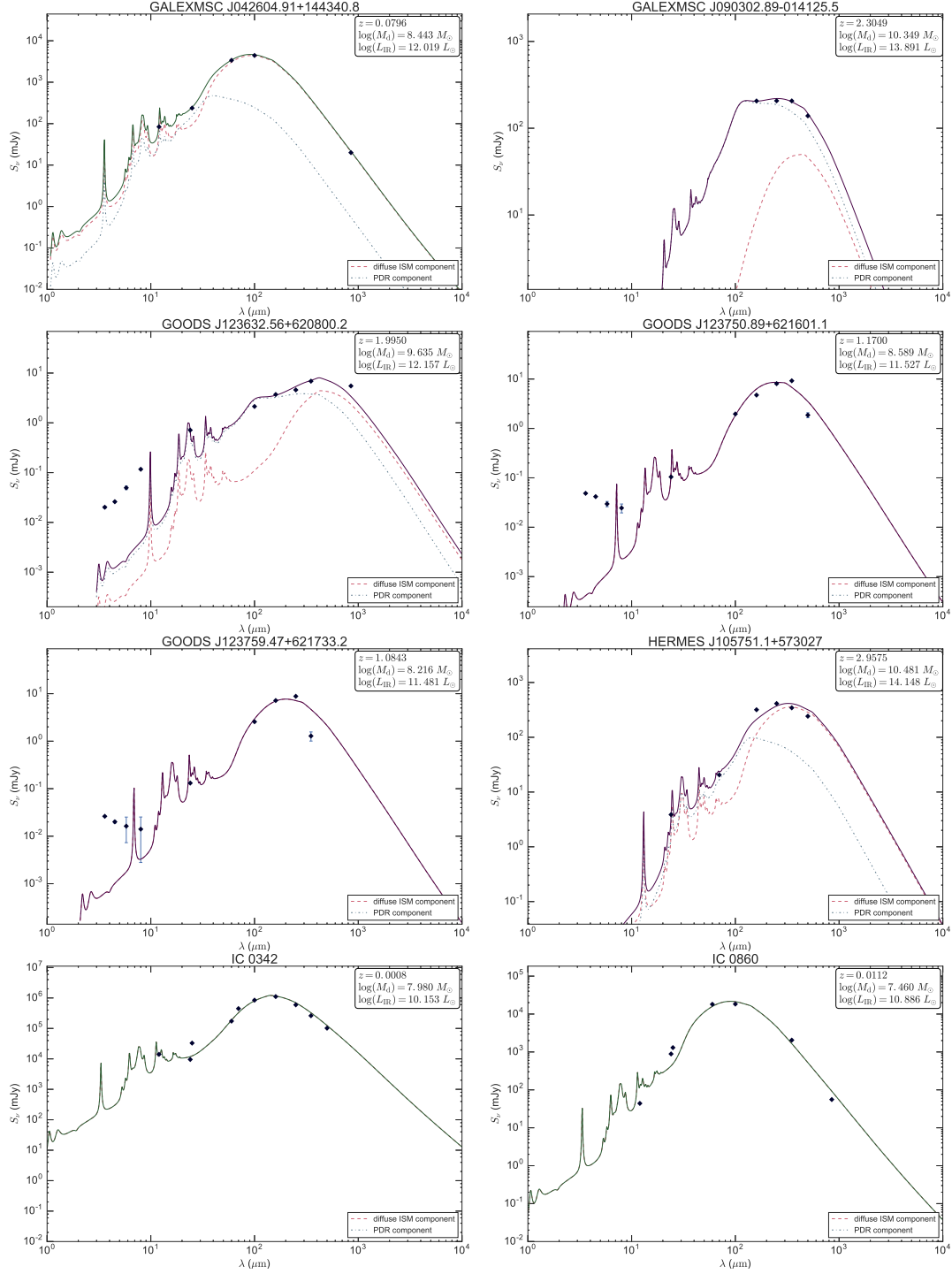


Figure C.4: Spectral energy distributions (SEDs) 4 of 16

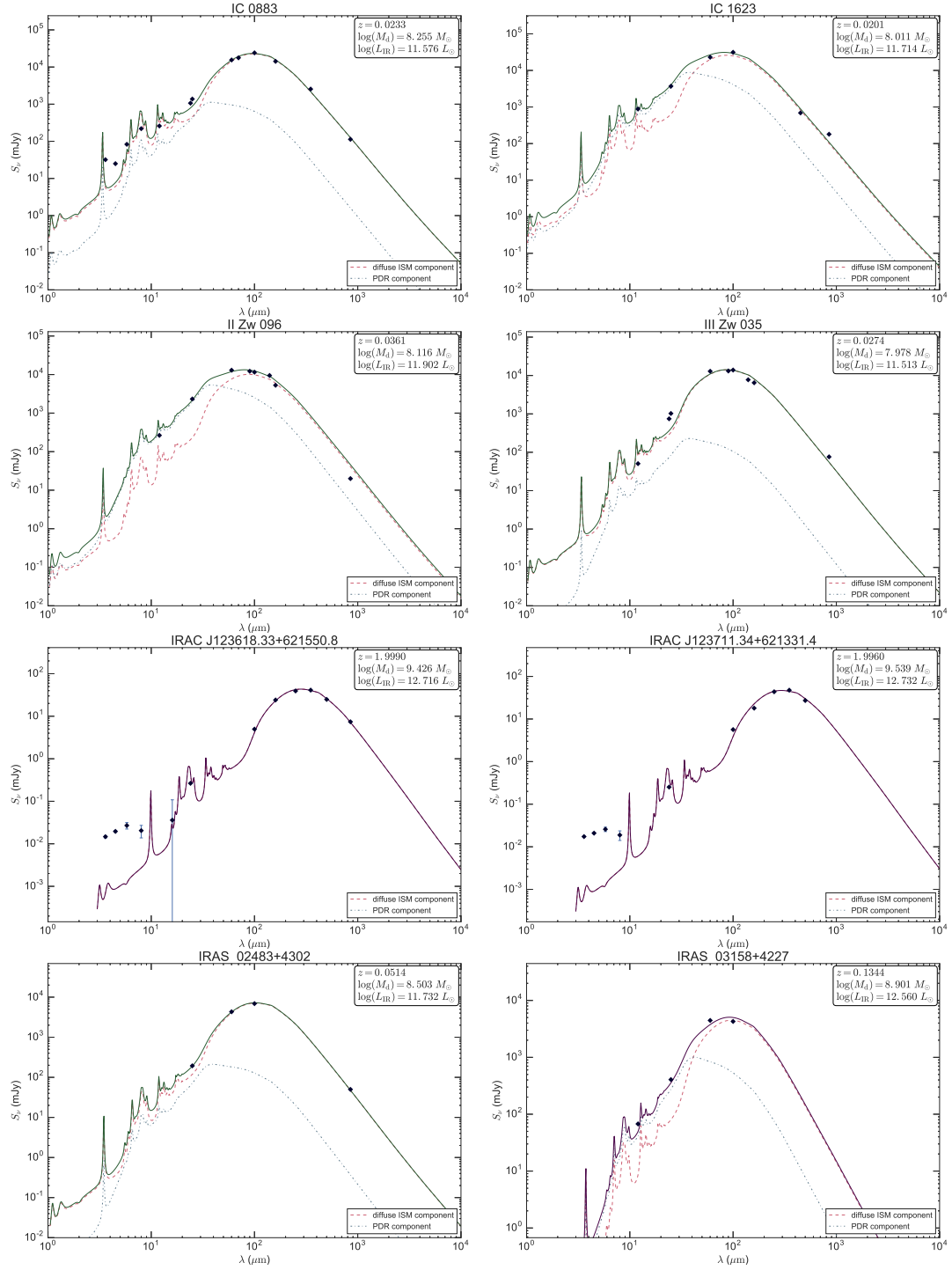


Figure C.5: Spectral energy distributions (SEDs) 5 of 16

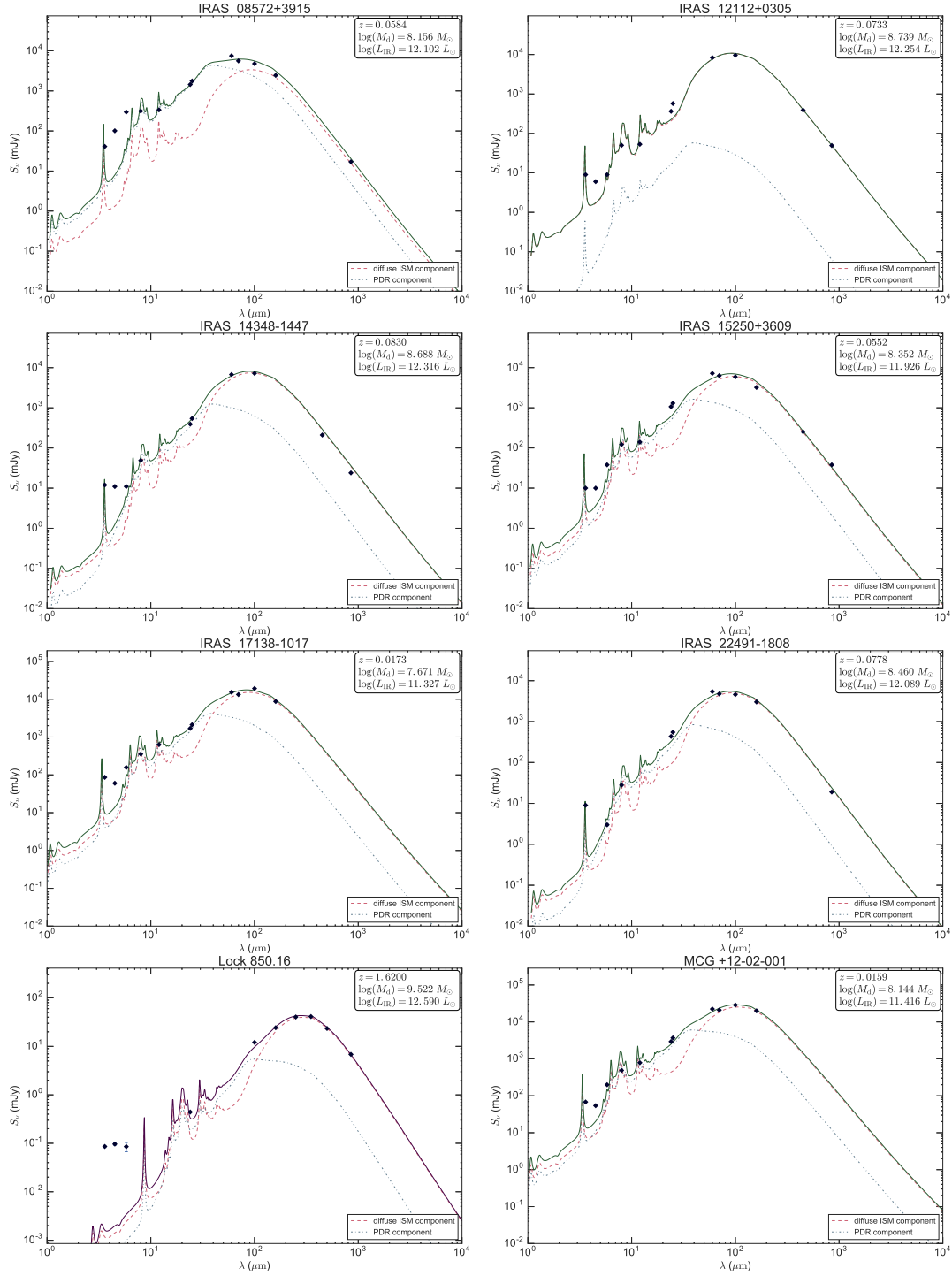


Figure C.6: Spectral energy distributions (SEDs) 6 of 16

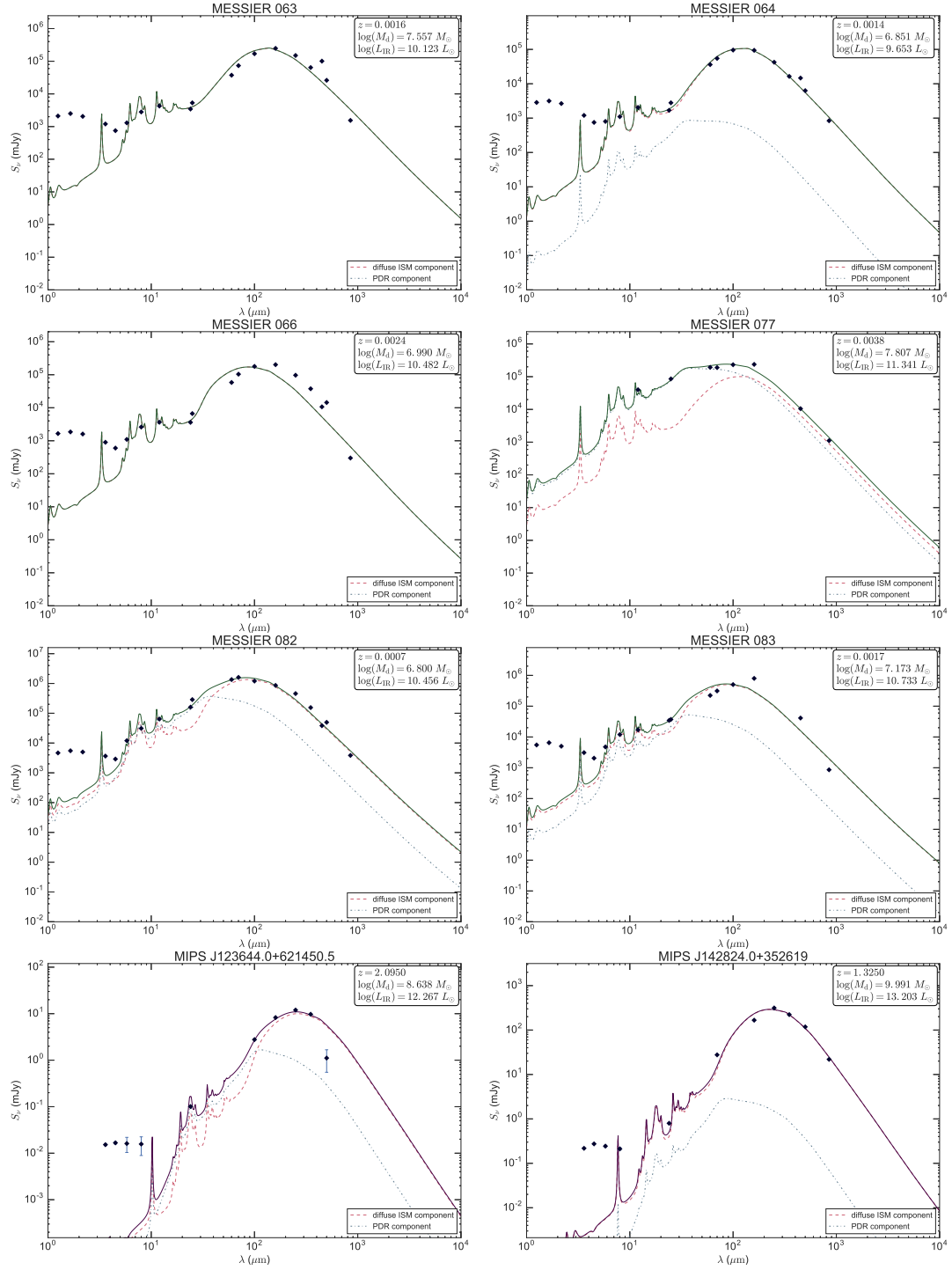


Figure C.7: Spectral energy distributions (SEDs) 7 of 16

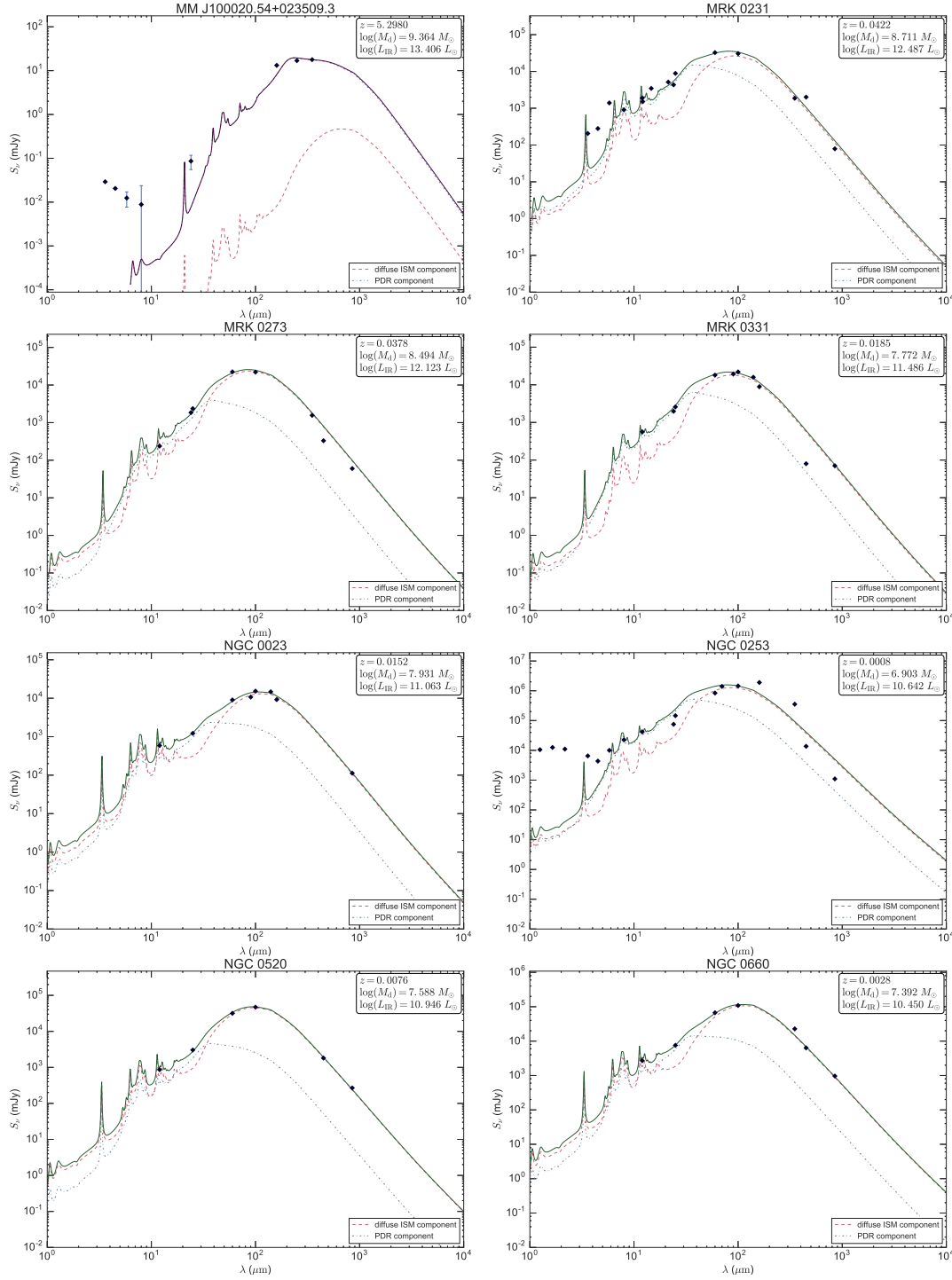


Figure C.8: Spectral energy distributions (SEDs) 8 of 16

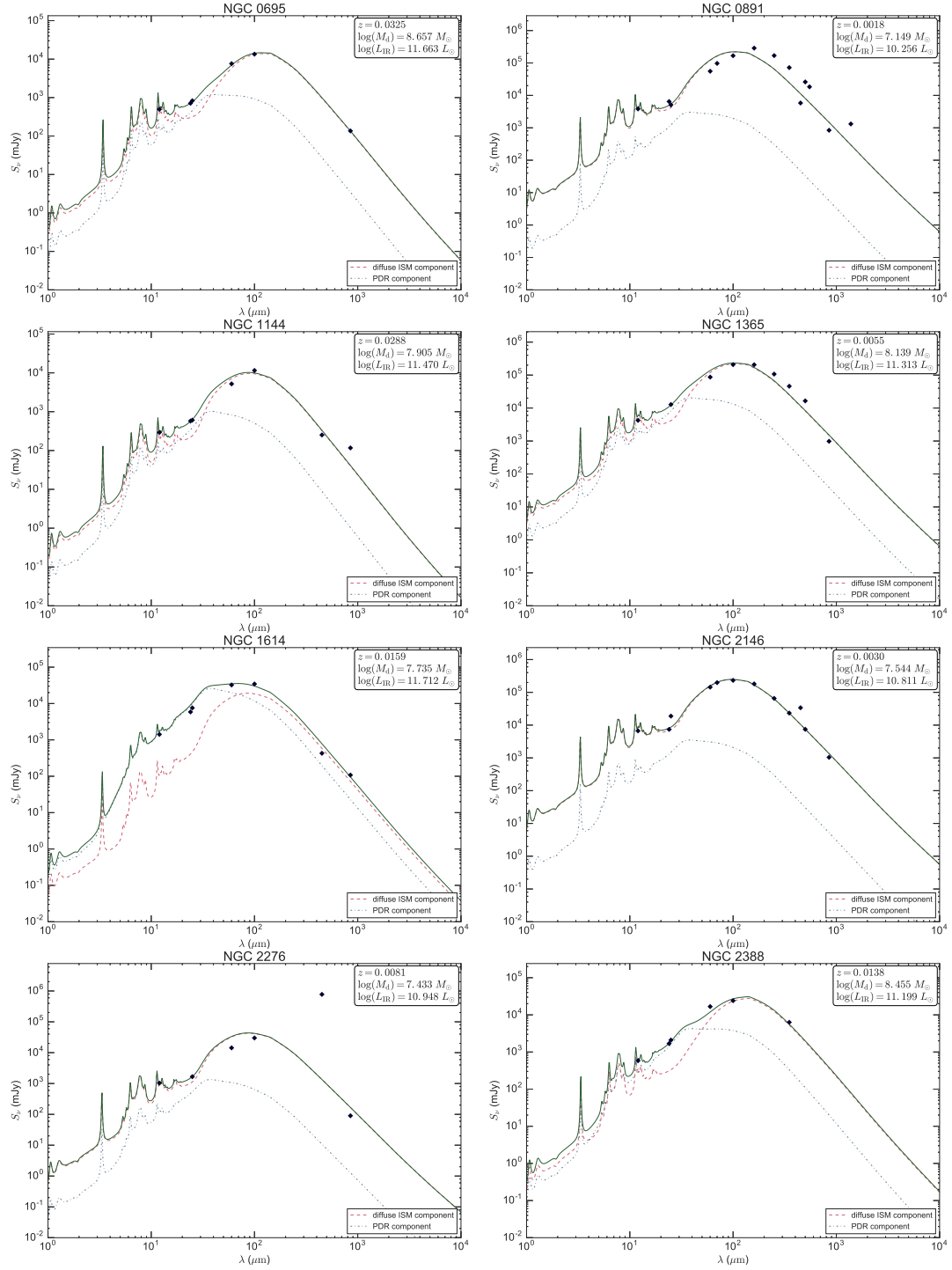


Figure C.9: Spectral energy distributions (SEDs) 9 of 16

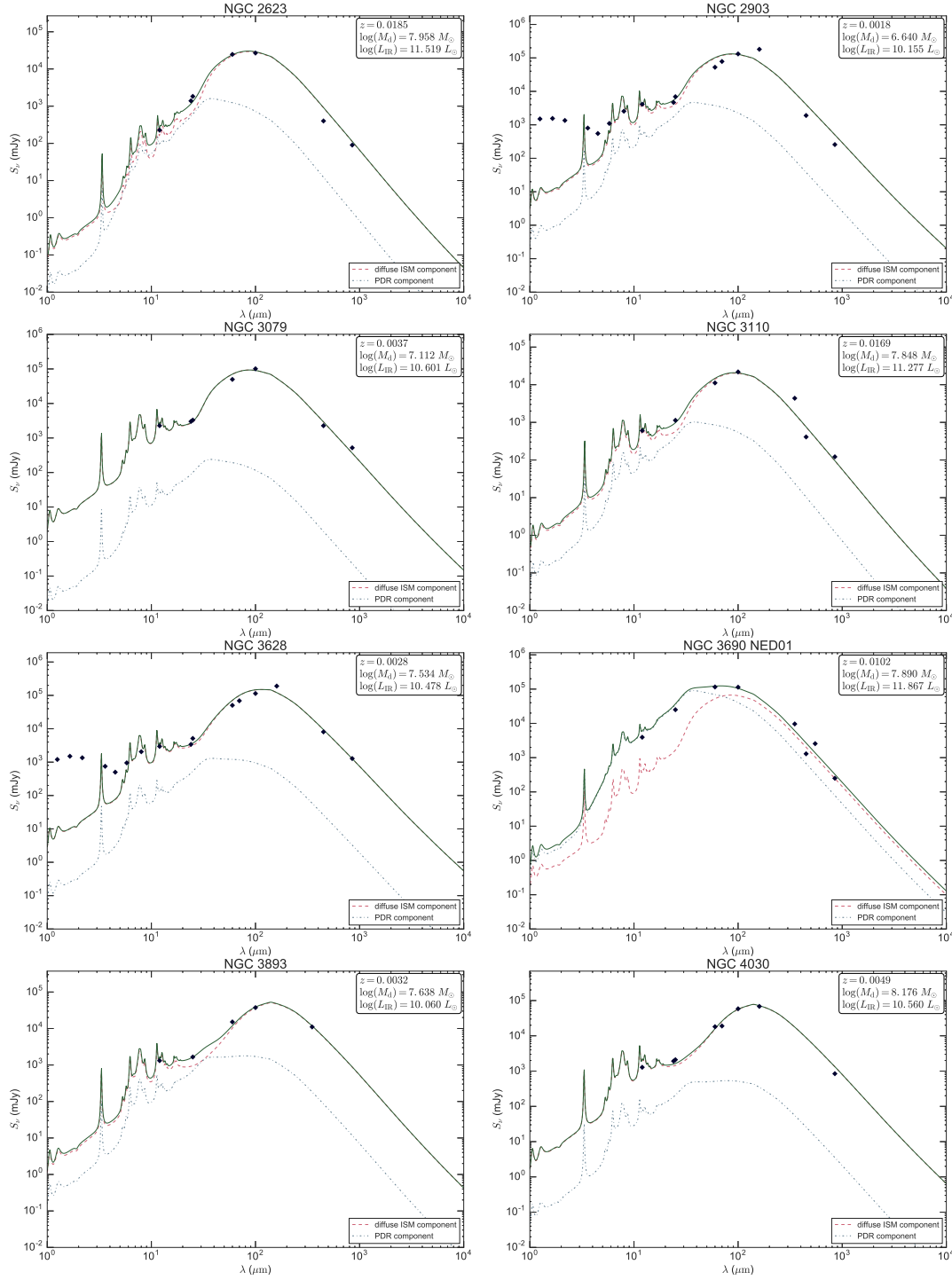


Figure C.10: Spectral energy distributions (SEDs) 10 of 16

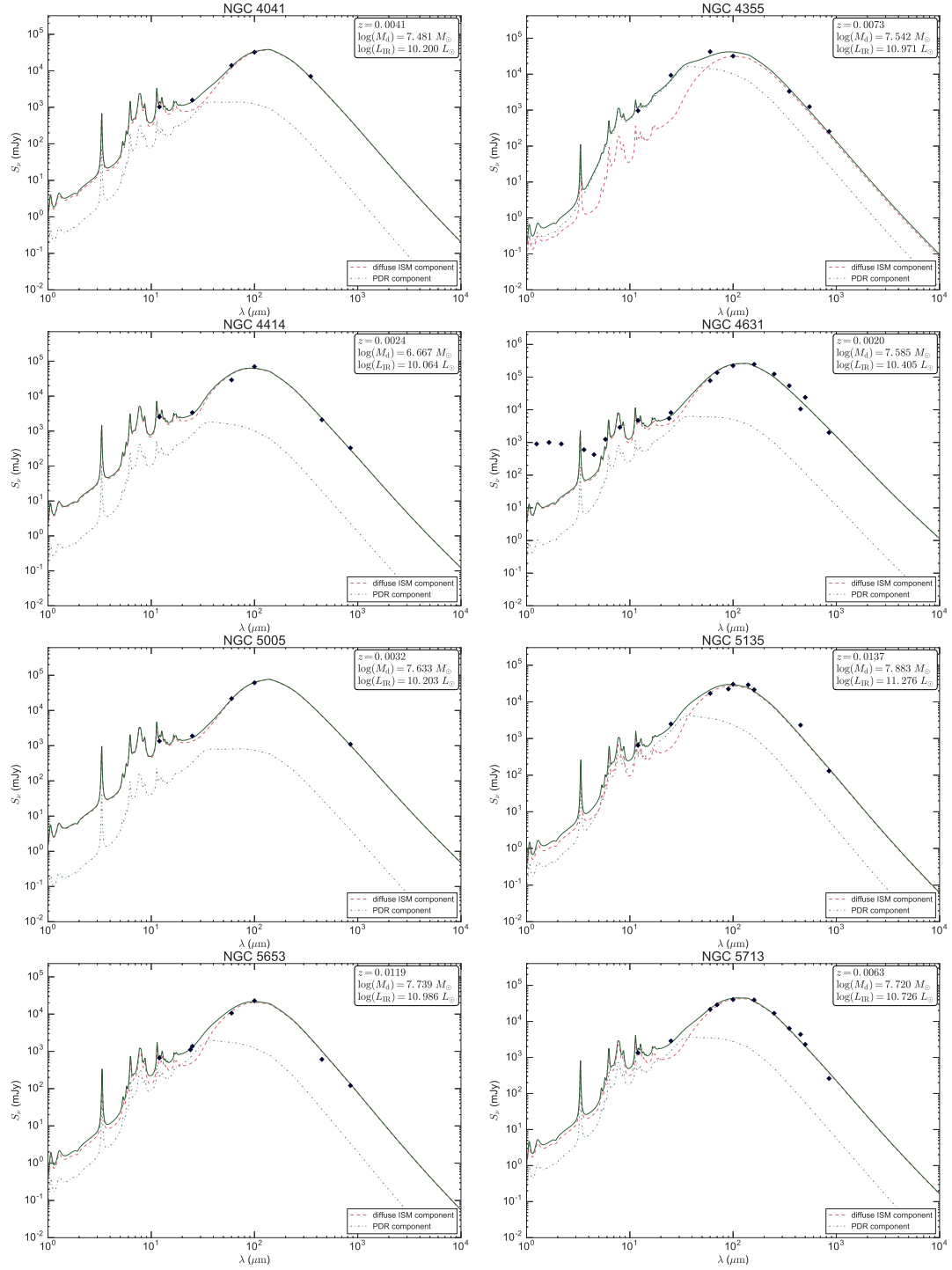


Figure C.11: Spectral energy distributions (SEDs) 11 of 16

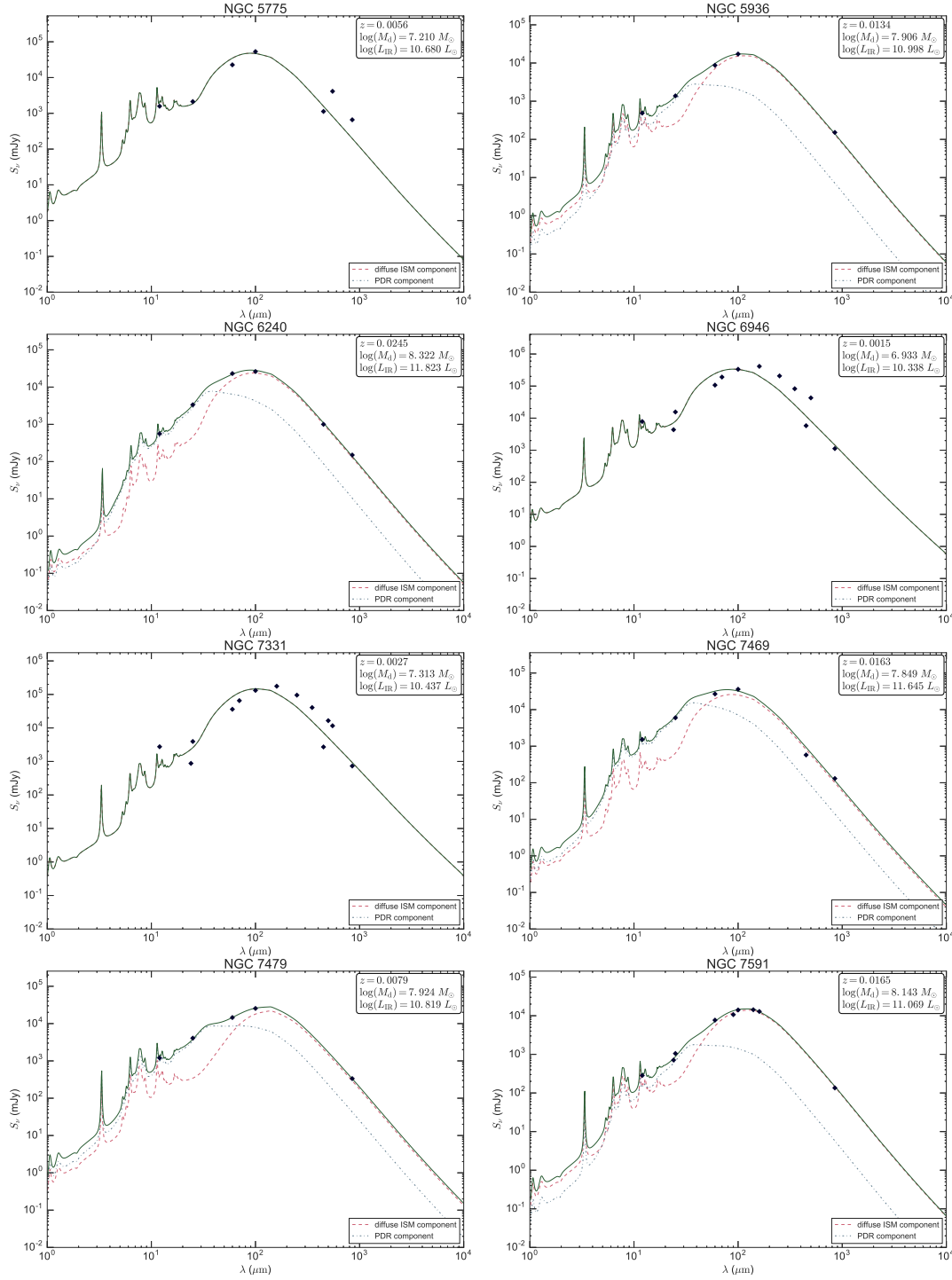


Figure C.12: Spectral energy distributions (SEDs) 12 of 16

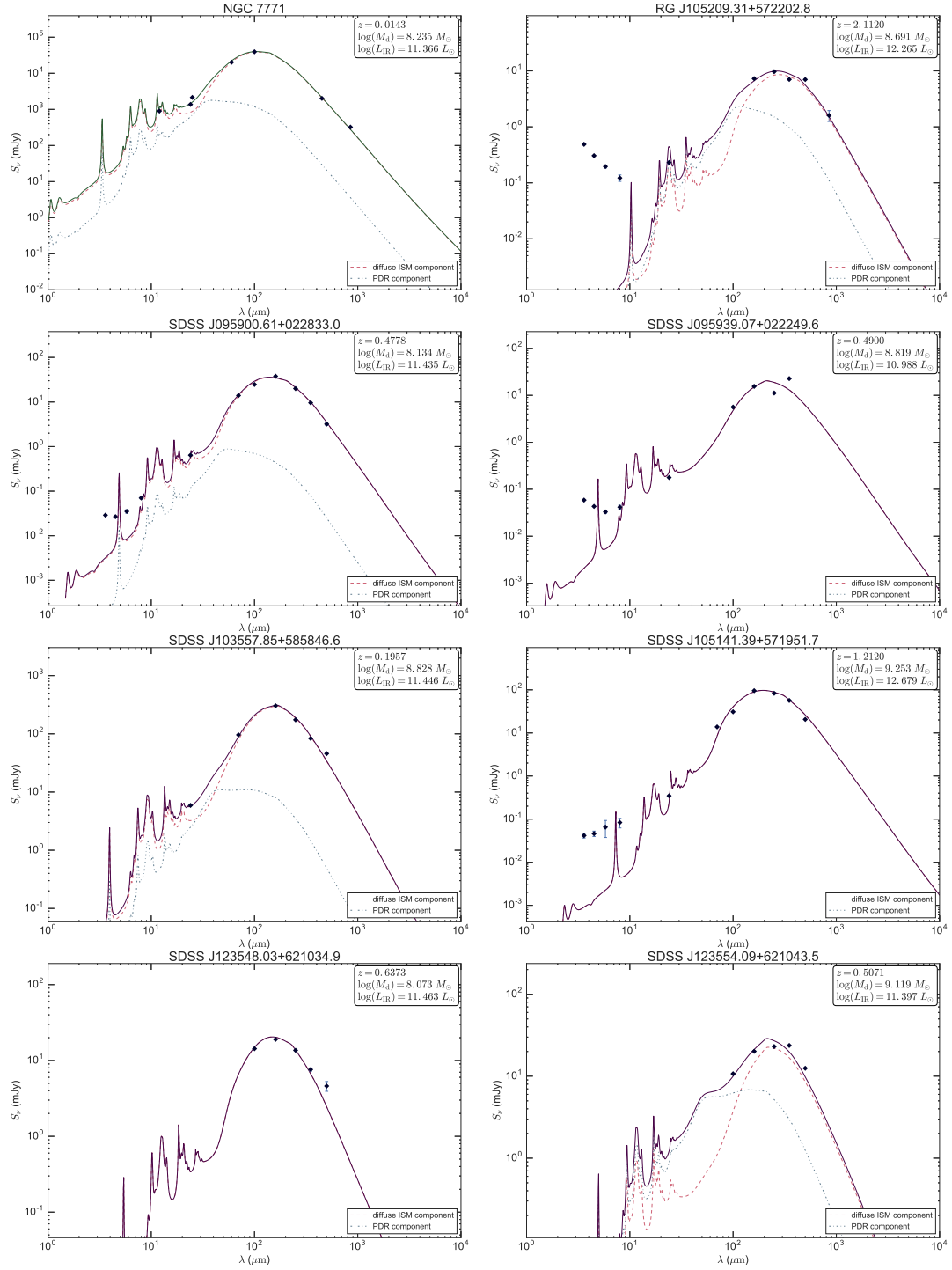


Figure C.13: Spectral energy distributions (SEDs) 13 of 16

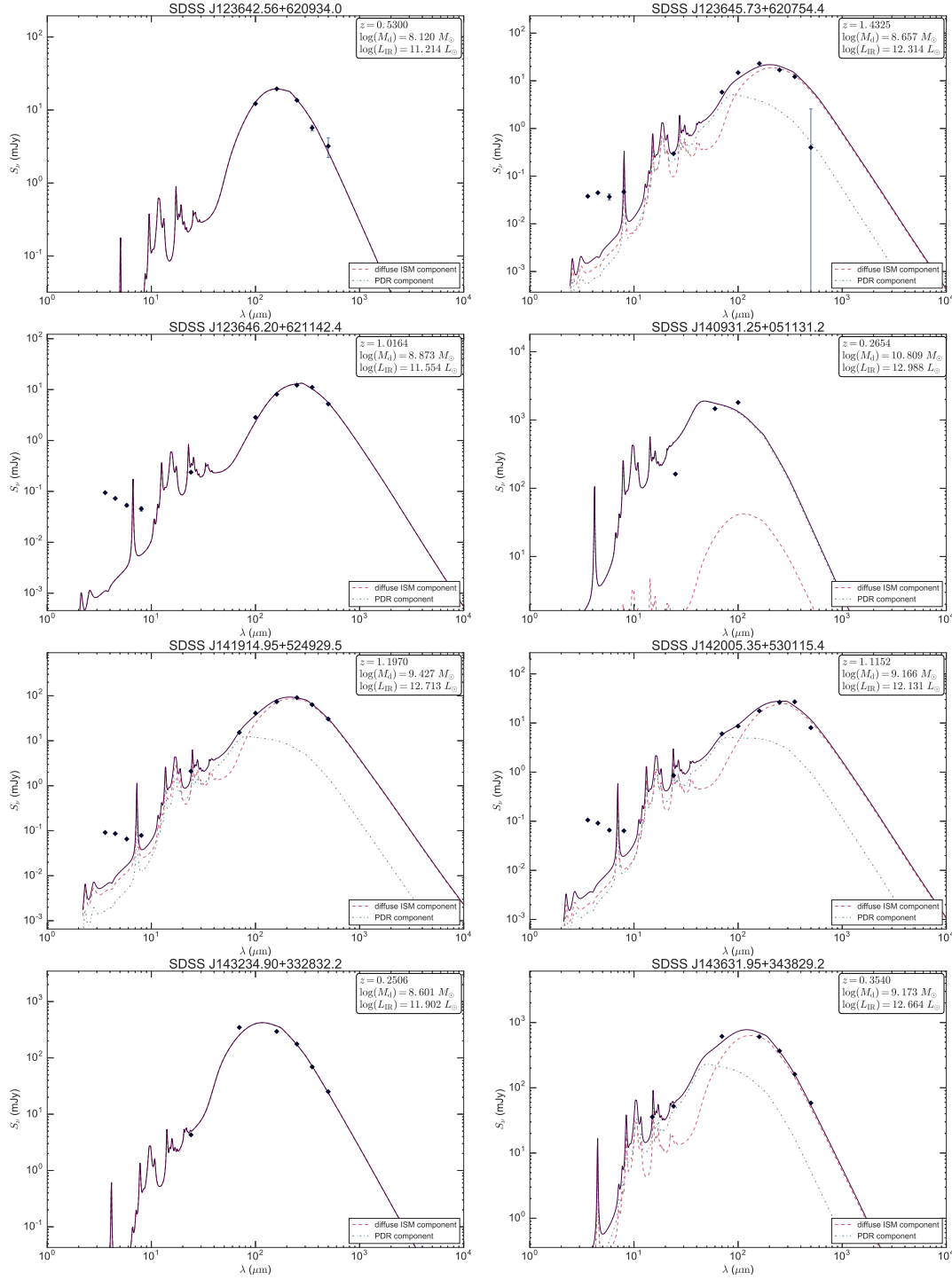


Figure C.14: Spectral energy distributions (SEDs) 14 of 16

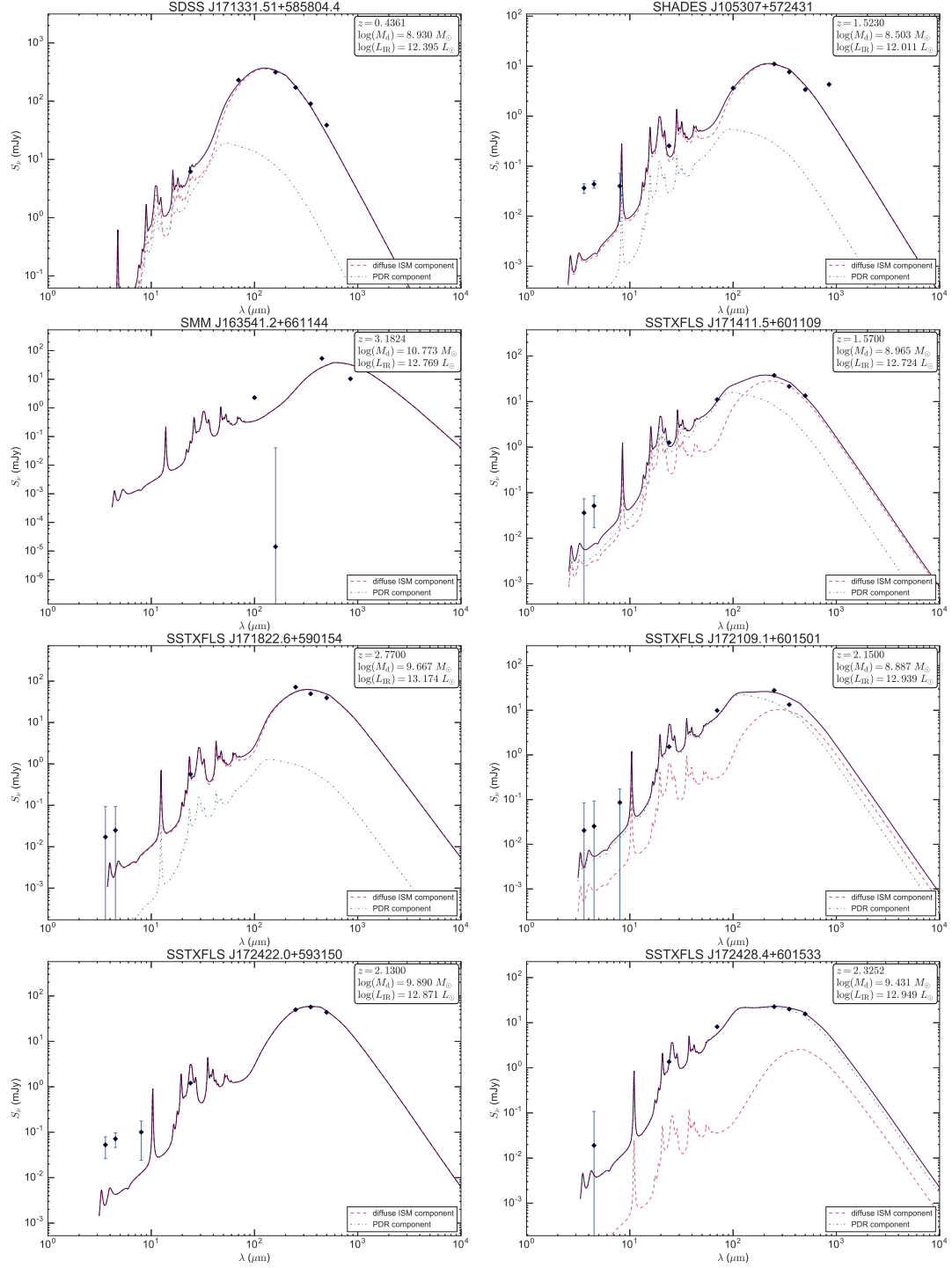


Figure C.15: Spectral energy distributions (SEDs) 15 of 16

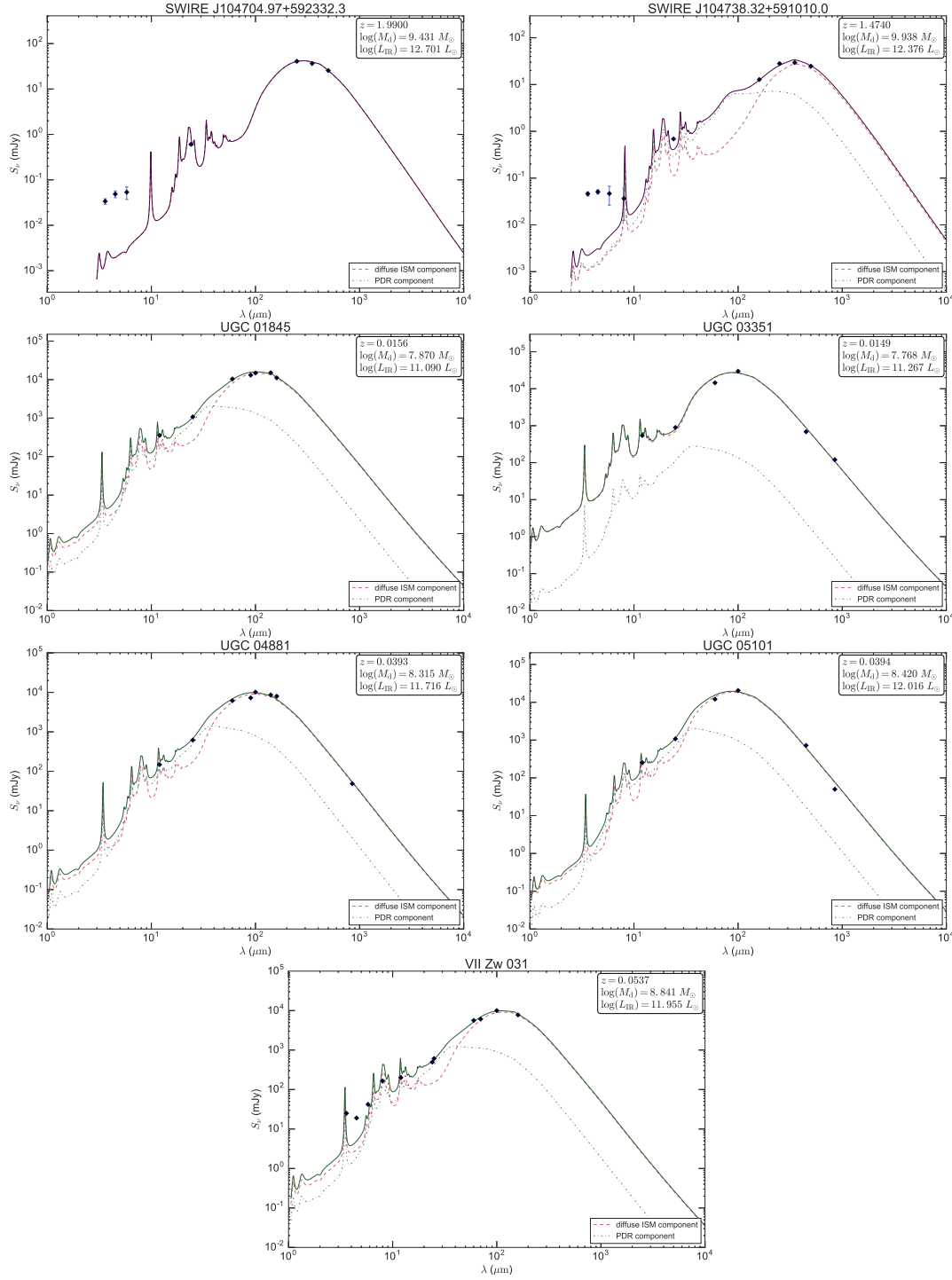


Figure C.16: Spectral energy distributions (SEDs) 16 of 16